Doctorate Dissertation (Censored)

博士論文（要約）

Observational study on spatiotemporal characteristics of hydrometeors and aerosols using multi-platform satellite measurements

（複数の衛星観測を用いた雲・降水粒子とエアロゾルの時空間特性に関する観測的研究）

Maki Kikuchi

菊池　麻紀

Abstract

The atmospheric particles, such as cloud, precipitation and aerosol, have fundamental influences on the formation and change of the Earth's climate system. Such climatic effects of the atmospheric particles are largely determined by their phase and shape, along with the interactions among the particles. However, physical properties of these particles and their roles in climate are not yet fully understood on a global scale, making it uncertain to predict the climate change. This calls a need for the satellite observation, which is the only effective means to measure the microphysical properties, such as particle phase and shape, and their spatiotemporal variabilities on a global scale.

During the last decades, significant progresses have been made in satellite remote sensing of cloud and aerosol microphysics, particularly given the vertical measurement capability by the active sensors and high-frequency measurements by the so-called next generation geostationary satellites. These technical advancements added new vertical and temporal dimensions to the atmospheric observation, taking one step further toward the ultimate goal of satellite observing system to monitor four-dimensional variability of the atmospheric particulate environment over the globe. These new capabilities of satellite observations motivate this dissertation study that exploits the vertical and temporal measurement information to develop more complete and comprehensive algorithms for retrieving cloud, precipitation and aerosol microphysical properties with those different particles appropriately distinguished. Specifically, this study aims at observational analysis of how the microphysical properties of cloud, precipitation and aerosol vary in various spatiotemporal scales, and development of algorithms for discriminating different particles based on the observational findings. This dissertation study is comprised of three major parts: (a) analysis to reveal the vertical characteristics of cloud phase and ice crystal shape on a global scale using a satellite-borne lidar (Chapter 3); (b) development of algorithm that discriminates cloud/precipitation phase and cloud particle shape (hereafter referred to as the cloud or hydrometeor particle type) by combining radar measurement information with the lidar-based classification method (Chapter 4); and (c) development of algorithm that discriminates clouds from aerosols based on significant differences in their spatiotemporal variabilities by employing the high-frequency measurement capability offered by the next generation geostationary satellite (Chapter 5).

In Chapter 3, global and seasonal characteristics of cloud particle type were investigated using depolarization and backscattering measurements from satellite observations of Cloud-Aerosol Lidar and Infrared Pathfinder Satellite Observations (CALIPSO). This study revised the cloud particle type classification algorithm developed by a previous study to assign appropriate ice particle type to the unknown type and to extend the analysis period from three months to one entire year to investigate the

seasonal characteristics of the particle types. In contrast to the most widely used CALIPSO cloud phase product by National Aeronautics and Space Administration (NASA), the cloud particle type classification in this study has an advantage of fully resolving vertical inner structure of clouds and thus representing more detailed cloud structures as it avoids applying the horizontal averaging scheme. The statistical analysis based on the algorithm was performed to reveal how the cloud phase/type characteristics tend to vary with environmental conditions such as temperature and humidity on a global scale. In particular, the strong temperature dependence of ice plates concentrating at temperature range of -15 °C identified in the previous study was found to be the ubiquitous nature of ice plates climatology.

In Chapter 4, the lidar-based classification was then combined with radar observations by CloudSat satellite to explore how the cloud particle types vary globally depending on both temperature and particle size. Given the large sensitivity of radar reflectivity, an observable by CloudSat, to cloud particle size, the consistent characteristic of temperature – particle size dependency identified in the classical laboratory experiments were revealed for the first time on the global scale. The relationship thus found was then utilized to develop CloudSat – CALIPSO synergy hydrometeor particle type classification. Here, the complementary nature of CloudSat and CALIPSO sensitivity was employed to derive vertical particle type structures of hydrometeors for a wide range of cloud systems from thin cirrus to deep convective cloud and light precipitation. The uniqueness of the present analysis is in its effective use of the more realistic multivariable dependence of radar reflectivity and temperature, instead of assuming solid thresholds of reflectivity and temperature in assigning the particle types as done in previous studies. As a result, the algorithm provides a comprehensive breakdown of the total hydrometeor occurrence, often derived in previous studies, into relative contributions from different particle types, offering microphysics-based insight into the general idea of cloud occurrence.

In Chapter 5, an algorithm to discriminate aerosols from clouds was developed by utilizing 10-minute frequency measurement of the Japanese next generation geostationary satellite, Himawari-8. Based on the fact that aerosols and clouds have significantly different characteristics of spatiotemporal variability, the algorithm exploits the high-frequency measurement capability of Himawari-8 to discriminate the two particles, thereby addressing a long-standing issue of cloud contamination in aerosol remote sensing with traditional passive sensors. The results were validated against the ground-based observations to demonstrate improved retrievals of aerosols in the form of the statistics such as the root mean square error, correlation and bias. The methodology developed is regarded as a scheme to discriminate different atmospheric particles by using their differences in the spatiotemporal characteristics.

In summary, the state-of-the-art satellite observations offering vertical and temporal dimensions to the atmospheric measurement were exploited in this thesis study to analyze microphysical characteristics (particle types and phases) and spatiotemporal characteristics of the atmospheric particles. The findings obtained from the analysis were then employed to develop new algorithms for discriminating different particle types. Future studies include more intensive validations of the algorithms using aircraft in-situ measurements, ground-based networks and other satellite measurements. The hydrometeor particle type algorithm developed are applicable to future satellite missions, such as Earth, Clouds and Aerosols Radiation Explorer, to construct three-dimensional global long-term dataset of hydrometeor particle types. The aerosol – cloud discrimination scheme will also be applied to other existing and upcoming series of the next generation geostationary satellites (such as the Geostationary Operational Environmental Satellite-R Series and Meteosat Third Generation) to extend the observational analysis from Asia-Oceania to the whole globe. The observation-based knowledge obtained from this study also has an implication for evaluation and improvement in representations of atmospheric particles in numerical climate models for mitigating uncertainties of climate projection relevant to atmospheric particles. The synergistic analysis of the vertical and temporal dimensions explored in this study will further advance our understanding of fundamental processes governing microphysical structures of the atmospheric particles that vary in various temporal and spatial scales.

Acknowledgement

First and foremost, I would like to express my deep gratitude to Prof. Kentaroh Suzuki of Atmosphere and Ocean Research Institute, the University of Tokyo, for all the discussions and insightful advice and inspirations to my research. I have learnt extensively from him, including how to raise new questions, interpret analyzed results and find new perspectives from them. Since I first met him at the CloudSat-CALIPSO meeting in 2014, he has taught me the excitement to study and explore science.

I am grateful to Prof. Hajime Okamoto, Research Institute for Applied Mechanics, Kyushu University, for his educational instructions and suggestions during my research career, which started when I knocked his laboratory office in the second grade at the Tohoku University.

I would like to offer my gratitude to Prof. Yukari Takayabu of Atmosphere and Ocean Research Institute, the University of Tokyo, for her profound and detailed suggestions to my thesis work. I also would like to appreciate Prof. Makoto Koike of Department of Earth and Planetary Science, and Prof. Masaki Satoh and Prof. Akira Oka of Atmosphere and Ocean Research Institute, the University of Tokyo. It has been a great honor for me to make the presentations in front of the thesis committee and to have their invaluable comments to my thesis study.

I greatly appreciate my wonderful colleagues at the Earth Observation Research Center of Japan Aerospace Exploration Agency. My special appreciation goes to Dr. Riko Oki, Dr. Takuji Kubota, Dr. Mayumi Yoshida, Dr. Yuichiro Hagihara, Dr. Tomoko Tashima, Ms. Yuki Kaneko, Ms. Moeka Yamaji, Mr. Kosuke Yamamoto, Dr. Risa Miyazaki and Ms. Misako Kachi for their patience and providing me a comfortable and warming environment to carry out my research. I wish to extend my thanks to Dr. Hiroshi Murakami, Dr. Takashi Nagao and Prof. Teruyuki Nakajima for their continuous guidance and precise advice to my research.

I also would like to appreciate all my co-authors of the papers included in this thesis: Dr. Kaori Sato of Research Institute for Applied Mechanics, Kyushu University, Dr. Gregory Cesana of Department of Applied Physics and Mathematics, Columbia University, Dr. Akiko Higurashi of Center for Environmental Measurement and Analysis, National Institute for Environmental Studies, Prof. Nobuhiro Takahashi of Institute for Space-Earth Environmental Research, Nagoya University, and Prof. Tadahiro Hayasaka of Center for Atmospheric and Oceanic Studies, Tohoku University. They have offered guidance, feedback and advice to my research. It has always been my great pleasure to collaborate and work with them.

I wish to express my gratitude to Dr. Makiko Hashimoto of GOSAT-2 Project Team, Japan Aerospace Exploration Agency, Dr. Daisuke Goto of Center for Regional Environmental Research, National Institute for Environmental Studies, Ms. Haruka Hotta, Dr. Sam Sherriff-Tadano, Dr. Kaya Kanemaru, Dr. Akira Yamauchi, Dr. Takuro Michibata and the members of Atmosphere and Ocean Research Institute, the University of Tokyo, for their technical support, valuable advice and extensive discussions around this thesis work.

Special thanks are to all individuals and organizations that provided me the data used in this work. The CloudSat and the CloudSat-collocated TRMM and ECMWF data are downloaded from the CloudSat Data Processing Center (http://www.cloudsat.cira.colostate.edu) and CALIOP data are downloaded from the Atmospheric Science Data Center (https://eosweb.larc.nasa.gov). The aircraft observation data was provided by Dr. Olivier Jourdan and Dr. Guillaume Mioche. The AERONET data was obtained via NASA AERONET website (https://aeronet.gsfc.nasa.gov).

The last, but not the least, my warmest thanks goes to my family. My husband Yosuke has been supportive and encouraged me all the time in carrying out my research and work. My father Mitsuo and mother Mika have always been my role model in my life. I thank my sister Miki and my brother Seiya for their warm smiles and entertainments in our family. I owe my loving appreciation to my granny throughout my life. I am proud of being their family.

September, 2018

Contents

Chapter 1 General Introduction

1.1 Background

The particles in the Earth's atmosphere are principally composed of three elements—cloud, precipitation and aerosols. They are the key determinants of the radiation budget and water cycle in the Earth, thereby giving significant influence to the climate system. Cloud and aerosol affect the Earth's radiation field by scattering and absorbing solar radiation and re-emitting their thermal radiation. Another source of energy supply to the atmosphere is the release of latent heat through thermodynamic phase change between liquid droplets and ice crystals. This latent heat release acts to invigorate cloud convection system, thereby changing lifetime of cloud and further influencing the radiation field. Life of a cloud is initiated by condensation of water vapour on to aerosol nuclei, grow through collision and collection processes, and finally dissipated by evaporation or precipitation. The aerosol influence on microphysical properties of warm clouds are well known as the "Twomey Effect", which refers to the increase of aerosol (or cloud condensation nuclei; CCN) enhancing number of cloud droplets and reducing cloud particle size if cloud water content is conserved, leading the cloud to become optically thicker and increase solar reflection back to space [Twomey, 1974]. Consequently, smaller water droplets extend lifetime of its cloud, suppress precipitation and keep its water content [Albrecht, 1989]. However, smaller water droplets also induce an opposite effect by increased dry air entrainment, causing evaporation to lose its moisture [Ackerman et al., 2004]. In the case of ice nuclei (IN) injecting into a mixed phase cloud, water droplets start to glaciate though contact or immersion/condensation freezing, leading clouds to break up and increase amount of solar radiation reaching the surface [Christensen et al., 2014]. Here, the freezing processes are also accelerated by the so-called Wegener-Bergeron-Findeisen process [Bergeron, 1935; Findeisen, 1938], where ice formation is enhanced at the expense of surrounding supercooled water due to the lower saturation vapour pressure of ice compared to liquid. In addition, larger ice particles grow more rapidly through collection of surrounding particles. These mechanisms induce clouds to precipitate efficiently and shorten its lifetime [Christensen et al., 2014; Storelvmo et al., 2015]. The above physical processes play a key role particularly in cloud phase response to a warmed atmosphere, where the altitude of the freezing temperature generally rises, partly converting ice clouds to water, leading to cool the Earth's surface. This "cloud-phase negative feedback" is known to be a possible major factor for compensating temperature rise by CO_2 warming.

A work by McCoy et al. [2015] evaluated 19 Coupled Model Intercomparison Project Phase 5 (CFMIP5) climate models, focusing particularly on the thermodynamic phase representation within the models. In general, climate models determine cloud phase diagnostically (as a function of temperature), prognostically

(employing more complex microphysical processes) or the combination of the two [Cesana et al., 2015]. McCoy et al. [2015] evaluated the cloud phase representation in the models by investigating the partitioning of cloud water and ice as a function of temperature and showed that the freezing temperature (at which liquid and ice particles are equally mixed) varied as much as 40 K among the models, generally underestimating liquid water and producing ice instead, causing clouds to become optically thinner and increase solar radiation penetration. They discussed that this is partly subjected to the long-standing large warm bias of the surface shortwave radiance over the Southern Ocean found in climate models [Kay et al. 2016a]. Another study by Tan et al. [2016] showed constraining cloud phase partitioning observationally to the Community Atmosphere Model (CAM) climate model would increase liquid and decreased ice, in a sense to tune the underestimation found in McCoy et al. [2015], leading to depress glaciation process in a warmed climate (as the cloud is already in liquid phase). This resulted to weaken the negative cloud-phase feedback and, consequently, increase the climate sensitivity by up to 1.3K.

Although Tan et al. [2016] clearly demonstrated the sensitiveness of cloud phase to climate and identified that the freezing temperature assumption significantly affects the strength of the negative cloud phase feedback, the climate sensitivity response to cloud phase is yet to be investigated and evaluated with various climate models based on cloud phase observations in detail, given the variability in cloud phase representation shown by McCoy et al. [2015]. From the discussion above, cloud phase exerts different responses to aerosol perturbation in changing microphysical and radiation properties of clouds, along with associated precipitation processes, influencing the radiation balance and precipitation formation in the Earth. Hence this calls for the need to the satellite observations, which are considered to be the only effective way to acquire the microphysical properties (such as particle phase and shape) and the spatiotemporal variabilities of atmospheric particulates on a global scale.

1.2 Observations from Space

1.2.1 Conventional Passive Satellite Instruments

To better constrain cloud, precipitation and aerosol microphysical properties and processes in numerical models, their detailed observations over the globe are required. Passive remote sensing was the basis of the atmospheric observation over time. Cloud phase was traditionally detected by measuring visible and near-infrared radiances or brightness temperature differences of two infrared bands [Baum et al., 2000; Platnick et al., 2003] or by using the polarization sensitivity difference between liquid and ice particles [Goloub et al., 2000; Riedi et al., 2010]. The polarization information has also been employed to characterize shapes of ice crystals [Chepfer et al. 2001; Sun et al. 2006]. Precipitation observation also started by passive microwave radiometers. For example, precipitation rate estimation method was developed by Liu and Curry

[1992] and Liu and Curry [1996] from the Advanced Microwave Scanning Radiometer for the Earth Observation Satellite (AMSR-E) and Kummerow et al. [1996] and Kummerow et al. [2001] from Microwave Imager (TMI) onboard the Tropical Rainfall Measuring Mission (TRMM). Aerosols properties by passive imagers were primarily retrieved over ocean by Kaufman et al. [1997], Tanre et al. [1997] and Levy et al. [2003] using the MODerate Resolution Imaging Spectroradiometer (MODIS). Hsu et al. [2004, 2006] developed an algorithm that enable the aerosol retrieval over land using blue wavelength measurements. Gordon and Wang [1994] and Higurashi and Nakajima [2002] developed the retrieval schemes for the Sea-viewing Wide Field-of-view Sensor (SeaWiFS). Dubovik et al. [2011] showed a new algorithm using statistical optimization in inversion and Fukuda et al. [2013] used the Cloud and Aerosol Imager (CAI) onboard the Greenhouse gases Observing SATellite (GOSAT) to retrieve aerosol optical thickness over land.

The passive remote sensing from space was a significant advancement at the time and offered detailed measurements of atmospheric and surface states over the globe. Their observation projected profound implications in the complexity of the Earth's system with interactions and feedbacks between various components within and among atmosphere, land and ocean. This emerged the necessity to improve our understanding in the *processes* that governs the interactions and feedbacks, rather than just monitoring the atmosphere and surface states as a *result* of those processes. Since hydrological cycle is a dynamic system accompanying phenomena in both vertical and temporal dimensions, limiting to the conventional horizontal distribution observations of atmospheric particles is insufficient to fully understand their processes. In recent decades, two types of satellites have been developed that offer a vertical dimension and a temporal dimension to the atmospheric observation. One is the polar-orbiting satellites with active instruments, providing the vertical dimension, and the other is the so-called next-generation geostationary satellites with passive instruments, providing the temporal dimension to the conventional horizontal observations.

1.2.2 Active Satellite Instruments

Active remote sensing of cloud started from the launch of the CloudSat and Cloud–Aerosol Lidar and Infrared Pathfinder Satellite Observations (CALIPSO) satellites in April 2006. The precipitation measurement started beforehand by the TRMM in November 1997, followed by its successor, the Global Precipitation Measurement (GPM) Core Observatory, which was launched in February 2014. These measurements offered detailed vertical structure of the global cloud and precipitation. Their new capabilities have been extensively exploited to develop algorithms for retrieving cloud and precipitation microphysical properties. Cloud phase discrimination is one such algorithm for identifying cloud water droplets and ice crystal habits. Hu et al. [2009] developed the first algorithm that discriminates cloud phase and horizontal ice plates from the Cloud-Aerosol LIdar with Orthogonal Polarization (CALIOP) backscatter

and polarization measurements and is provided as the National Aeronautics and Space Administration (NASA) Level 2 Vertical Feature Mask (VFM) product. Their algorithm demonstrated the capability of estimating vertical features of cloud phase from space, although it should be noted that, to date, they generate layer type classification (i.e. one phase per cloud layer). Yoshida et al. [2010] and Cesana and Chepfer [2013] later developed their own algorithms that fully resolved vertical inner structure of clouds to generate the maximum capability of CALIOP measurement.

Although CALIOP has the advantage in detecting thin cirrus, its signal is strongly attenuated against water and thick ice clouds, making it difficult to detect clouds underneath. On the contrary, the Cloud Profiling Radar (CPR) onboard the CloudSat has the advantage of penetrating into thick clouds, although it is not sensitive to optically thin clouds. These two characteristics of the CALIOP and CPR are complementary to each other so that their combined use can be powerful to detect a wide range of clouds from cirrus to precipitation. Cloud phase identification using the CPR and CALIOP has been provided in the NASA official product of 2B-CLDCLASS-LIDAR, although the cloud layer is not vertically resolved [Wang et al., 2013]. In contrast, Ceccaldi et al. [2013] developed a vertically resolved cloud phase algorithm from the synergetic observation of the CPR and CALIOP.

1.2.3 Next Generation Geostationary Satellites

Another type of the new satellite is the next generation geostationary satellites, which load multispectral imagers with high temporal resolution, giving a potential capability of capturing the horizontal movement of cloud and aerosols. The Japanese geostationary satellite, Himawari-8, was launched in October 2014, taking the lead in this series [e.g. Geostationary Operational Environmental Satellite-R (GOES-R) by National Oceanic and Atmospheric Administration (NOAA) and Meteosat Third Generation (MTG) by European Organisation for the Exploitation of Meteorological Satellites (EUMETSAT)]. The technical progress in these satellites from the conventional geostationary satellites can be summarized in the following three points: (1) higher temporal resolution, (2) higher spatial resolution, and (3) increased number of observation wavelengths. The Advanced Himawari Imager (AHI), a payload on the Himawari-8, equips 16 observation bands from visible to infrared wavelength, observing the full disk image over Asia and Oceania every 10 minutes. With regard to the visible wavelength range, for example, the AHI has 0.47, 0.51, and 0.64 μm channels with the spatial resolution of 0.5 km at 0.64 μm channel, in contrast to the previous Himawari-6/7 satellites that had only a 0.64 μm channel with the spatial resolution of 1 km [Bessho et al., 2016].

1.3 Objective

Cloud, precipitation and aerosol behave dynamically in a complex system with interactions and feedbacks among them and between the ambient atmosphere and surface. The 4-dimensional global observation of the atmospheric particles would be an ideal measurement concept that would contribute to untangle the intricate system for deepening our understanding in the physics behind the processes. Towards this goal, this dissertation study exploits the vertical and temporal atmospheric observations offered by the active satellite and next generation geostationary satellites for a more comprehensive understanding of the behaviors of atmospheric particles. Hence the main objective of this study is to reveal spatiotemporal distribution and variability characteristics of cloud, precipitation and aerosol in various temporal and spatial scales — from tens of minutes and a few kilometers to seasonal and global scale. To this end, this study is mainly organized in three sections after the explanations on the analyzed dataset in Chapter 2. The respective objective of the sections are: (a) to reveal global and seasonal characteristics of cloud phase and ice crystal orientation using CALIPSO (Chapter 3), (b) to investigate the dependence of the cloud phase and ice crystal shape on particle size and temperature and to develop an algorithm for discriminating phase and types of hydrometeors by introducing the CloudSat measurement to the CALIPSO classification (Chapter 4), and (c) to develop a scheme to discriminate clouds from aerosol estimation using the difference in spatiotemporal variability characteristics between cloud and aerosol by employing the high-frequency observation of the Himawari-8 (Chapter 5). Finally, the main findings and future perspectives are summarized in Chapter 6.

Chapter 2 Description of Data

This chapter compiles information on the satellite and numerical model data used in the respective chapters of this thesis study.

2.1 CloudSat and CALIPSO

The main data used in Chapters 3 and 4 is the satellite measurements obtained from two satellites, CloudSat and Cloud-Aerosol Lidar and Infrared Pathfinder Satellite Observations (CALIPSO). They fly as a part of the satellite constellation known as “the A-Train” and this formation flight enables synergistic data retrievals with a combined use of their instruments [Stephens et al., 2002]. CloudSat carries a W-band (94 GHz) cloud profiling radar (CPR), which measures backscatter signals from cloud and precipitation. CALIPSO carries 532-nm and 1064-nm dual-length depolarization lidar, the Cloud-Aerosol Lidar with Orthogonal Polarization (CALIOP), and measures backscatter signals from clouds and aerosols. In this study, I used radar reflectivity data from the CPR Level 2B GEOPROF product (Release 04), with vertical and horizontal resolutions of 240 m and 1.1 km, respectively [Mace, 2007; Marchand et al., 2008]. The minimum detectability of the CPR radar reflectivity factor is approximately -28 dbZe [Miller and Stephens, 2001; Stephens et al., 2008]. For CALIOP, it has a capability to not only observe backscattering from particles, but also to receive the depolarization information using an onboard polarization beam splitter to separate parallel and perpendicular components of the 532 nm wavelength. 532 nm total and perpendicular attenuated backscatter data was used from CALIPSO Level 1B products (version 3). Below an altitude of 8.2 km, the resolution is 30 m × 333 m vertically and horizontally, respectively; above 8.2 km, the respective resolution is 60 m × 1000 m [Vaughan et al., 2005]. Minimum detectable backscatter coefficients for the respective altitude range are shown in Table 2.1. CALIOP has a sufficient sensitivity to detect clouds with optical thicknesses as low as 0.01 [McGill et al., 2007], but cannot penetrate optically thick clouds.

Table 2.1 Minimum detectable backscatter coefficient of CALIOP for both day and night (modified from Vaughan et al. [2005]). The maximum altitude used in this study was 20 km, so only altitudes below this are shown.

Altitude Range [km]	Horizontal Resolution [m]	Vertical Resolution [m]	$\beta_{\min}$ [km/sr] (Day)	$\beta_{\min}$ [km/sr] (Night)
0.0 ~ 8.2	333	30	1.91×10^{-5}	1.67×10^{-5}
8.2 ~ 20.0	1000	60	5.54×10^{-6}	4.57×10^{-6}

2.2 MODIS and ECMWF

For the comparison of the retrievals with a different satellite measurement, the observation data of MODerate resolution Imaging Spectroradiometer (MODIS) was used. MODIS is a passive imager loaded on Aqua satellite, also flying over the A-Train. MODIS cloud phase estimation in MAC06S0 product was employed in this study, which is a subset of Aqua/MODIS L2 product (MYD06_L2) along the CloudSat footprint. The original cloud phase classification by MODIS combine two methods: one using the brightness temperature difference between the two thermal infrared bands and the other using the ratio for the near infrared and visible bands [King et al., 2004]. The detailed information on MODIS-AUX is given in the CloudSat Project document [2008].

The ambient field data from the numerical model of European Centre for Medium Range Weather Forecast was employed in the algorithm development of satellite retrievals and in the comparisons of the retrievals with environmental conditions. The atmospheric temperature, pressure and specific humidity profiles were used in the CloudSat auxiliary product (ECMWF-AUX) provided by the CloudSat project, which is ECMWF ambient data interpolated to each CloudSat bin [Beneditte, 2003]. ECMWF produces global analysis for the four synoptic hours of 00, 06, 12 and 18 UTC each day. The numerical scheme is a TL511L60 (i.e., triangular truncation, resolving up to wavenumber 511 in spectral space and 60 vertical levels), and the horizontal resolution approximately is 40 km. Relative humidity with respect to ice is derived in Chapter 3 from the temperature, pressure and specific humidity profiles of ECMWF-AUX (Appendix 2.1). The detailed description of ECMWF-AUX is presented in Beneditte [2003] and CloudSat Project document [2008].

2.3 CloudSat and CALIPSO Hydrometeor Mask

The CloudSat and CALIPSO data described above were then analyzed to discriminate and classify the particle phase and shape. For this purpose, hydrometeor pixels were selected by the radar and lidar hydrometeor mask algorithm developed by Hagihara et al. [2010]. This mask was originally developed for ship-borne radar and lidar measurements and validated against the sky-camera data by Okamoto et al. [2007] and Okamoto et al. [2008] in the western Pacific Ocean near Japan and in the western tropics, respectively. Hagihara et al. [2010] later adjusted and extended this masking algorithm to CloudSat and CALIPSO measurements.

All the CloudSat, CALIPSO, MODIS and ECMWF data used in Chapters 3 and 4 are collocated onto CloudSat 240-m vertical and 1.1-km horizontal pixels according to the procedure described in Hagihara et al. [2010]. These data are known as “The CloudSat-CALIPSO Merged Dataset” and distributed from JAXA

A-Train Product Monitor (http://www.eorc.jaxa.jp/EARTHCARE/research_product/ecare_monitor_e.html).

2.4 Himawari-8 Aerosol Optical Thickness

For the development of the hourly combined aerosol algorithm in Chapter 5, aerosol optical thickness retrievals, named as $AOT_{original}$ in Chapter 5, were employed using L2 Aerosol Product (version β) from the JAXA Himawari Monitor (http://www.eorc.jaxa.jp/ptree/index.html). The product is in equal latitude-longitude grid of 0.02° with temporal resolution of 10 minutes. The aerosol pixels were discriminated from cloudy pixels using a cloud flag algorithm, CLoud and Aerosol Unbiased Decision Intellectual Algorithm (CLAUDIA), developed by Ishida and Nakajima [2009] and Ishida et al. [2011]. The CLAUDIA is a "neutral" cloud detection algorithm that avoid biased discrimination on either clear (including aerosol) or cloudy by using a number of pixel-by-pixel threshold tests. The aerosol optical thickness retrieval was based on the 2-channel method developed by Higurashi and Nakajima [1998] over ocean and Fukuda et al. [2013] over land. The details on the retrieval algorithm of $AOT_{original}$ is described in Appendix 2.2. In not specified, only minimum quality control was conducted in the $AOT_{original}$ dataset to extract as much aerosol information as possible for the hourly combined algorithm, where the following pixels were excluded: (1) pixels that were next to cloud pixels and (2) pixels whose solar zenith angle was more than 70° to avoid retrievals with low accuracy.

Appendix 2.1 Relative Humidity Respect to Ice

For the purpose to analyze ice supersaturation in Chapter 3, relative humidity respect to ice was derived from the temperature, pressure and specific humidity profiles of the ECMWF-AUX product, which provides ECMWF atmospheric state data interpolated along CloudSat pixels. The definition of relative humidity respect to ice, RH_{ice}, is

$$RH_{ice} = \frac{e_{wv}}{e_{si}} \times 100 \qquad \text{(A2.1)}$$

where e_{si} [Pa] is ice saturation pressure and e_{wv} [Pa] is water vapor pressure. In this study, the ice saturation pressure e_{si} is derived from Marti and Mauersberger [1993]

$$e_{si} = 10^{(\frac{a}{T}+b)} \qquad \text{(A2.2)}$$

where $a = -2663.5 \; and \; b = 12.537$. Note that Eq. (A2.2) is valid over the range -273.15°C < T < 0°C. The water vapor pressure e_{wv} [Pa] is derived from the equation of state for water vapor

$$e_{wv} = \rho_{wv} R_v T \qquad \text{(A2.3)}$$

where, T [K] is temperature and R_v [J/g/K] is the individual gas constant for water vapor (= 0.4615 J/g/K). Here, the water mass density ρ_{wv} [g/m^3] is calculated from the specific humidity, q, from the ECMWF-AUX product. The specific humidity q is the mass of water vapor per unit mass of moist air, which is described as

$$q = \frac{\rho_{wv}}{\rho_d + \rho_{wv}} \qquad \text{(A2.4)}$$

where ρ_d [g/m^3] is the mass density of dry air. Rearranging Eq. (A2.4) gives

$$\rho_{wv} = \rho_d \frac{q}{1-q} \qquad \text{(A2.5)}$$

From the equation of state for dry air,

$$\rho_d = \frac{p_d}{R_d T} = \frac{p - e_{wv}}{R_d T} \qquad \text{(A2.6)}$$

in which p_d [Pa] is partial pressure of dry air and p [Pa] is atmospheric pressure. R_d [J/g/K] is the individual gas constant for dry air (= 0.287 J/g/K). Therefore, substituting Eq. (A2.6) into Eq. (A2.5) gives

$$\rho_{wv} = \frac{p - e_{wv}}{R_d T} \frac{q}{1-q} \approx \frac{p}{R_d T} \frac{q}{1-q} \qquad \text{(A2.7)}$$

assuming $e_{wv} \ll p$ [Rogers and Yau, 1989]. Eq. (A2.7) is substituted into Eq. (A2.3) to calculate e_{wv}, which is then used to derive RH_{ice} from Eq. (A2.1).

Appendix 2.2 Himawari-8 Snapshot Aerosol Algorithm

The aerosol optical thickness from 10-minute observations of AHI ($AOT_{original}$) used in Chapter 5 was derived based on the algorithms by Higurashi and Nakajima [1998] and Fukuda et al. [2013], with adjustments to AHI's wavelength, geometry, and time interval. The details of the algorithms and its application to Himawari-8 are described in the following sections.

Appendix 2.2.1 Aerosol Model

The algorithm assumes the aerosol size distribution as a bimodal log-normal function [Dubovik et al., 2002; Smimov et al., 2003], which is described in the following equation:

$$\frac{dV}{d\ln r} = \sum_{n=1}^{2} c_n \, exp\left[-\frac{1}{2}\left(\frac{\ln r - \ln r_{mn}}{\ln \sigma_n}\right)^2\right] \qquad \text{(A2.8)}$$

where V is the column volume, r is the particle radius, and n is the mode number. On the basis of WCP-55 [1983], respective mode radius over land and ocean was defined as $r_{m1} = 0.17$ μm (fine mode) and $r_{m2} = 3.44$ μm (coarse mode) with deviations $\sigma_1 = 1.96$ and $\sigma_2 = 2.37$, respectively. The complex refractive index over ocean was set to $1.5 - 0.005i$ [Higurashi and Nakajima, 1998]. The complex refractive index over land was referenced from Fukuda et al. [2013], which used the sulfate model by WCP-55 [1983].

Appendix 2.2.2 Surface Reflectance Model

The estimation of the surface reflectance, R_{srf}, is one of the essential challenges in retrieving land aerosols from imagers. On the basis of Fukuda et al. [2013], the second lowest gas-corrected reflectance (hereafter referred to as the second minimum, R_{2ndmin}) was used as R_{srf} (i.e., $R_{srf} = R_{2ndmin}$) to avoid occasional interference by cloud shadows in the lowest reflectance. Furthermore, even taking the second minimum, R_{2ndmin} tended to be higher than expected due to residual aerosols over urban areas such as in China and Southeast Asia. Therefore, if the second minimum in the blue band (0.47 μm) was higher than the second minimum in the red band (0.64 μm), aerosol contamination was suspected, and the algorithm estimated R_{srf} by using the modified Kaufman method described in Fukuda et al. [2013]. This method derives R_{srf} by fitting a fourth-order function of the normalized difference vegetation index (NDVI) using the second minimum pixels from Australia (assuming aerosol loadings in Australia are more negligible compared with those in the Asian regions). To take into account the bidirectional reflectance distribution function (BRDF), the surface reflectance was calculated at every hour (i.e., the current 00 UTC minute's surface reflectance

was derived from the data of the previous hour's 10, 20, 30, 40, 50, and the current 00 UTC minutes) using the last 30 days of data and updated at every eight days.

Appendix 2.2.3 Lookup Table Construction

Based on the aerosol and surface model setting described above, the look-up-table (LUT) over land and ocean for each component in the following equation was constructed by using a radiative transfer simulation package called "the STAR series" [Nakajima and Tanaka, 1986; Ota et al., 2009]:

$$R_{sim} = \begin{cases} R_a + \frac{t_0 \cdot t_1 \cdot R_s}{1 - s \cdot R_s} & over\ land \\ R_a + T_0 \cdot T_1 \cdot R_g & over\ ocean \end{cases} \quad \text{(A2.9)}$$

where R_{sim} is the apparent reflectance with gas absorption correction at top-of-atmosphere, R_a is the atmospheric reflectance, t_0 is the total transmittance from the sun to the surface, t_1 is the total transmittance from the surface to the satellite sensor, s is the spherical albedo of the atmosphere, and R_s is the surface reflectance. T_0 is the direct transmittance from the sun to the surface, T_1 is the direct transmittance from the surface to the satellite sensor, and R_g is the specular reflectance from the ocean surface. The spectral response function of AHI provided by the Japan Meteorological Agency (JMA) (http://www.data.jma.go.jp/mscweb/ja/himawari89/space_segment/spsg_ahi.html) was used to apply the algorithm to the AHI.

Appendix 2.2.4 AOT Estimation

$AOT_{original}$ was retrieved by using AHI's full disk image at every 10 minutes. The original resolution of Himawari Standard Product distributed from the JMA was 0.5 km for the 0.64 μm band, 1 km for the 0.47, 0.51, and 0.86 μm bands, and 2 km for the longer wavelength bands. The radiances were averaged to 2km and then resampled to 0.02° grid for each wavelength of 0.47–0.86 μm to make the spatial representativeness consistent with the other bands. AOT over ocean was estimated from the 0.64 and 0.86 μm bands, and AOT over land was estimated from the combination of the 0.46, 0.51, and 0.64 μm channels. The 0.46 μm radiance was refrained from using in the ocean retrievals because it is often influenced by water leaving radiance and the shorter wavelengths were used for land since they are more sensitive to aerosol signals and the surface is too bright for aerosol retrieval at the near-infrared channel. The measured radiances were compared with the simulated R_{sim} given in Eq. (A2.9) to search for the best estimate of AOT by the optimal estimation [Rogers, 2000] based on Bayes' theory, which was implemented by using the Levenberg–Marquardt method.

Chapter 3 Comparison of Global and Seasonal Characteristics of Cloud Phase and Horizontal Ice Plates Derived from CALIPSO with MODIS and ECMWF

3.1 Motivation

Building upon the advancement in the remote sensing technique of cloud particle habit from space during the last decade, the global and seasonal characteristics of cloud phase and its orientation was first studied for deeper and more comprehensive understanding of their behaviors in the atmosphere. The cloud phase and ice crystal shape (hereafter, cloud particle type) classification is estimated using CALIPSO/CALIOP observation and a retrieval algorithm originally developed by Yoshida et al. [2010] with a few additional modifications considered in this study. The objective of this chapter is to investigate the fundamental characteristics of cloud particle habit in various temporal (e.g. daytime/nighttime, seasonal) and spatial (e.g. land /ocean, zonal) scales. The cloud particle types are compared with (1) a different discrimination scheme from the same CALIOP observation [NASA Vertical Feature Mask (VFM) product]; (2) a different observation [MODIS imaging sensor onboard Aqua satellite]; and (3) environmental conditions offered by a numerical model (ECMWF). The analysis period was extended to one year (September 2006 to August 2007) from the three months analysis in Yoshida et al. [2010], enabling to reveal for the first time the global seasonal characteristics of the particle habits. Note that the context of this chapter is published in Hirakata* et al. [2014].

3.2 CALIPSO Cloud Particle Type Discrimination

Several cloud phase/particle type estimations have been developed based on the lidar measurement of the depolarization ratio and the backscattering coefficient from CALIOP observations [Hu et al., 2009; Yoshida et al., 2010; Cesana and Chepfer, 2013]. In this study, the cloud particle type classification algorithm originally developed by Yoshida et al. [2010] was employed. In this section, I briefly describe the algorithm and the changes made from Yoshida et al. [2010].

3.2.1 Algorithm Basis

In Yoshida et al. [2010], cloud particle types are discriminated by calculating two parameters, depolarization ratio δ and total backscattering attenuation χ, for each cloudy pixel defined by Hagihara et al. [2010]

Hirakata is Kikuchi's maiden name.

(Chapter 2.3) in 1.1km horizontal and 240m vertical resolutions. The first parameter, δ, is defined as

$$\delta = \frac{\beta_{perp}}{\beta_{parallel}} \times 100 \quad [\%] \tag{3.1}$$

where β_{perp} and $\beta_{parallel}$ are the attenuated backscattering coefficients at the 532 nm perpendicular and parallel channels, respectively. $\beta_{parallel}$ is derived by subtracting β_{perp} from the total attenuated backscattering coefficient. δ is known to vary significantly with the particle orientation: horizontally oriented ice plates give lower δ, whereas randomly oriented ice crystals give higher δ. It should be noted, however, that although spherical water droplets give low δ values in single scattering regimes, large values are observed in satellite observations where the penetration depths were large (as in the 240 m vertical resolution of this study) due to the larger footprint and resultant greater multiple scattering as opposed to ground-based lidar observations [Yoshida et al., 2010]. This makes it difficult to discriminate water and randomly oriented ice from satellite measurements using δ alone.

Hence this issue was overcame by introducing the second parameter χ. The parameter quantifies the lidar attenuation that discriminates water and randomly oriented ice for a given δ. χ is defined as

$$x(R_i) = \log_{10}\left\{\frac{\beta_{total}(R_i)}{\beta_{total}(R_{i+1})}\right\} \tag{3.2}$$

where $\beta_{total}(R_i)$ and $\beta_{total}(R_{i+1})$ are the attenuated backscattering coefficients from *i*th and *i+1*th layer, respectively. Assuming the microphysical properties of the two vertically successive layers are homogeneous, the ratio of attenuated backscattering of two successive layers could be related to the extinction (σ) of the target layer:

$$\frac{\beta_{total}(R_i)}{\beta_{total}(R_{i+1})} = \exp\{2\sigma(R_i)\Delta R\} \tag{3.3}$$

From Eq. (3.2) and (3.3), the relationship between χand σ can be obtained:

$$\sigma(R_i) = \frac{1}{2\Delta R \cdot \log_{10} e}\, x(R_i) \tag{3.4}$$

This equation indicates that the parameter χcan be used as a proxy of extinction at the wavelength of 532 nm in a target cloud layer. If the two vertically successive layers have similar homogeneity, ice clouds are expected to have a smaller extinction, meaning lower χ, than water clouds.

One may argue that the vertical inhomogeneity within 240 m bin could induce large value of χ in ice cloud, which may exceed the threshold of the water detection, leading to the misclassification of ice to water. However, Yoshida et al. [2010] suggest that the misclassifications due to vertical inhomogeneity of cloud are exceptionally rare (see their Figs. 2 and 3). Their Fig. 2 is the χ-δ diagram of frequency distributions of clouds and in Fig. 2a (where temperature ≥ 0°C and liquid water particles were dominant), the majority of cloud frequency (≥ 0.075 in yellow) lay in $\chi \geq 0.5$. In contrast, Fig. 2c (where temperature $\leq$ -20°C and ice particles were dominant), the majority of cloud frequency lay in $\chi \leq 0.25$, showing a clear difference from water. Even near $\chi = 0.25$ where water and ice may share the same χ values, the lidar classification also uses δ to separate water and ice (as in their Fig. 3). In fact, the water-ice separation line was set at χ over 0.5 (and not at 0.0) which implies that the vertical inhomogeneity was taken into account. The region which can induce the most ambiguity was assigned as an unknown type.

The second step of the particle type discrimination is the spatial continuity test, which is very similar to the procedure taken in the cloud-masking scheme. Here, 15 bins (3 vertical bins × 5 horizontal bins) around the target bin are considered. Then, the particle type that are most prevalent in the 15 bins is assigned to the target bin in the center. If there are more than two types that dominated within the 15 bins, then the target cloud type is assigned in the following order: water, 3-D ice, 2-D plate, mixture, unknown1, and unknown2. To check the adequacy of this minor rule, I used one month of data (June 2006) and found that the ratio of water cloud to ice cloud decreased from 18.1% to 16.7% when the preference order was changed to unknown2, unkown1, mixture, 2-D plate, 3-D ice and water, showing that even if there were two dominant particles, the type assignment did not significantly change the water versus ice cloud discrimination. Note that 2-D plate defined here refers to clouds that include quasi horizontally oriented ice plates. 3-D ice is accepted to be included in the 2-D plate category because even a small amount of 2-D plate induces small depolarization ratio due to its strong backscatter [Zhou et al., 2012] and there is a possibility that 3-D ice is included in the volume. Lastly, the “water” pixels that are above 0°C was further discriminated into “warm water”, and that are below 0°C are discriminated into “supercooled water”.

Consequently, the original version of cloud particle type discrimination (i.e., Yoshida et al. [2010] algorithm) discriminates particle types into warm water, supercooled water, 3-D ice, 2-D plate, unknown1 and unknown2.

3.2.2 Modifications from Previous Study

The algorithm in this paper included two modifications from Yoshida et al. [2010]. First, I revised the discrimination scheme to replace the original “unknown 1” type to the “mixture of 3-D ice and 2-D plate” type. To confirm the adequacy of this change, one month of data in September 2006 was used to investigate which particle type was assigned at the consecutive pixels just above and below the original unknown 1

type. The result showed that over 92 % was an ice type (either 3D-ice or 2D-plate) and only less than 8% was a liquid type (either warm or supercooled water). Thus, the majority of this type was suggested to contain either or mixture of the two ice categories and that a sudden phase change at the unknown 1 pixel was considered rare. This also gave an implication that liquid water particles induce higher depolarization ratio and lidar attenuation than those given in the unknown 1 region. Therefore, the original unknown 1 type was categorized to a new type: "Mixture of 3D-ice and 2D-plate". Consequently, the original unknown2 defined by Yoshida et al. [2010] was changed to the unknown1. When a pixel of either of the two successive layers were missing, it was difficult to calculate $\chi$and therefore would not be able to determine its particle type. Consequently, the corresponding pixels were assigned as the new type, unknown2. Second modifications were to reprocess the lidar data (backscattering coefficient, cloud mask, cloud particle type) due to the update of the CALIPSO L1b data from version 2.01 to version 3.2. Fig. 3.1 shows the χ–δ planes with the new classification scheme overlaid.

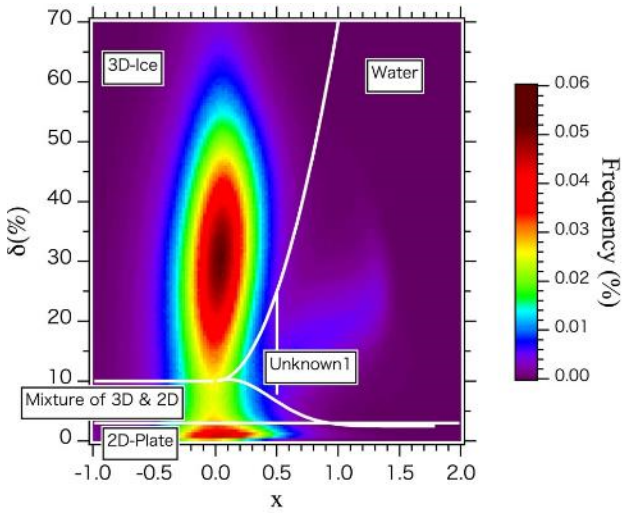

Figure 3.1 Cloud particle diagram on the $\chi$and δ planes. The colors denote the occurrence frequencies of the observations during October 2006 at all temperatures. In the figure, the original "unknown1" in Yoshida et al. [2010] was replaced to "Mixture of 3D-ice and 2D-plate" and, consequently, the original "unknown2" was replaced to "Unknown1".

Given the general correspondence of δ and χ to particle orientation and extinction, and modifications from Yoshida et al. [2010] described above, hydrometeor particle types are classified into the following seven categories: warm water, supercooled water, 3D-ice, 2D-plate, a mixture of 3D-ice and 2D-plate, unknown1, and unknown2. Unknown1 could include all types of clouds. Both unknown1 and unkown2 were negligible from June 2006 to May 2007, at less than 0.2% and 0.04% of total clouds, respectively.

3.2.3 Case Study

Shown in Fig. 3.2 is an example case of hydrometeors measurement by CALIPSO/CALIOP, CloudSat/CPR, and Aqua/MODIS, observed on 13 September 2006 over the Arctic.

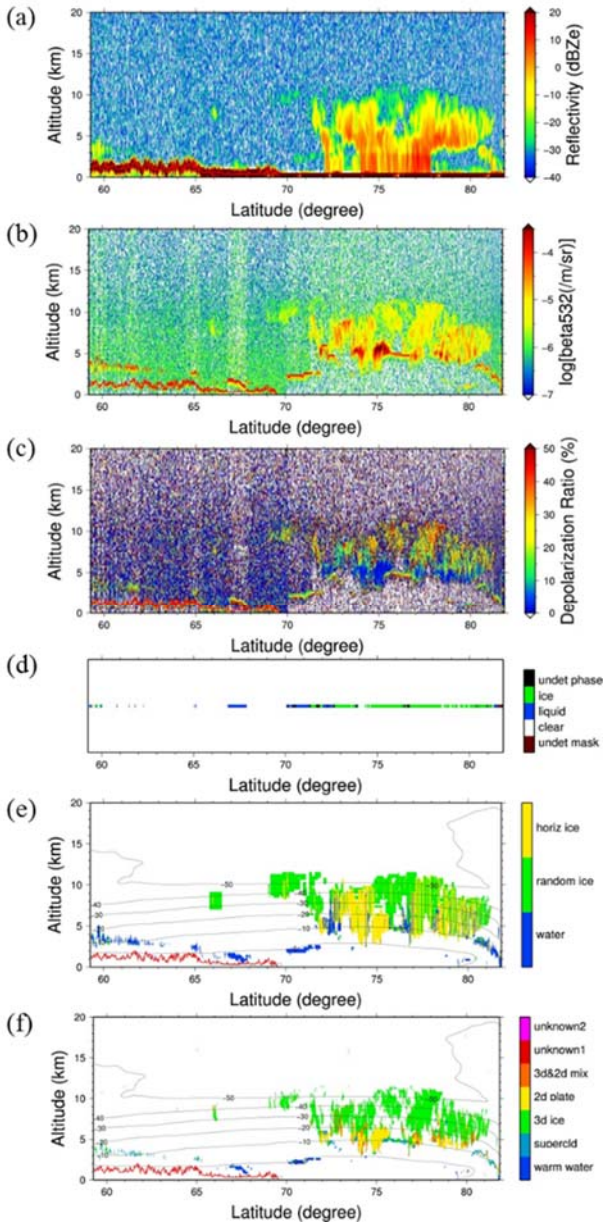

Figure 3.2 An example of a latitude–height cross section of (a) the CloudSat radar reflectivity; (b) the CALIPSO lidar backscattering coefficient; (c) the CALIPSO depolarization ratio; (d) MODIS cloud phase discrimination; (e) the cloud phase discrimination derived from the NASA VFM; and (f) the cloud particle type discrimination derived from this study. The observation was made around 2025UTC on 13 September 2006 over the Arctic (59°– 82°N, 131°– 151°E).

A large deep cloud system accompanying precipitation can be recognized at higher latitudes (72°–82° N). As expected, CPR was able to detect the precipitation, whereas CALIOP was strongly attenuated by the clouds above. On the other hand, at lower latitudes (60°–63° N and 65°–68° N), CALIOP detected thin broken clouds that were missed by CPR. This is the first orbit-to-orbit comparison of phase discrimination by MODIS and VFM (Figs. 3.2d–3.2f). Due to the differences between active and passive sensors, the CALIOP classification shows two-dimensional cross sections of clouds, whereas MODIS only shows one-dimensional line, which was selected from the horizontal measurement of MODIS along the CloudSat/CALIPSO orbit. The cloud particle type classification from this study shows that the majority of clouds below -20°C were 3-D ice. In contrary, between -20°C and 0°C, the 2-D plate and supercooled water became the dominant cloud particle type, with only a few 3-D ice classifications. The method by Hu et al. [2009] discriminates particle types by layer-integrated backscattering coefficient and depolarization ratio. Hence the scheme in VFM is not designed to provide vertically resolved cloud particle type. As a result, VFM water and ice discrimination in Fig. 3.2 seemed to vary from one record to the next. In addition, due to this vertical integration, there were cases where VFM overestimated the horizontally oriented ice regions, giving 2-D plate to be registered at low backscattering signals and high depolarization ratios (73°–76° N). 2-D plate in general produce larger backscatter and smaller depolarization than 3-D ice but some portion of horizontally oriented ice in VFM does not show such features due to the possible misclassification of randomly oriented ice to horizontally oriented ice. Some of the 2-D plate existing at temperatures as low as -40°C also seems to be unrealistic and inconsistent with previous findings [e.g. Zhou et al., 2013].

Since the algorithm in the present study employs pixel by pixel classification, the retrievals from this study reflected the fine structure of water, 2-D plate and 3-D ice in the clouds. The overall phase classification showed a good agreement between MODIS and this study, as shown in clouds at the high latitudes (67°–68° N and 73°–81° N). Interestingly, this case study also showed changes in the MODIS phase estimation in the regions where water and ice clouds overlapped. In the highest latitudes (73°–81° N), the ice clouds seemed to be thick enough for MODIS to detect, even where the water clouds existed underneath. On the other hand, at around 71.5° N, where water and thin ice clouds were overlapped, MODIS determined the phase to be water, which was due to CALIOP's capability in detecting optically thin clouds that are often missed by MODIS. Further, some of thin water clouds around 60°– 65° N were missed by MODIS whereas CALIPSO succeeded in detecting them and giving phase classification in both the present study and the VFM. There were a few undetermined MODIS phases where water and ice clouds with similar thicknesses overlapped (71.7°–71.9° N and 76.5°–76.8° N).

3.3 Cloud Particle Type Patterns

3.3.1 Day–Night Differences

Next, differences in cloud particle type classifications between daytime and nighttime was examined. In general, due to the background signals from scattered sunlight, daytime data gave much lower signal-to-noise ratios (SNR) than nighttime [Hunt et al., 2009]. Hence Hu et al. [2010] applied horizontal averaging scheme up to 80 km to increase signal-to-noise ratio. To confirm the adequacy of the pixel-by-pixel discrimination in this study to identify detailed cloud structure, the consistency of cloud particle type frequencies between day and night was investigated, in an assumption that the actual day–night variation was small for cloud particle types observed by CALIPSO.

The latitude–temperature cross section of three-dimensional cloud occurrence frequencies was investigated for day and night from September 2006 to August 2007 (Fig. 3.3). The three-dimensional cloud occurrence frequency of a cloud particle type was defined as the total number of the cloud particle type event divided by the total number of observation. Here, the "three-dimensional" cloud occurrence was called to differentiate from the traditional "two-dimensional" cloud coverage. The frequencies were calculated for warm water, supercooled water, 3-D ice, and 2-D plate. The latitude and temperature resolutions were 2.0° and 2.0°C, respectively. Relatively consistent cloud frequencies between day and night were found in warm water, supercooled water and 2-D plate, although slightly stronger frequencies were observed around the equator at night compared to day for supercooled water and 2-D plate (~0.02). Differences between daytime and nighttime cloud occurrence frequencies were seen in 3-D ice at all latitudes. It is worthy to mention that two peaks of the 3D-ice frequencies were recognized in the midlatitudes at low temperatures (~-75°C) in both daytime and nighttime, which were also seen in the previous CALIPSO analysis [Fig. 5 of Yoshida et al., (2010)], in the ECMWF supersaturation (Fig. 3.10 in this chapter) and in a climate model [Fig. 12 of Cesana and Chepfer, (2013)]. Although these peaks were not apparent in the latitude-altitude cross section (c.f. Fig. 4.8 in Chapter 4), they were considered to be formed as independent cloud systems from the cloud layers at the higher temperatures, which was oppose to the tropical cloud systems where the frequencies were continuous until temperature was as low as -80°C. Scatter plot of the frequencies in daytime and nighttime for each cloud particle type are further shown in Fig. 3.4, showing the quantitative differences in the overall cloud occurrence frequencies regardless of temperature and latitude. Each point in Fig. 3.4 indicates a cloud occurrence frequency at a specific latitude and temperature in Fig. 3.3. Despite the larger background signals in daytime, the scatter plot of water (both warm and supercooled) and 2-D plate showed very good agreement between day and night, suggesting that large background signals were effectively removed in the algorithms. The slope of the linear regression was 0.90 for warm water, 0.92 for supercooled water, and 1.09 for 2-D plate. In addition, the correlation coefficients were 0.96 for warm water, 0.95 for supercooled water, and 0.99 for 2-D plate. The 3-D ice cloud occurrence frequency during the nighttime

was found to be higher than that of daytime [Figs. 3.3 (a-3) and (b-3)], similar to what was found for total cloud occurrence (figure not shown). If this was due to the misclassification of 3-D ice from another type, then the decrease in the 3D-ice frequency during daytime should have been appeared as an increase in the frequency of other types. Since this was not the case, it was likely due to the combined effect of (1) the degradation of cloud detectability in the daytime from the low signal-to-noise ratio, and (2) the change in the cloud detection from the actual diurnal cycle of clouds, rather than the misclassification in cloud particle type scheme.

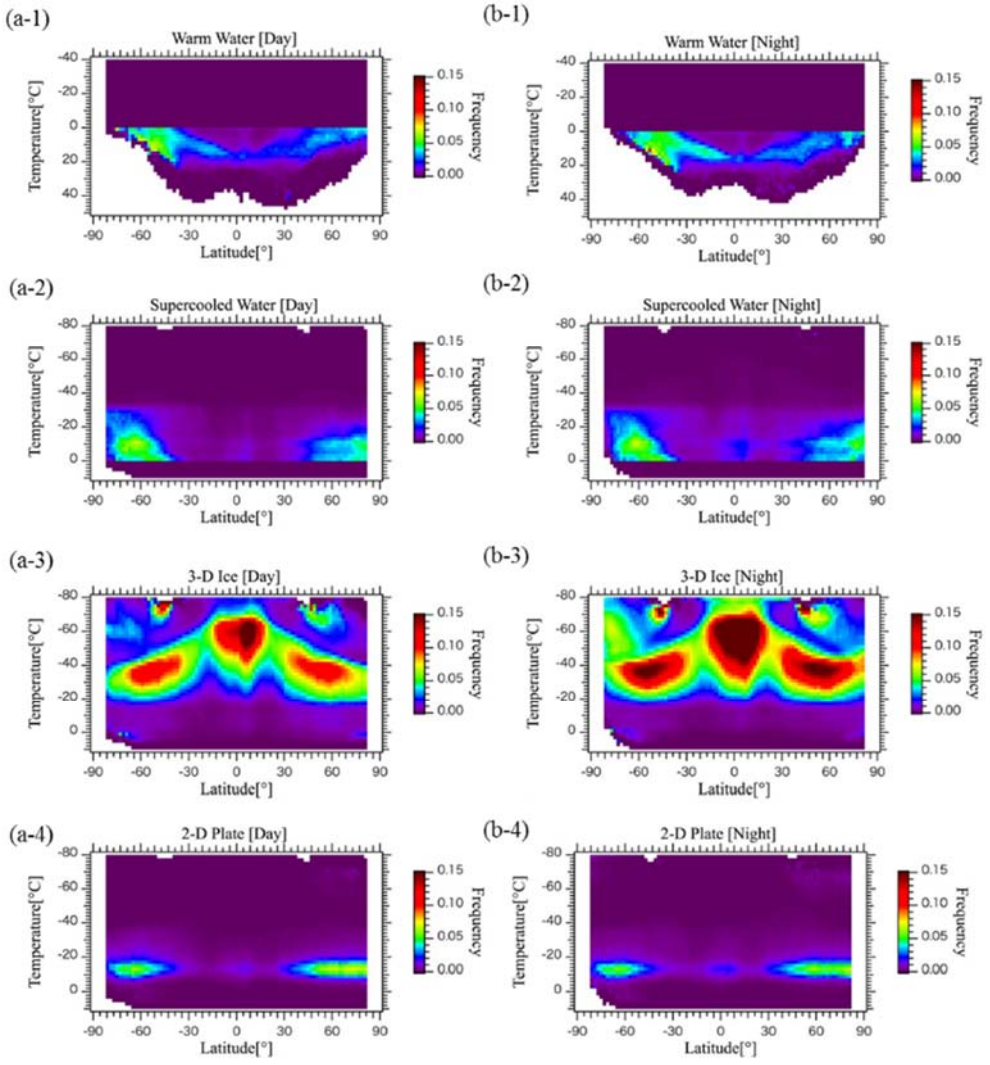

Figure 3.3 Latitude versus temperature distribution of occurrence frequency for (1) warm water; (2) supercooled water; (3) 3-D ice; and (4) 2-D plate for (a) daytime and (b) nighttime during September 2006 and August 2007. Note that the temperature ranges for vertical axes were -40°C < T < 50°C for warm water and -80°C < T < 10°C for all others.

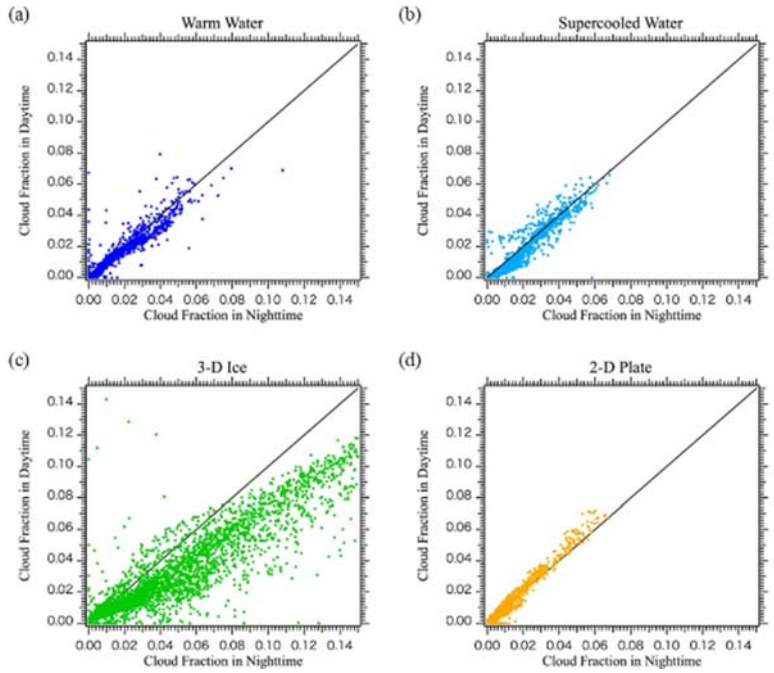

Figure 3.4 Correlation of each cloud particle type occurrence frequency between daytime and nighttime. (a) warm water; (b) supercooled water; (c) 3-D ice; and (d) 2-D plate.

Shown in Table 3.1 is the global mean cloud occurrence frequency to summarize the day – night comparisons for each type. The global mean cloud occurrence frequency of a cloud particle type at nighttime (daytime) was defined as the total number of the cloud particle type events in nighttime (daytime) divided by the total number of observation in nighttime (daytime), from surface to approximately 20km altitude. The global mean cloud occurrence frequency for 3-D ice was 1.6 times higher in nighttime than in daytime (4.1×10^{-2} for night and 2.6×10^{-2} for day). On the other hand, the frequencies in night and day was similar in the rest of the types. The global mean cloud occurrence frequency in nighttime was 0.95 times that of daytime for warm water (2.4×10^{-3} for night and 2.5×10^{-3} for day), 1.2 times higher for supercooled water (4.8×10^{-3} for night and 4.0×10^{-3} for day) and 1.04 times higher for 2-D plate (3.2×10^{-3} for night and 3.1×10^{-3} for day).

Table 3.1 Global mean cloud occurrence frequency for warm water, supercooled water, 3-D ice, and 2-D plate during day and night.

	Night	Day
warm water	0.0024	0.0025
supercooled water	0.0048	0.0040
3-D ice	0.041	0.026
2-D plate	0.0032	0.0031

3.3.2 Dependence of Cloud Particle Type on Temperature

Given the strong dependence of cloud particle phase/type on temperature shown by the fundamental laboratory experiments [Libbrecht, 2005], the dependence of the cloud particle type on ambient temperature was investigated in this study from the global cloud measurements (Fig. 3.5). The phase dependency on temperature was represented by the occurrence ratio of each cloud particle type at a given temperature, defined as the number of cloud particle type observations divided by the total number of clouds. The occurrence ratio was calculated from September 2006 to August 2007 at the temperature resolution of 0.25°C. As expected, the water ratio (sum of warm water and supercooled water) tended to increase as temperature increased, whereas the ice ratio (both 3-D ice and 2-D plate) started to increase at temperatures below 0°C. The freezing temperature at which water occurrence ratio become 50% was found at about -10°C. It is well known from laboratory experiment, ground observations and numerical simulations that mixed-phase clouds exist at temperatures between 0°C and -40°C [Rogers and Yau, 1989; Rauber and Tokay, 1991; Shupe et al., 2006]. The result of the 2D-plate agreed with the analysis on the temperature dependency of horizontally oriented plates by Zhou et al. [2013], and with Zhou et al. [2012] in the perspective that the existence of quasi-horizontally oriented plates is higher at warm temperatures over -35°C than at the colder temperatures. On the other hand, the result from Zhou et al. [2012] may infer that the fraction of 2-D plate contains relatively small portion in the cloud as their method used layer integrated depolarization ratio and attenuated backscatter. Okamoto et al. [2010] showed that ice water content retrievals become overestimated when 2-D plate is not considered. Note that the present scheme may not exactly coincide with previous work on mixed phase clouds because the present results did not accept the coexistence of water and ice, and only one cloud particle type was accepted in the ideal CloudSat grid box. The errors in temperatures and algorithms may also induce the discrepancy between the current and the previous results. In this scheme, 3-D ice existed at temperatures over 0°C and these particles may have been due to the transport of ice particles from colder temperatures. Considering that dendrites, needles and columns correspond to 3-D ice in this study, the results generally agreed with previous findings in the existence of plate crystals (with dendrites) at $-20°C < T < -10°C$, and with needles and columns being dominant at $-10°C < T < 0°C$ and $T < -20°C$ [Pruppacher and Klett, 1997].

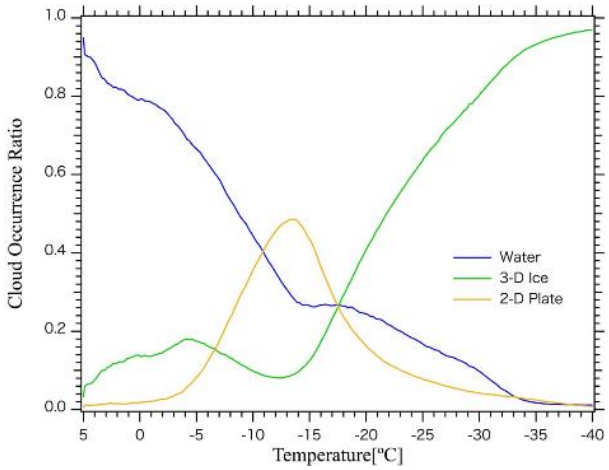

Figure 3.5 Annual mean occurrence ratios of cloud particle type with respect to total clouds from September 2006 to August 2007.

3.3.3 Land–Ocean Differences

The latitude–altitude cross section of three dimensional water and ice cloud occurrence frequencies over land and ocean was investigated (Fig. 3.6). Note that water was defined as the sum of warm water and supercooled water, and that ice was defined as the sum of 3-D ice, 2-D plate and mixture of 3-D ice and 2-D plate.

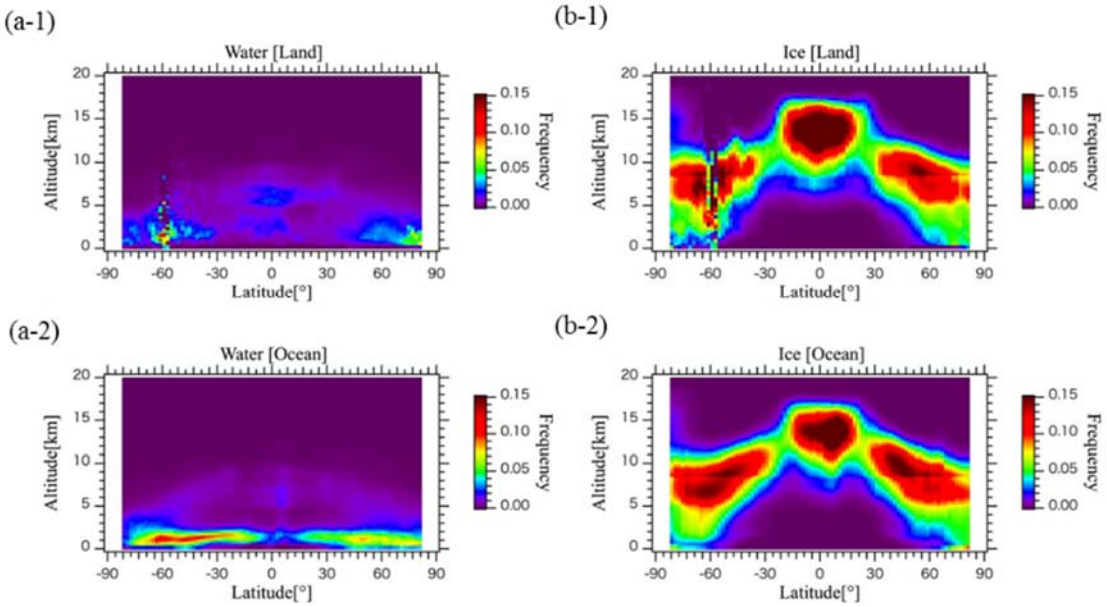

Figure 3.6 Latitude–temperature distribution of: (left) water and (right) ice cloud occurrence frequency from September 2006 to August 2007 over: (top) land and (bottom) ocean.

The definition of the three dimensional cloud occurrence frequency and the latitude resolution were same as that in Fig. 3.3, although the statistic here included both day and night observation in each panel. The altitude resolution was set to 240 m. The discontinuity of phase distribution around latitude -60° over land (Figs. 3.6 (a-1) and (b-1)) is caused by the limited number of sampling due to the lack of land over the Southern Ocean.

As mentioned in Yoshida et al. [2010], the maximum altitude at which water could be observed depended on the latitude; the maximum altitude generally became higher as the latitude decreased. This arch-like shape of the water occurrence frequency corresponded to the temperature at which supercooled water can exist. Yoshida et al. [2010] stated that the water cloud fraction became close to zero (< 2%) below -40°C. Very cold water (< -40°C) was not found in either land or ocean in this analysis. Fig. 3.6 illustrates the significant contrast between land and ocean at altitudes below 3 km. The annual mean water occurrence frequency below 3 km over ocean was almost double the frequency over land (3.7×10^{-2} over ocean and 1.9×10^{-2} over land), attributed to the larger supply of water vapor and weaker upward velocity over ocean compared to land. In contrast to water, the annual mean ice occurrence frequency did not differ significantly between land and ocean (4.0×10^{-2} for land and 3.7×10^{-2} for ocean in 0-18 km altitude). Note that stronger upward air motion over land did not significantly affect the ice cloud occurrence, although a distinct difference in ice water content (IWC) was found, with higher IWC over land than over ocean [Okamoto et al., 2010].

3.4 Comparisons with VFM, MODIS and ECMWF

3.4.1 Cloud Coverage Comparisons with VFM and MODIS

Prior to this study, Yoshida et al. [2010] studied the global daytime monthly mean cloud coverage of cloud phase with that of MODIS Level 3 data products (MYD08_M3) during September and November 2006. Here, the zonal mean phase coverages during the same period were examined by the pixel-by-pixel matchup of cloud phase retrievals from this study, VFM and MODIS, instead of comparing the monthly mean products as done in Yoshida et al. [2010] (Fig. 3.7). The cloud coverage corresponds to the traditional two-dimensional cloud occurrence frequency and the zonal mean cloud coverage for water at a latitude was defined as the total number of water cloud that was observed at topmost pixels in topmost layer divided by the total number of observation profile at the corresponding latitude. The definition is same for ice and total cloud. Here, only the topmost pixels were considered for this study and VFM, and only the daytime data were accepted because MODIS retrieves phase classification using the visible channels, which were only available in daytime. The water cloud in this study was defined as the sum of warm water and supercooled water, and the ice cloud was defined as the sum of 3-D ice, 2-D plate, and mixture of 3-D ice and 2-D plate. The ice cloud for VFM was defined as the sum of “randomly oriented ice” and “horizontally oriented ice”

in their definition. The latitude resolution was set to 2.0°. In general, the zonal mean cloud coverage for all three schemes distributed similarly (Fig. 3.7): (1) the enhancement of ice clouds was seen in the tropics due to the upward branch of the Hadley cell at about 8°; (2) the low ice cloud coverage was identified in the subtropical high pressure belt at around -20° and 23°; and (3) enhancement of both ice and water clouds was indicated at higher latitudes (about 60°) in the known storm track regions of both hemispheres.

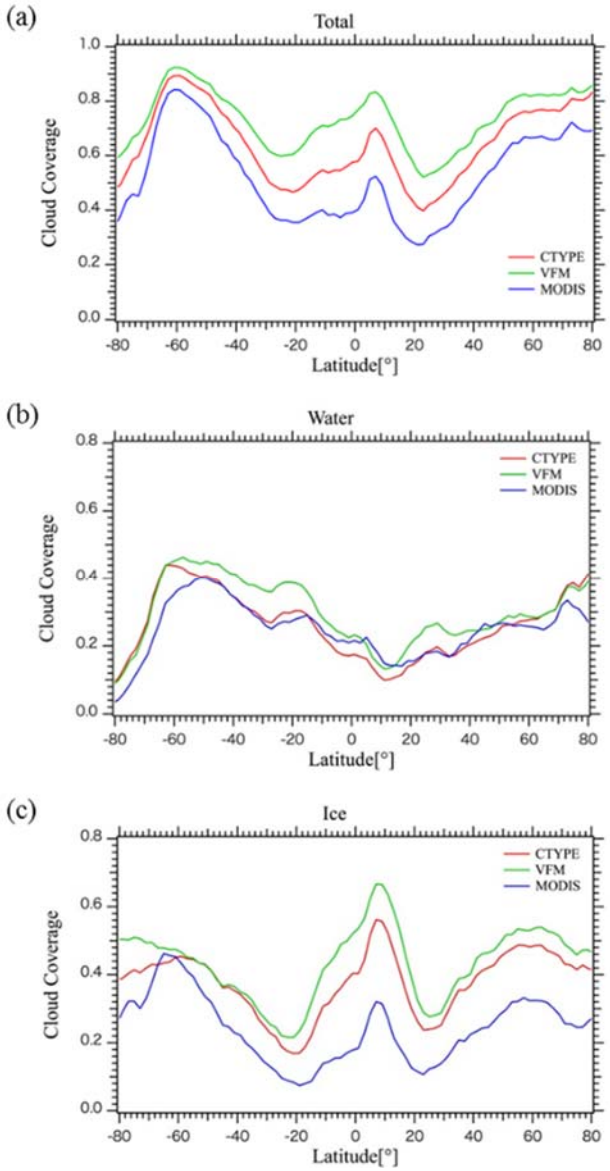

Figure 3.7 Zonal mean daytime coverage of MODIS (blue) and zonal mean daytime coverage of topmost pixels of cloud particle type from this study (red) and VFM (green) for (a) ice; (b) water; and (c) total cloud during September and November 2006.

The zonal mean cloud particle type cloud coverage for water ranged between 0.2 to 0.4 and was in good agreement with MODIS and VFM except at high latitudes where MODIS seems to have underestimated. The MODIS ice cloud coverage was much lower than that from the two CALIOP retrievals, and this reflected the difference in the cloud detection sensitivity between CALIOP and MODIS. In contrast, the zonal mean VFM cloud coverage was generally higher than that obtained from this study, and one of the reasons for this was suspected to be due to the horizontal averaging scheme in VFM until they detected a "feature" (either aerosol or cloud) [Vaughan et al. 2005], leading to extend the maximum horizontal resolution of the clouds to 80 km. In addition, recent studies demonstrated that VFM often misclassified noise or aerosols as clouds [Holz et al., 2008; Marchand et al., 2008; Hagihara et al., 2010; Rossow and Zhang, 2010].

Next, the correlation between cloud particle type, VFM, and MODIS was analyzed by deriving scatter plots of the cloud phase coverage from this study and VFM against MODIS, showing the differences in the relationship of VFM and the present study to MODIS (Fig. 3.8). Each plot in Fig. 3.8 represents the zonal mean cloud coverage at specific latitude in Fig. 3.7. For ice clouds, the present study and VFM generally had larger cloud coverage than MODIS, due to the low sensitivity of MODIS to thin cirrus clouds as discussed earlier. The cloud particle type estimation from this study had better ice cloud correlation with MODIS than VFM (correlation coefficient was 0.82 for the present study and 0.27 for VFM). For zonal mean water coverage, the present study and MODIS were in good agreement, and the slope of the linear regression was 1.06. Where MODIS water coverage was lower than that obtained from this study, it was likely due to the difficulty in the passive MODIS instrument to observing clouds especially at high latitudes over bright surfaces induced from accumulated snow [Wang et al., 2013], which was also seen in Fig. 3.7b. On the other hand, there were some plots where MODIS water coverage was larger than the present study, which may have been attributed to MODIS classifying the phase as water when water and ice clouds overlapped (c.f. Fig. 3.2). The correlation coefficients for water clouds were better in VFM (0.92) than in cloud particle type (0.88). The linear regressions for cloud particle type and VFM had slopes of 1.06 and 1.20, and the offset was 2.1×10^{-3} and 2.5×10^{-2}, respectively.

Although a number of climate model evaluation studies treat satellite measurements as a "truth" [e.g. Probst et al. 2012], this study underscores that there are uncertainties in satellite retrievals, which are attributed to differences in sensitivity of sensors and algorithm schemes. From Figs. 3.7 and 3.8, these uncertainties are considered to be larger in ice clouds than water clouds, which further imply a necessity of different treatments in satellite retrievals depending on their cloud phase in the evaluation of numerical models.

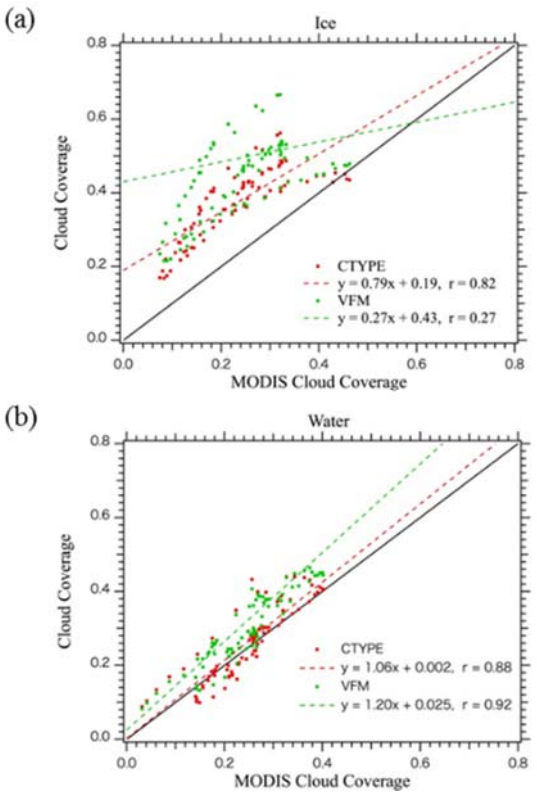

Figure 3.8 Scatter plot of Fig. 3.7; MODIS zonal mean cloud coverage versus zonal mean cloud coverage of cloud particle type from this study (red) and VFM (green) for (a) ice and (b) water.

3.4.2 Seasonal Characteristics of Ice Clouds from CALIPSO and Supersaturation from ECMWF

Supersaturation is a key parameter in cloud formation. A number of studies [Ovarlez et al., 2000; Tompkins et al., 2007; Rädel and Shine, 2010] have compared ice supersaturation from ECMWF with cloud occurrence from in situ measurements and found relatively good agreement. In this paper, ice cloud occurrence was examined over the globe against ice supersaturation occurrence derived from ECMWF data.

Shown in Fig. 3.9 is a case study comparing the cloud particle type retrieval result with ECMWF relative humidity respect to ice. Here, the relative humidity is derived from pressure, temperature and specific humidity profiles given in ECMWF-AUX product (Appendix A2.1). In this case, the observation was made over the Antarctic Ocean (59°–30° S, 165°–153° E) on 1 April 2007. Note that ice relative humidity was not calculated at temperatures over 0°C. Below the freezing level, the region where ice clouds were retrieved in this studygenerally matched with the region where ice relative humidity was high (over 80%). However, the relative humidity did not exceed 100% even though the current scheme (and VFM; figure not shown) identified cloudy regions. This is likely due to the underestimation of water vapor density when

expanding the subgrid-scale water vapor density to its large-scale in ECMWF [Tompkins et al., 2007].

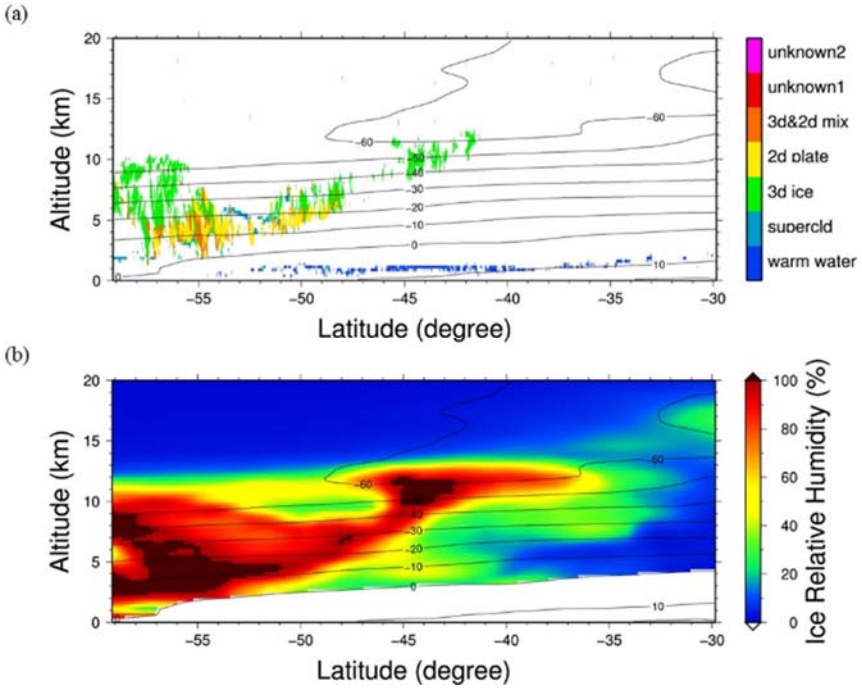

Figure 3.9 An example of (a) cloud particle type discrimination derived from this study and (b) relative humidity derived using ECMWF data. The observation was made around 0308UTC on 1 April 2007 over the Antarctic Ocean (59°–30° S, 165°–153°E).

The seasonal differences in the global three-dimensional ice cloud occurrence frequency obtained from this study was then compared with the ice supersaturation occurrence frequency derived from ECMWF data during September and August 2007 (Fig. 3.10). The definition of three-dimensional occurrence frequencies, latitude and temperature sampling was same as that defined in Fig. 3.3. The definition of the “ice cloud” for this study was same as that defined in Fig. 3.7.

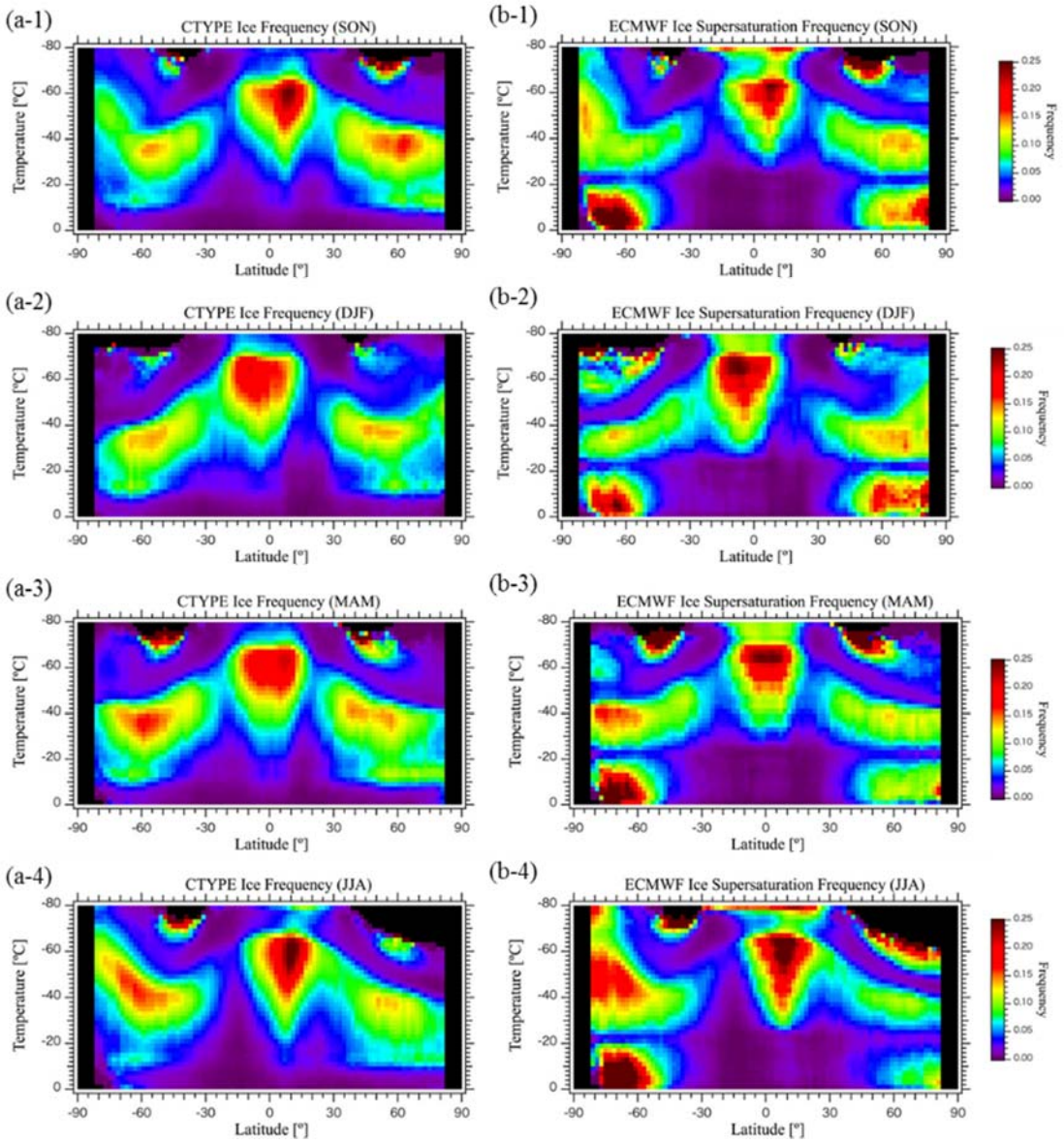

Figure 3.10 The seasonal dependency of global ice cloud occurrence frequency derived from this study (left) and ice supersaturation occurrence frequency derived from ECMWF (right) in September - November 2006 (top), in December 2006 - February 2007 (second row), in March - May 2007 (third row), and in June - August 2007 (bottom). The temperature and latitude resolutions were 2.0°C and 2.0°, respectively.

Overall, the magnitude of zonal mean ice occurrence frequency from the present study was similar to the ice supersaturation frequency of ECMWF. Both results showed similar seasonal characteristics. Large occurrence frequencies were recognized around -60°C of the equator in all seasons. The location of the maximum ice fraction moved from ~9°N in SON to ~9°S in DJF, then back to ~7°N during MAM and JJA,

which was considered to correspond to the movement of the Intertropical Convergence Zone (ITCZ). In addition, exceptionally low occurrence frequencies were recognized in both results around 15° of both hemispheres during DJF, although their magnitudes were much lower around 0.05 (possibly stronger subduction) at 15° N than at 15° S. Similarly, low occurrence frequencies around 15° were found in both hemispheres during JJA, although their magnitudes were much lower at 15° S (0.03) than at 15° N. The overall frequency pattern agreed well between the schemes, showing similar seasonal dependencies, especially at temperatures colder than -20°C. A relatively high supersaturation frequency could be recognized at the temperatures above -20°C in high latitudes (over 50° in both hemispheres), which could be due to (1) the lidar attenuation and (2) a possible disagreement between ice cloud measurement and ice supersaturation condition attributed to the formation of supercooled water instead of ice at high ice supersaturation.

The comparisons between the cloud particle type and ice super saturation were summarized in the form of their scatter plots in Fig. 3.11. Each point represents a frequency at a specific latitude and temperature from September 2006 to August 2007. The latitude and temperature resolutions were 2.0° and 2.0°C, respectively. The slope of the linear regression was low (0.28) when the calculations used the entire temperature range. However, when the temperature range was restricted to -60°C ≤ T ≤ -30°C to take into account the lidar attenuation and a possible supercooled water formation as explained above, better agreement was obtained with the slope of the linear regression of 1.02 (figure not shown).

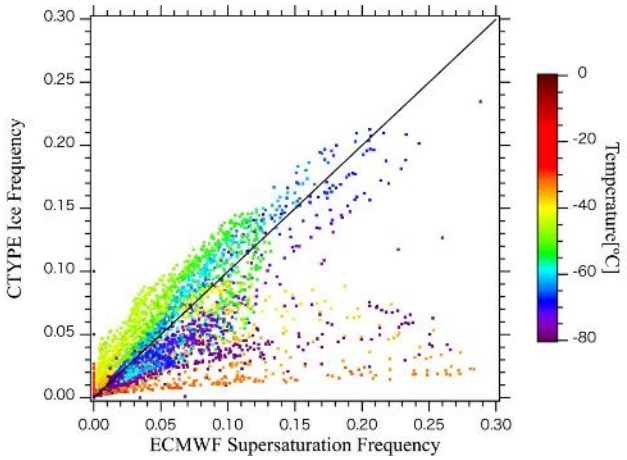

Figure 3.11 Scatter plot of ice cloud occurrence frequency from this study against ECMWF ice supersaturation frequency for temperatures between -80°C and 0°C.

3.5 Summary

The global and seasonal characteristics of cloud phase and ice crystal orientation was analyzed using a CALIPSO dataset from September 2006 to August 2007 and the modified Yoshida et al. [2010] cloud particle type scheme. The temporal (i.e. day/night and season) and spatial (i.e. land/ocean) variabilities of cloud particle habit was investigated and compared against global cloud properties obtained from a different algorithm (NASA/VFM), a different instrument (MODIS) and a numerical model product (ECMWF).

The daytime and nighttime retrievals were compared to evaluate the cloud particle type classification algorithm. Despite the larger noise in daytime, differences in cloud occurrence frequency between day and night were small, except for 3-D ice which was considered to be attributed to the cloud detection due to the diurnal cycle of the clouds and difference in the signal-to-noise ratio between daytime and nighttime, rather than the misclassification of the particle type. These results were encouraging for a fully-resolved classification scheme that avoid averaging of pixels (to increase signal-to-ratio) at the expense of the resolutions as done in the past studies.

The water cloud occurrence between land and ocean was compared and identified a significant difference in the water cloud existence especially at altitudes below 3 km, where the water occurrence frequency over ocean was almost double that of land (i.e. 0.037 over ocean and 0.019 over land), likely due to the large supply of water vapor and weaker upward velocity over ocean. The ice cloud occurrence was compared with the environment humidity condition derived from ECMWF. The global frequencies of ice cloud occurrence from this study and ice supersaturation from ECMWF exerted a similar zonal and seasonal variabilities. Large occurrence frequencies were recognized both in this study and ECMWF around -60°C of the equator, the peak of which shifted from several degrees North (~9°N) in SON to South (~9°S) in DJF and back to North (~7°N) in MAM and JJA, corresponding to the movement of the ITCZ. In general, the cloud particle type estimation was found to be consistent with the results from VFM, MODIS and ECMWF.

Chapter 4 Development of Algorithm for Discriminating Hydrometeor Particle Types with a Synergistic Use of CloudSat and CALIPSO

4.1 Motivation

Taking the advantage of the CALIOP lidar's capability to observe cloud particle habit from space, the global temporal and spatial characteristics of cloud habit (such as their seasonal variabilities, altitude distributions and correlation with ambient conditions) was investigated in Chapter 3, with the comparisons against an alternative lidar algorithm, a different instrument and a numerical model. For a further investigation of the global characteristics of cloud phase, one of the critical physical processes in cloud system to be considered in particular is freezing process from water droplets to ice crystals. The freezing process was historically studied through laboratory experiments, and it is commonly known that the freezing tends to occur more readily when the particle size is larger and the temperature is colder (e.g. Bigg et al., 1953). Although laboratory-based knowledge of the freezing process is fundamental, it is necessary to extend it to the global-scale characterization for the purpose of climate studies. As demonstrated in Chapter 3, CALIOP has the advantage of detecting thin ice clouds; however, its signal is strongly attenuated against water and thick ice clouds, making it difficult to detect clouds underneath. On the contrary, the Cloud Profiling Radar (CPR) onboard the CloudSat, the only alternative active instrument in operation, has the advantage of penetrating into thick clouds but is not sensitive to optically thin clouds. This study is thus motivated towards the synergistic use of these complementary characteristics of CALIOP and CPR to detect a wide range of clouds from thin cirrus to light precipitation. Cloud phase identification using the CPR and CALIOP has been provided as NASA 2B-CLDCLASS-LIDAR product, but, to date, the cloud layer is not vertically resolved [Wang et al., 2013]. In contrast, Ceccaldi et al. [2013] developed an algorithm that vertically resolves cloud phase, warm/cold precipitation within cloud layers with a combined use of CPR and CALIOP exploiting their vertical profiling capability.

Building upon these previous studies, the objective of this chapter is two-fold: (1) to investigate the dependence of the cloud phase and ice crystal shape on particle size and temperature - on a global scale - with a synergistic use of CPR and CALIOP, and (2) to develop an algorithm for classifying phase and types of hydrometeors based on the findings of (1). To address the first objective, I examined how the particle phase and shape vary globally as a continuous function of radar reflectivity and temperature, rather than

introducing thresholds of temperature and radar reflectivity to discriminate particle phase as done by previous studies. Given that radar reflectivity is proportional to the sixth power of particle diameter, the derived relationship of the particle phase/shape with reflectivity would provide an observation-based insight into the particle size dependency in the freezing process. The findings derived from this analysis are then employed to develop CPR stand-alone and CPR-CALIOP synergistic type of discrimination algorithm to offer more complete picture of vertically resolved hydrometeor type classification than has been provided by previous studies. Note that the context of this chapter is published in Kikuchi et al. [2017].

4.2 Hydrometeor Particle Type Dependence on Radar Reflectivity and Temperature

This study explores and combines different sensitivities of CPR and CALIOP to hydrometeor size and type that complement each other to cover a wide spectrum of hydrometeors. The complementary nature of the multi-satellite measurements is exploited to investigate the microphysical characteristics of the hydrometeor types and to develop a more complete algorithms of hydrometeor type classification, as described in the following subsections.

The collocated measurement capability of the two sensors is exploited to relate the hydrometeor type to radar reflectivity and temperature. Figure 4.1 shows the results from such an analysis, where different aspects of the hydrometeor occurrences are investigated as a function of the radar reflectivity, *dbz*, and temperature, *T*, on the global scale. The statistics in Fig. 4.1 was derived from the observations during September and November 2006. The plots are constructed with bin intervals of 0.5 dBZ and 0.5 °C for *dbz* and *T*, respectively. Figures 4.1a and 4.1b show the occurrence frequency of hydrometeors detected by CALIOP and CPR, respectively. The definitions of the occurrence frequencies of hydrometeors are described in Appendix 4.1. As expected, Fig. 4.1a shows that CALIOP detects more cloud at low temperatures than at high temperatures, whereas Fig. 4.1b shows that CPR detects more low-level cloud and precipitation than CALIOP. I first analyze how the particle type relates to *T* and *dbz* for clouds detected by CALIOP and later discuss the relationship for hydrometeors that are missed by CALIOP.

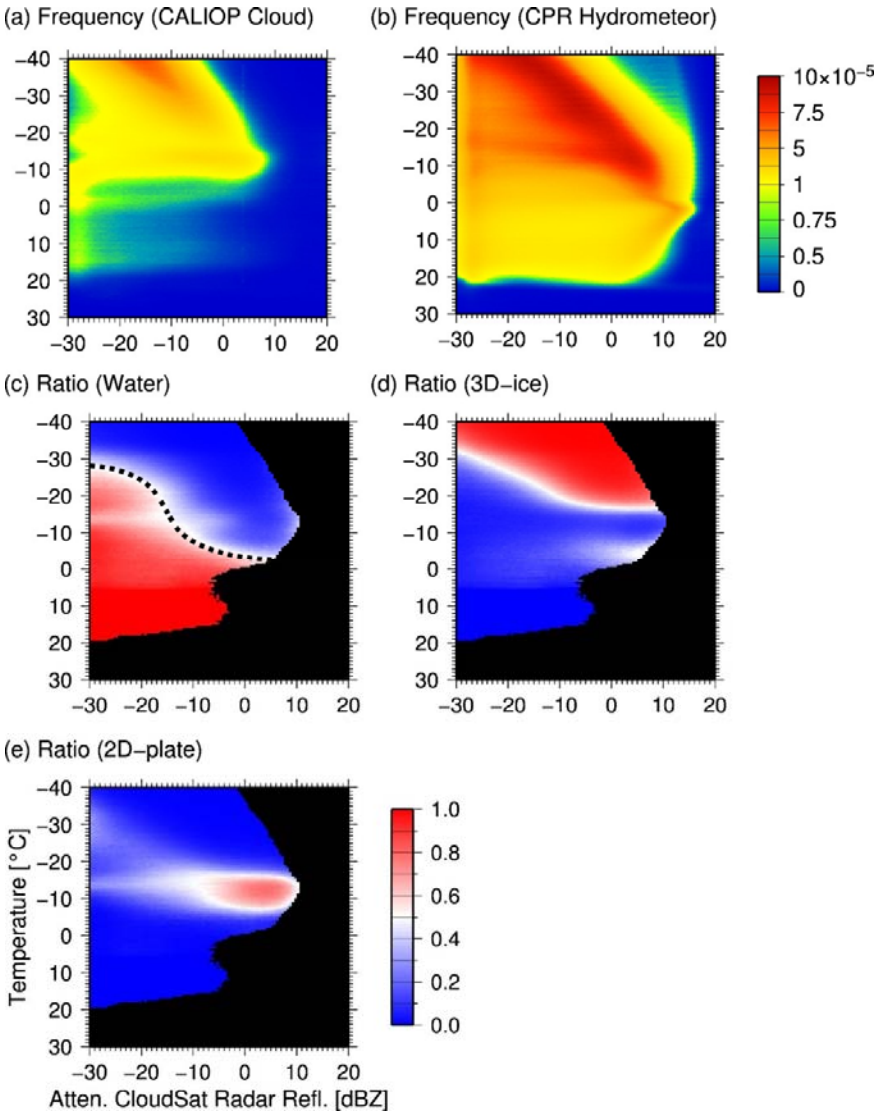

Figure 4.1 CPR reflectivity–temperature distribution of: (a) CALIOP cloud occurrence frequency, (b) CPR hydrometeor occurrence frequency, (c) CALIOP water occurrence ratio, (d) CALIOP 3D-ice occurrence ratio, and (e) CALIOP 2D-plate occurrence ratio. The fractional occurrences are derived for radar reflectivity–temperature bins that exceeds the minimum CALIOP cloud occurrence frequency threshold of 3×10^{-6}, below which corresponds to the black region. An example of the "freezing line", which corresponds to the freezing ratio of 0.5, is drawn in black dotted line in Fig. 4.1c.

Figures 4.1c-4.1e show the fractional occurrences of different hydrometer types (water, 3D-ice, 2D-plate) discriminated by the lidar retrieval as a function of temperature and radar reflectivity. The definitions of the fractional occurrence are also given in Appendix 4.1. The fractional occurrences are derived for radar reflectivity–temperature bins that exceeds the minimum CALIOP cloud occurrence frequency threshold of 3×10^{-6}, below which corresponds to the black region in Figs. 4.1c-4.1e. Note that the CALIOP cloud

occurrence frequency was limited mainly due to the existence of liquid cloud or thick ice cloud above. The global statistics of Figs. 4.1c-4.1e illustrate which hydrometeor type are observed most often when clouds were formed for a given combination of radar reflectivity and temperature. Figure 4.1c shows the temperature dependency of the phase occurrence that is expected from the qualitative behavior of the freezing process: water particles dominate for warmer temperatures and ice particles dominate for colder temperatures. Closer observations within ice particles (Figs. 4.1d and 4.1e) further reveal that horizontally oriented plates (2D-plates) are formed in relatively warm temperature range (between –5 °C and –15 °C) while randomly oriented ice crystals (3D-ice) dominate in colder temperature range. These characteristics are qualitatively consistent with behaviors described in a previous CALIOP analysis study [Yoshida et al. 2010; Zhou et al. 2012] and also with the classical Nakaya diagram [Libbrecht, 2005] derived from the laboratory experiments.

Given that the radar reflectivity is proportional to sixth power of the cloud particle diameter (or proportional to mass concentration and third power of particle diameter), the reflectivity dependency of the statistics in Fig. 4.1 can be interpreted to illustrate how the hydrometeor types tend to relate with the particle size. Note that radar reflectivity is also a function of number/mass concentration. Because radar reflectivity is more sensitive to the particle size, the horizontal axis in Fig. 4.1 would basically reflect the dependency on particle size, although it would also include the dependency on concentration (i.e. even particles with large diameter may give small radar reflectivity when its concentration is very small), which should be kept in mind in the interpretation of Fig. 4.1. Even so, ice particles are in general known to be larger than water particles and it is indeed evident in Fig. 4.1 that ice-phase types are enhanced at large radar reflectivity. Closer investigations of ice-particle shapes in Figs. 4.1d and 4.1e show that ice crystals formed at near –5 °C are dominated by 3D-ice rather than 2D-plate. It is also found in Fig. 4.1d that 3D-ice in this temperature range (near –5 °C) is enhanced only when the particle size (approximated by reflectivity) is considerably large, contrary to the case of temperatures lower than –15 °C where smaller 3D-ice particles are also present. This illustrates one particular aspect of the multiple dependency of the hydrometer type on both temperature and particle size, which is another interesting characteristic identified in Fig. 4.1. In particular, the statistics of Figs. 4.1c-1e hint at how the observed particle size tends to vary with temperature and which ice crystal type tends to dominate at each temperature range. At around –20 °C, for example, small particles with reflectivity of approximately –20dBZ can sustain in liquid state (Fig. 4.1c), but freezing particles start to dominate at a certain threshold of size, approximately –15dBZ (Fig. 4.1c), and form 3D-ice particle (Fig. 4.1d). At around –10 °C, when compared to the -20 °C case, even larger particles are more likely to sustain in liquid phase (Fig. 4.1c) and they tend to become 2D-plate, rather than 3D-ice (Fig. 4.1e).

The co-variability of temperature and particle size for a given particle type is dictated by the "freezing line" that is refer to as the line corresponding to the freezing ratio of 0.5 in Figs. 4.1c-4.1e (an example shown in black dotted line in Fig. 4.1c). Figure 4.1c shows that the slope of the "freezing line" is relatively smooth at temperature below –20 °C and over –10 °C, whereas it is somewhat steeper in between. Interestingly, this temperature range (between –20 °C and –10 °C) coincides with the regions where 2D-plate is enhanced (Fig. 4.1e), and the outer temperature ranges coincide with where 3D-ice is dominant (Fig. 4.1d). The freezing line of 2D-plate also has a "tail" extending to a small radar reflectivity, indicating that 2D-plate can exist with smaller particle size than 3D-ice at the lower temperature just below –20 °C. This suggests that the size of particles is related to the type of the ice particle. The occurrences of 2D-plate and 3D-ice are also found to dominate over different size ranges: the 2D-plate occurrence (ratio > 0.5) is concentrated in the large reflectivity (Fig. 4.1e), while 3D-ice can take wider range of reflectivity including smaller values (Fig. 4.1d). This suggests that 2D-plates are likely to exist as large particles, in agreement with a previous finding that the effective radius for plate-type particles is estimated to be as large as 150 μm by the combined radar and lidar retrievals [Okamoto et al. 2010]. Interestingly, the identification of 2D-plate to exist in large particles is also consistent with the aerodynamic modelling study by Bréon and Dubrulle [2004] who showed that small plate particles have the difficulty in keeping their orientation horizontal. The statistic in Figs. 4.1c-4.1e can be considered as the combined result of the following three processes. One is freezing process of the liquid particle and ice particle being initialized at a given temperature range. Second is the growing process of ice particles within given temperature range. For example, in supercooled clouds, ice particles are often formed as small particles [Lawson et al. 2015; Yang et al. 2016] and grow rapidly. Third is the dynamical process of liquid/solid particles from outer temperature range. Ice particles are often initialized at a colder temperature and grow large while falling. The characteristics found in the statistics of Fig. 4.1 and discussion above suggest how the hydrometeor type (phase and shape) varies with both temperature and particle size on the global scale.

The analysis is extended to a joint analysis of the CloudSat, CALIOP and TRMM data collected over a three-year period from September 2006 to August 2008 and derived the fractional occurrence of precipitation derived from the Precipitation Radar (PR; an active instrument on the TRMM for observing precipitation) with respect to the CALIOP cloud and PR precipitation (figure not shown). The analysis showed that precipitation events (with precipitation rates greater than $0.7 mmh^{-1}$) were dominant where the fractional occurrence of hydrometeor was exceptionally low in Figs. 4.1c–4.1e and the particle type was unable to be determined by CPR and CALIOP alone. With this in mind, the hydrometeor type classification algorithm was developed as is described in the next section.

4.3 CPR and CPR-CALIOP Hydrometeor Particle Type

The analysis described in the previous section revealed the multiple dependency of the hydrometeor type on both radar reflectivity and temperature on the global scale. Based on this finding, an algorithm for classifying hydrometeor types is proposed. At first, given the systematic dependency of particle types on radar reflectivity and temperature, a type classification algorithm using CPR alone is proposed, followed by the proposal of a synergistic algorithm combining CPR and CALIOP.

4.3.1 CPR Stand-alone Hydrometeor Particle Type

The CPR stand-alone algorithm consists of three main steps: (1) initial classification of hydrometeor particle type based on radar reflectivity and temperature, (2) correction for classification of cloud–precipitation, and (3) spatial continuity test.

4.3.1.1 Initial Classification of Hydrometeor Particle Type

The hydrometeor type is initially determined based on the relationship of the dominant hydrometeor type with radar reflectivity and temperature. For this purpose, a type classification diagram was constructed that describes the initial guess of hydrometeor type using the relationship (Fig. 4.2). This was derived from Fig. 4.1 by selecting the hydrometeor type that gave the highest fractional occurrence exceeding the minimum threshold of 3×10^{-6} at a given radar reflectivity–temperature bin. The category of water was further separated according to temperature T into the warm water ($T \geq 0$°C) and the supercooled water ($T < 0$°C). Furthermore, when the fractional occurrence was below the threshold, a precipitation type was assigned based on the fact that dominance of the precipitation coincides with the low occurrence of CPR/CALIOP detection as argued in Section 4.2. The precipitation type was further separated into rain where $T \geq 0$°C and snow where $T < 0$°C. In the next step described in Section 4.3.1.2 and Appendix 4.2, this 0 °C threshold is kept if the precipitation layer did not cross the freezing level (i.e. the precipitation phase does not change throughout the precipitation layer) but the threshold is modified to 2°C [Liu 2008] if the precipitation layer crossed the freezing level, which are often seen in the convective clouds where falling snows typically reach below 0°C level.

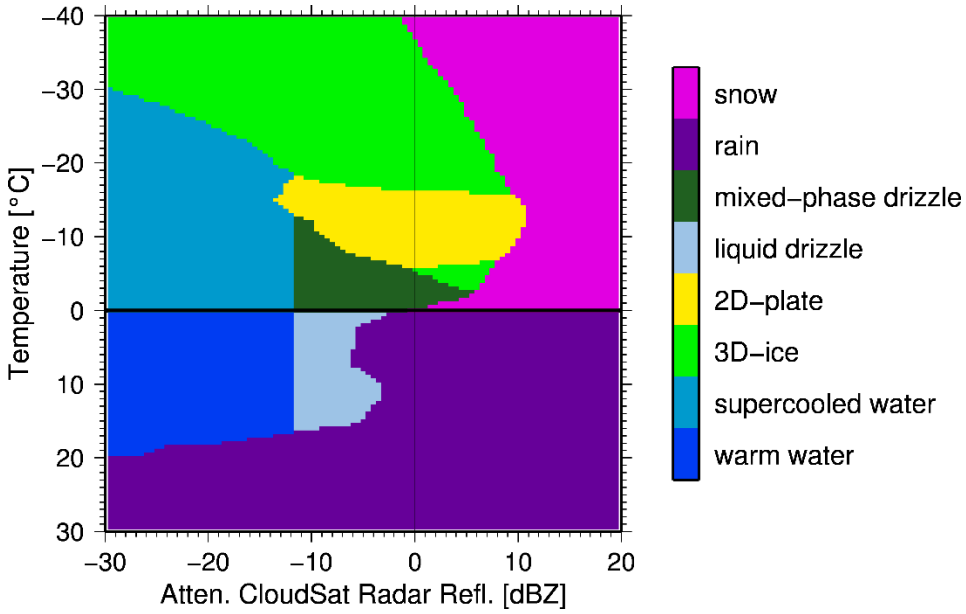

Figure 4.2 Radar reflectivity–temperature diagram for the initial hydrometeor type classification in the radar algorithm. In the precipitation correction, the 0 °C threshold for rain and snow separation was modified to 2 °C if the precipitation layer crossed the freezing level.

The hydrometeor type was further divided into drizzle categories, according to the particle size (approximated by radar reflectivity). The threshold reflectivity that detect the occurrence of drizzle in clouds has been somewhat uncertain in previous studies: the lower limit of the drizzle was taken to be –15 dBZ [Matrosov et al., 2004; Stephens and Haynes, 2007] and –18 dBZ [Leon et al., 2008]. The present study set the limit to -11.75 dBZ, considering the existence of supercooled water at -18.25 °C and -11.25 dBZ (Fig. 4.2). The drizzle category was further separated according to temperature into subcategories of liquid drizzle for $T \geq 0$°C and mixed-phase drizzle for $T < 0$°C. The latter assignment was introduced because the relatively large radar reflectivity (over -11.75 dBZ) for the temperature below 0°C implies the presence of ice particles (i.e. not water) while the collocated lidar observation indicates the existence of water (Fig. 4.1c). Above $T \geq 20$°C, the rain type was assigned even at low radar reflectivity since radar signal is often attenuated by the precipitating layer above. At this stage, there are some circumstances where cloud water particles, instead of rain, are present. In this case it is difficult to discriminate the hydrometeor type based on radar reflectivity alone and information on path integrated attenuation (PIA) is used in the procedure followed to correct cloud-precipitation partitioning (Section 4.3.1.2 and Appendix 4.2). Overall, water particles are assigned to low radar reflectivity (i.e. small-sized particles), ice and drizzle particles to moderate reflectivity, and precipitating particles to high reflectivity.

The present study extends the previous study by Ceccaldi et al. [2013], who developed the CloudSat (and CALIOP) phase discrimination algorithm using independent thresholds based on radar reflectivity and temperature, respectively. Here, the multiple dependency of hydrometeor type on both radar reflectivity and temperature was employed, which was built based on collocated CALIOP measurements, making the maximum use of global measurement information, and proposes the hydrometeor type classification method based on global statistics of the hydrometeor occurrence as a function of particle size and temperature.

4.3.1.2 Correction for Cloud and Precipitation Partitioning

The initial guess of the hydrometeor type described above is then corrected in the context of cloud-precipitation partitioning for each CPR profile using the precipitation detection method by Haynes et al. [2009]. The details of the correction method are described in Appendix 4.2. To summarize, the attenuation-corrected radar reflectivity factor near the surface is derived from PIA to identify “snow definite”, “rain definite” and “no precipitation” profiles based on Haynes et al. [2009]. Then, any profile that is inconsistent with the initially estimated type is corrected. For example, for “rain definite” or “snow definite” profiles, the initially classified cloud pixels in the lowest layer is corrected to precipitation. The readers should refer to Appendix 4.2 for more details of the correction methodology.

4.3.1.3 Spatial Continuity Test and Final Classification

In the last step of the radar-only algorithm, the spatial continuity test similar to what is applied in the lidar scheme [Yoshida et al., 2010] is conducted. This test investigates if the pixel of target is registered to an irregular type by checking the consistency with the dominant type in the surrounding pixels. In the test, a total of 15 bins (3 vertical × 5 horizontal) around the target bin is considered, and chose one hydrometeor type, from water, drizzle, 3D-ice, 2D-plate, and precipitation, that is most frequently assigned within the 15 bins. Hence the input of the test would be one of water, drizzle, 3D-ice, 2D-plate, and precipitation, and the result would also be one of those types, with the pixel of target corrected if necessary. The temperature information is then used to discriminate the phase of water, drizzle, and precipitation.

After passing these three procedures, the hydrometeor type is classified into one of these eight categories: warm water, supercooled water, 3D-ice, 2D-plate, liquid drizzle, mixed-phase drizzle, rain, and snow. Figure 4.3 summarizes the overall flow of the radar-only algorithm.

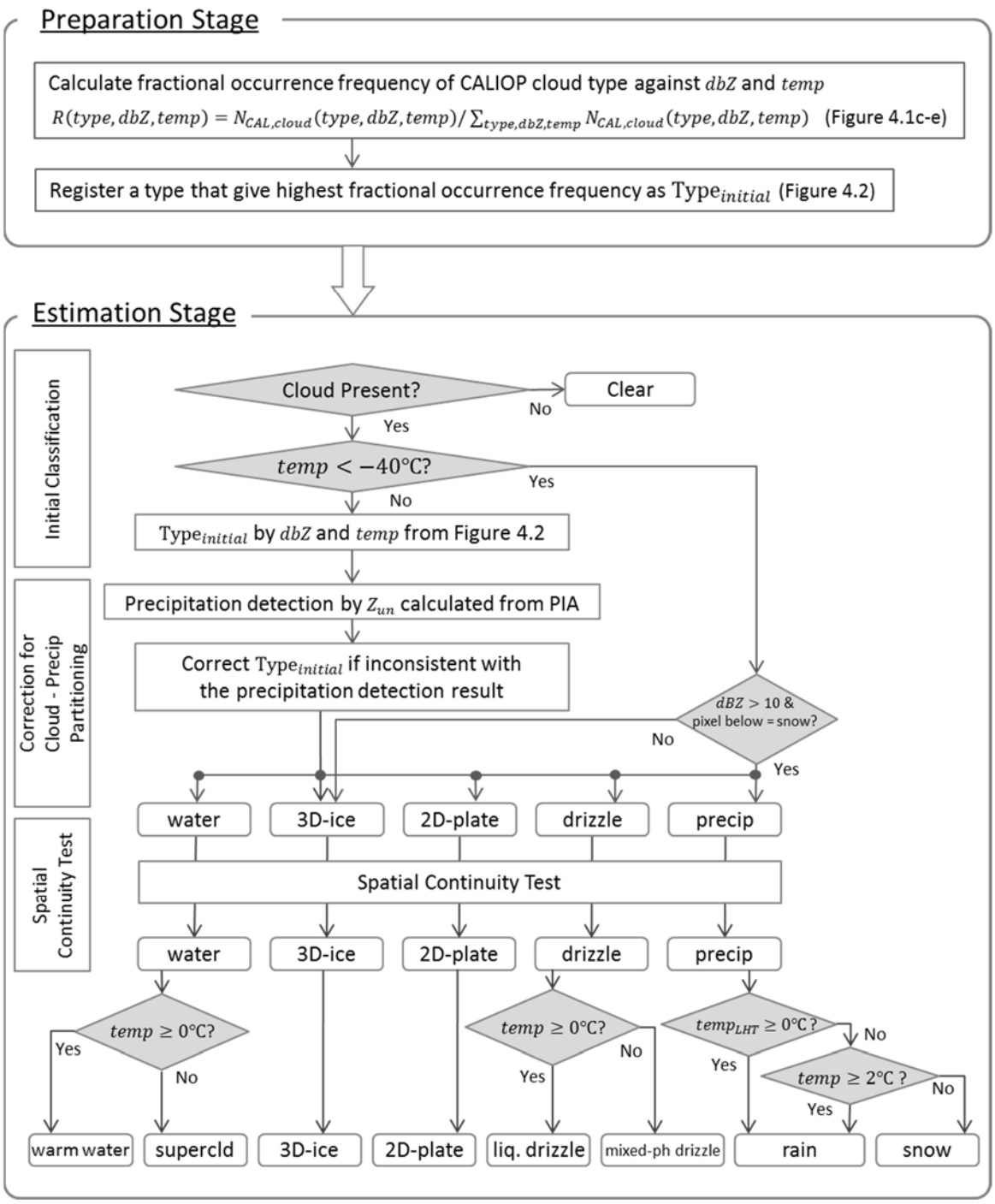

Figure 4.3 Overall flow of radar algorithm. dbz is radar reflectivity, $temp$ is temperature, and Z_{un} is attenuation-corrected radar reflectivity at near surface. $R(type, dbz, temp)$ is the fractional occurrence frequency of CALIOP for a type, $type$, at a given dbz and $temp$. $Type_{initial}$ is the initial type determined form Fig. 4.2. $N_{CAL,cloud}(type, dbz, temp)$ is the total number of CALIOP observations for $type$ at a given dbz and $temp$. $temp_{LHT}$ is the precipitation height top temperature of the lowest hydrometeor.

4.3.2 CPR-CALIOP Synergy Hydrometeor Particle Type

4.3.2.1 Algorithm Description

The radar-only algorithm described in Section 4.3.1 is further combined with the independent information of the lidar measurement described in Section 3.2 to propose a radar-lidar synergy classification algorithm. In other words, hydrometeor particle types were independently derived by the lidar algorithm (using depolarization ratio δ and a parameter χ as a proxy of lidar attenuation) and the radar algorithm (using radar reflectivity and temperature). In the synergy algorithm, the classifications derived from the radar-only algorithm was compared with the lidar-based type classifications and assign the types according to the rule defined in Table 4.1, which results from the discussion below.

Table 4.1 Combination of CloudSat and CALIPSO* hydrometeor particle type classifications used to derive the synergy classifications.

		CALIOP				
		water	3D	2D	3D+2D	missing/clear/ unknown
CloudSat	water	water	3D	2D	3D+2D	water
	liquid drizzle	water+ liquid driz.	3D	2D	3D+2D	liquid driz.
	rain	water+rain	3D	2D	3D+2D	rain
	3D	mixed-phase cloud	3D	2D	3D+2D	3D
	2D	mixed-phase cloud	3D	2D	3D+2D	2D
	mixed-phase drizzle	mixed-phase cloud	3D	2D	3D+2D	solid driz.
	snow	mixed-phase cloud	3D	2D	3D+2D	snow
	missing/clear	water	3D	2D	3D+2D	missing/clear/unknown

At first, if only one type is available from radar and lidar, then the type is assigned as the synergy type. This rule is introduced to make the most of hydrometeor detection capability given either by radar or lidar. Combining radar and lidar information in this way, the lidar measurement limitation because of attenuation is complemented by radar detection of hydrometeors and the radar limitation to miss cirrus is complemented by lidar's high sensitivity to thin clouds. Note that in the case where CPR identified a type but CALIOP classified "clear", CALIOP type should be assigned as "attenuated" since the situation is likely to arise from the attenuation of the lidar signal rather than no presence of hydrometeors. Although this itself is an issue of the lidar-only cloud mask that should be addressed in the future (outside the scope of this study),

the approach here to employ the radar information as well avoids missing the hydrometeor detection by lidar.

Secondly, the synergy type is defined with a particular care when the CALIOP and CPR offer different hydrometeor types. In some cases, I considered the type to be a "mixture" of those from CALIOP and CPR. For instance, when the CALIOP type is water and the CPR type give a different one, the mixture of water and liquid drizzle/rain or mixed-phase cloud was assigned, depending on the CPR type. Note that the combination of water and snow is rare (less than 0.01% of total cloud particle type), so they were merged into the mixed-phase cloud type. Another example was the situation where CALIOP detects ice and CPR detects water. In this particular case, the CALIOP type was considered to be correct since it observes not only the backscattering intensity but also the depolarization.

Table 4.2 Definition of CloudSat-CALIOP synergy hydrometeor particle types.

Type	**Definition**	**Source**
warm water	liquid water cloud particles with $T > 0$°C	CALIOP and/or CPR
supercooled water	liquid water cloud particles $T \leq 0$°C	CALIOP and/or CPR
3D-ice	randomly oriented ice crystals	CALIOP and/or CPR
2D-plate	horizontally oriented ice plates	CALIOP and/or CPR
3D-ice+2D-plate	mixture of 3D-ice and 2D-plate	CALIOP and/or CPR
liquid drizzle	drizzle in liquid phase	only CPR
mixed-phase drizzle	drizzle consisting both liquid and ice phase particles	only CPR
rain	light liquid precipitation	only CPR
snow	solid precipitation	only CPR
mixed-phase cloud	mixture of liquid cloud (by CALIOP) and ice cloud particles (by CPR)	CALIOP and CPR
water+liquid drizzle	mixture of liquid cloud (by CALIOP) and liquid drizzling particles (by CPR)	CALIOP and CPR
water+rain	mixture of liquid cloud (by CALIOP) and rain (by CPR)	CALIOP and CPR
unknown	undetermined type	CALIOP

It should also be noted that the combination of CALIOP 3D-ice/2D-plate and CPR drizzle/precipitation is rare. Therefore, they were defined as the CALIOP type. Under the circumstances where CALIOP offers

water and CPR offers mixed-phase drizzle, the case was included into the “mixed-phase cloud” (without drizzle) rather than “mixed-phase drizzle” to identify that “mixed-phase cloud” is derived from the combination of CPR and CALIOP whereas “mixed-phase drizzle” was derived from CPR alone. Note that the fractional occurrence of the combination of CALIOP water and CPR drizzle/precipitation is exceptionally low (less than 0.01% of the total).

As a result of this rule for the radar–lidar synergy scheme, the hydrometeor type is classified into the following thirteen categories: warm water, supercooled water, 3D-ice, 2D-plate, 3D-ice+2D-plate, liquid drizzle, mixed-phase drizzle, rain, snow, mixed-phase cloud, water+liquid drizzle, water+rain and unknown.

4.3.2.2 Error Analysis

In application of the hydrometeor type classification algorithm described above, the uncertainty induced by the errors from the input parameters, including measurement errors, were quantified by an error analysis. Note that the error analysis in this section does not cover the errors associated with algorithm logic or the adequacy of type selections. For the input parameters, I selected four main parameters that contribute to the algorithm: attenuated radar reflectivity, backscattering coefficient, depolarization ratio, and temperature. The errors were considered to be within ± 1 dBZ for the attenuated radar reflectivity [Protat et al., 2011], ± 1.09 K for the ECMWF temperature [Eyre et al. 1993], ± 2 % for the total backscattering coefficient and ± 10 % for the depolarization ratio [Hunt et al., 2009; Okamoto et al., 2010]. Although the error associated with the backscattering coefficient would be zero because it was presented as the ratio of two consecutive layers in the lidar algorithm which would cancel each other out, I added the random error after the calculation of the ratio. These parameters are perturbed separately in both the positive and negative directions within the assumed uncertainty range to investigate how the uncertainty of each parameter is propagated to the error of the resultant hydrometeor type identified. The analysis was conducted for one day of observation on 13 September 2006. When the results without perturbation are used as a reference for the “true” observation, the type classification error ε_i arising from each parameter i can be computed as the root mean square of the fractional occurrence of misclassification:

$$\varepsilon_i = \frac{N_{i,error}}{N_{obs}} \times 100 \quad [\%] \qquad (4.1)$$

where $N_{i,error}$ is the number of pixels that mismatched with the true observation and N_{obs} is the total number of hydrometeor observations. The type classification error for the radar reflectivity uncertainty is estimated to be 2.5% and 2.5% for +1 dbZ and –1 dBZ biases, respectively. Similarly, the respective errors were 4.4% and 4.3% for the temperature error of ±1.09 K, and 0.8% and 0.9% for the depolarization ratio error of ±10%, 0.09% and 0.09% for the backscattering coefficient error of ±2%, respectively. Assuming that the

input parameters are independent of each other and their covariance is negligible, the total error arising from the five parameters, derived by the root mean square of the fractional uncertainties, is estimated to be 5.8%. To the total error of 5.8%, 3D-ice contributed the most at 24.7%, followed by 20.1% for 2D-plate, 15.8% for snow and 15.5% for supercooled water, 8.3% for rain, 6.1% for warm water and mixed-phase drizzle. The contribution of the rest of the respective errors were less than 1 %. Note that the effect of CALIOP's pointing direction to the lidar and synergy algorithm is discussed in Appendix 4.3.

4.3.2.3 Algorithm Uncertainty

In the synergy algorithm, the lidar classification is considered to be more robust than the radar algorithm since particle types are determined using two independent observables: i.e. backscatter and depolarization. The radar classification is considered to persist larger uncertainty since only one measurement information of radar reflectivity is available. In a case where both the radar and lidar observed a cloud, the radar classification will be modified, if necessary, to the most reasonable type using the information offered from the lidar (Section 4.3.2.1). Hence the largest uncertainty in the synergy algorithm is considered to be attributed to the classifications that were only detected by the radar. To recall, the classification diagram in the radar scheme (Fig. 4.2) is derived from the synergetic analysis of the radar and lidar in Fig. 4.1. Where the fraction of the particle type frequency is high or low (i.e., the red or blue region in Fig. 4.1), the radar and lidar classifications give consistent type in most of the cloud-observed cases. Thus, the ambiguity in the radar algorithm remains to where (1) the fraction is near 0.5 (i.e., the white region in Fig. 4.1) in which different lidar types are observed almost in equal frequency, and (2) the transition region from cloud to precipitation types (although this is partly checked in the cloud-precipitation correction followed: c.f. Appendix 4.2). Given the difference in the terminal velocity among the types, one of the future work is to evaluate this diagram by the ground-based Doppler radar observation, which provides the vertical Doppler measurement as another independent observable, in addition to the radar reflectivity.

4.4 Case Study and Validation

4.4.1 Case Study

Before the radar–lidar synergy particle type classification algorithm is applied globally, case studies are conducted to evaluate the algorithm. Two measurement cases are analyzed for this purpose: (1) an Arctic case when the temperature was below the freezing level throughout the layer and thus the observed clouds were expected to be limited to supercooled or iced types, and (2) a near tropic case where the vertical temperature gradient was large and various particle types were expected to exist.

Figure 4.4 shows the cross sections of several parameters and hydrometeor type classifications for the first case observed over Arctic at 1350 UTC on 16 November 2006. The lidar backscattering coefficient (Fig. 4.4a) shows a multi-layer cloud structure stretching over several hundreds of kilometers in along-track direction, consisting of low-level clouds around 1 km in altitude and mid- and high-level clouds around 4 km to 13 km in altitude. The majority of mid- and high-level clouds (> 6 km) is classified as 3D-ice even by the radar-only algorithm (Fig. 4.4e), although there are some undetected thin clouds. The lidar attenuation due to mid- and low-level clouds (below 6 km in altitude between 63°–66° latitude or at 1-km altitude) is large and the depolarization is relatively high (~20%, although lower than the ice particles in the upper layer) as shown in Fig. 4.4b, which corresponds to supercooled water. The CPR type (Fig. 4.4e) also classifies the clouds as supercooled water due to their low radar reflectivity. It is noteworthy to mention that between latitudes 63°–66° and approximately 5 km in altitude, the lidar could observe only the cloud top of the supercooled water layer, whereas the radar could observe the consecutive thicker supercooled water layer underneath. The 2D-plate type is assigned based on a low lidar attenuation and depolarization ratio (approximately 3%) at 66° latitude at 5 km altitude. The 2D-plate type is also assigned by the radar-only scheme because the condition of radar reflectivity and temperature matches what corresponds to 2D-plate. Therefore, independent classifications by the radar and lidar types are overall in good agreement in this particular case. In the synergy type (Fig. 4.4f), the radar and lidar classification results complement each other, demonstrating the usefulness of the radar-lidar combined product. For example, the synergy type is assigned as 3D-ice for thin clouds detected by only lidar and as a supercooled layer that ranged vertically for a few kilometers observed only by radar. It is worth mentioning that in the case in Fig. 4.4, radar reflectivity was notably low (approximately -15 dBZ) and the radar algorithm assigned the type of "supercooled water" throughout the layer. Another typical case in polar region is where liquid water exists at the cloud top with ice phase precipitation underneath [Shupe 2007; Morrison et al. 2012] which is also shown in Fig. A4.2 in Appendix 4.4 with CALIOP detecting water particle and CPR detecting solid precipitation. Because supercooled water is separated from mixed-phase drizzle at the threshold of -11.75 dBZ, there may be a potential overestimation of the supercooled layer in the polar regions, and therefore, the validation with ground-based W-band radar and lidar (e.g. ARM, ArCS data) is considered necessary.

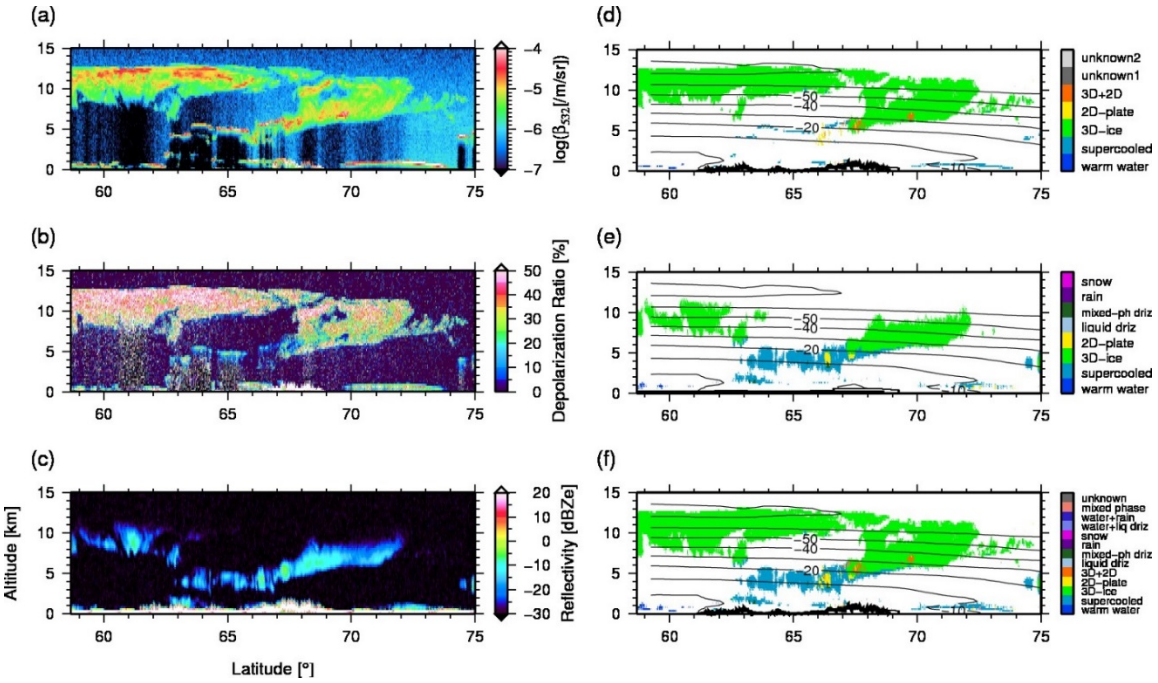

Figure 4.4 Example case of hydrometeor particle type classification: (a) CALIOP backscattering coefficient, (b) CALIOP depolarization ratio, (c) CPR attenuated radar reflectivity, (d) CALIOP hydrometeor particle type, (e) CPR hydrometeor particle type, and (f) CALIOP–CPR synergy hydrometeor particle type. The observation was conducted over Arctic at 1350 UTC on 16 November 2006.

Figure 4.5 shows the near tropics case observed on 1020 UTC 2 November 2006 between 20° and 28° latitude over North East Pacific. The hydrometeors are inhomogeneous in the along-track direction and the temperature vertically ranged from –60 °C to 20 °C, with the maximum temperature difference as large as 80 °C. Between 20°–21° latitude and at an altitude of around 9 km, the lidar signal is strongly attenuated (Fig. 4.5a) due to the presence of supercooled water that produces high depolarization due to multiple scattering. This indicates that the liquid phase particle is present at such a low temperature of –30 °C. With a low radar reflectivity, the radar classification also indicates supercooled water at the same altitude although the cloud-detected area is smaller than that of lidar. Between 23° and 25.5° latitude and temperatures from –10 °C to –20 °C, the lidar discrimination (Fig. 4.5d) shows a 2D-plate layer with a low depolarization ratio (Fig. 4.5b) horizontally stretching for more than 100 km. In this region, very high values of backscattering larger than 10^{-4} /m/sr were observed (Fig. 4.5a) due to the specular scattering of the laser. Between the 3D-ice and 2D-plate layers, mixture of 3D-ice and 2D-plate types are also identified (Fig. 4.5d). In the radar classification (Fig. 4.5e), 2D-plate is also indicated although its presence strongly depends on temperature. In the synergy type (Fig. 4.5f), the lidar classification result is preferred for defining an ice crystal type (either 3D-ice, 2D-plate or mixture of 3D and 2D) since it observes not only

the backscattering but also the depolarization, giving a more realistic type. The radar also detected convective precipitation (at 24.5°–25.5° latitude) and shallow precipitation (intermittently between 20°–24° latitude), which are not observed by the lidar. Particularly with respect to convective precipitation, the radar observes a melting layer with high radar reflectivity at an altitude of around 3.5 km and the synergy classification (Fig. 4.5f) also modified the type from snow to rain as the temperature reached 0 °C at the corresponding height. Overall, the synergy scheme generated types ranging from cirrus to thick clouds and precipitation.

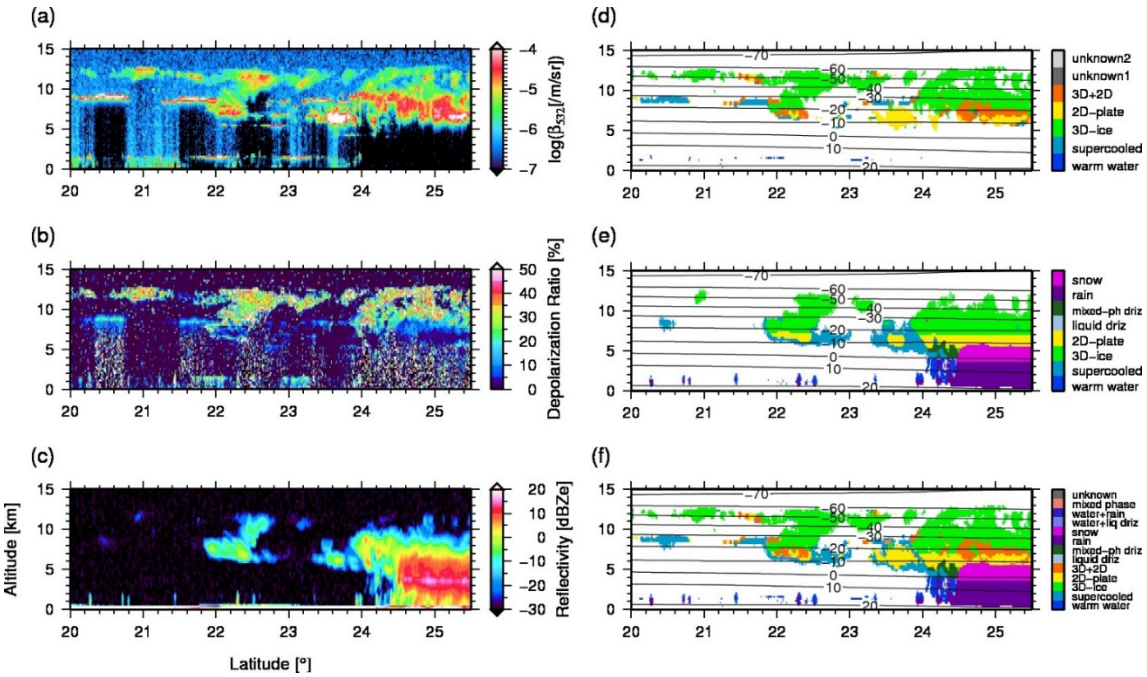

Figure 4.5 Example case of hydrometeor particle type classification: (a) CALIOP backscattering coefficient, (b) CALIOP depolarization ratio, (c) CPR attenuated radar reflectivity, (d) CALIOP hydrometeor particle type, (e) CPR hydrometeor particle type, and (f) CALIOP–CPR synergy hydrometeor particle type. The observation was conducted over North East Pacific at 1020 UTC on 2 November 2006.

4.4.2 Validation using Aircraft In-situ Observation

The algorithm is validated against two in-situ aircraft observations collocated with CloudSat/CALIPSO measurements. The first is from the “Cirrus Cloud Experiment” (CIRCLE-2) [Eichler et al., 2009] and the second is from the “Arctic Study of Tropospheric Aerosol Clouds and Radiation” campaign (ASTAR) [Engvall et al., 2008]. The first case is relatively simple and I used this case to validate the classification results under a few uncertain conditions. The second case is more complex scene where liquid and solid

particles co-exist. The lidar-only type classification has already been compared with the aircraft observations in Cesana et al. [2016], who validated the so-called Kyushu University product, which corresponds to the lidar classification in this study. Therefore, this study focuses on the validation of the final radar–lidar synergy classification result. The aircraft-based cloud detection and cloud phase classification were those determined using extinction coefficient and asymmetry factor observations, respectively, obtained from a polar nephelometer. For further details, readers should refer to Cesana et al. [2016]. The present study used aircraft data observed within 5 km and 10 minutes of the satellite observations.

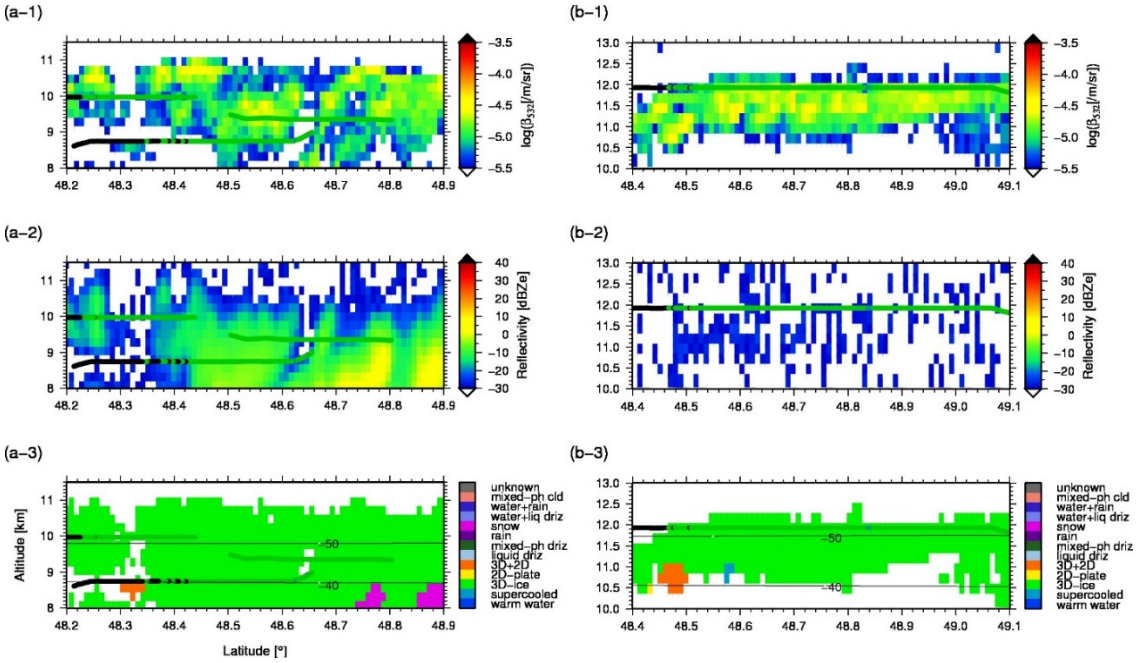

Figure 4.6 Validation of hydrometeor particle type classification with aircraft observation: left column (a) and right column (b) were observed on 26 May 2007 and 16 May 2007, respectively. Both observations were conducted over the midlatitudes. (1) CALIOP backscattering coefficient, (2) CPR attenuated radar reflectivity, and (3) CALIOP–CPR synergy hydrometeor particle type. The lines indicate aircraft track, with green indicating ice cloud, blue is water, and black is clear sky.

Figure 4.6 shows the synergy type classifications, together with the CPR and CALIOP observations on 26 May 2007 and 16 May 2007 in the left column and right column, respectively. Figures 4.6 (a-1) and (b-1) are similar to the figures in Cesana et al. [2016] (their Figs. 2c and 2a). The line in the figures indicates the aircraft track and the green and blue colors show the presence of ice and water clouds, respectively, as determined according to the polar nephelometer classification. Note that the color scheme is same as that

used in the satellite type classification. The black color in the aircraft classification indicates clear sky. The majority of clouds observed by the aircraft are at the altitude higher than 8 km where the ice phase dominates, which makes the comparison relatively simple. On the 26 May case (left column), the lidar observes only the upper part of the cloud while the radar detects the geometrically and optically thick bottom part of cloud layer. Although the case is limited to cold ambient, the 3D-ice classification in lidar algorithm is not so obvious as it does not use temperature between -37.0°C and -39.3°C at altitudes below 9 km (i.e. it only uses depolarization ratio and the parameter χ, which is a proxy of lidar attenuation). The 3D-ice type identified by the synergy classification scheme is consistent with what is obtained from aircraft in the detection of ice clouds. Between 48.34°N and 48.46°N latitude at altitudes below 9 km, the lidar signal is fully attenuated and that area was only observed by the radar. The synergy classification shows 3D-ice, which is in good agreement with the aircraft observations. In the 16 May case (right column), as the cloud layer are too thin to be detected by the radar, the 3D-ice type identified by the lidar classification is readily adopted in the synergy scheme.

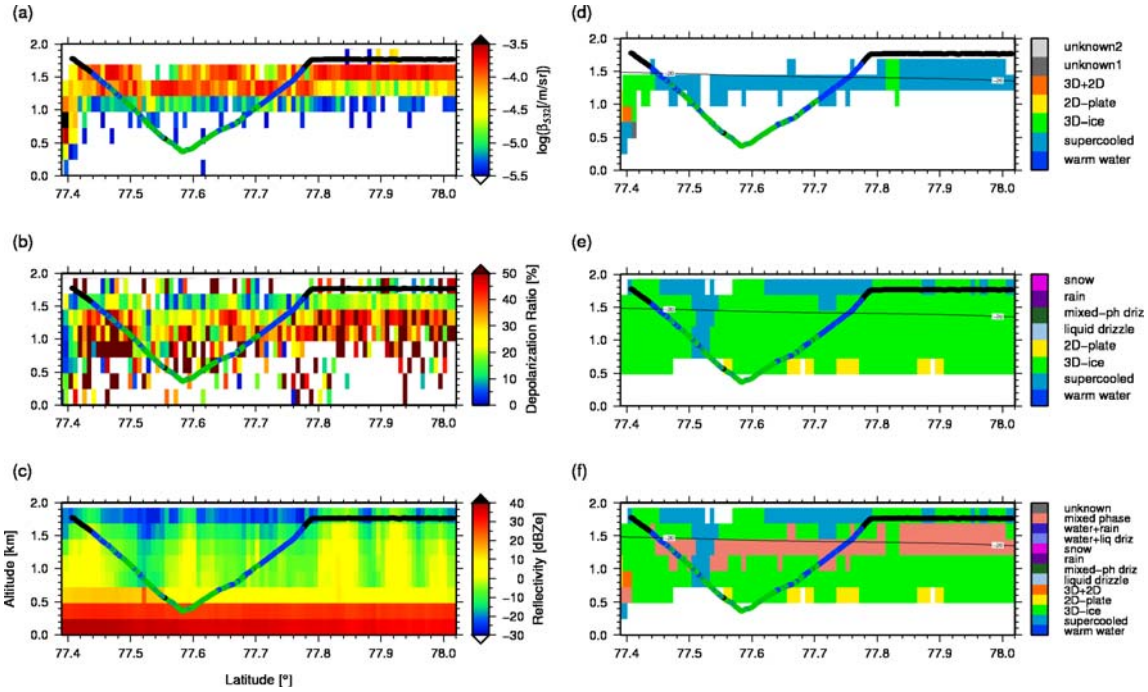

Figure 4.7 Validation of hydrometeor particle type classification with aircraft observation on 7 April 2007 over the Arctic. (a) CALIOP backscattering coefficient, (b) CALIOP depolarization ratio, (c) CPR attenuated radar reflectivity, (d) CALIOP cloud particle type, (e) CPR hydrometeor particle type, and (f) CALIOP–CPR synergy hydrometeor particle type. The lines indicate aircraft track, with green indicating ice cloud, blue is water, and black is clear sky.

To quantify the extent to which the satellite synergy classification agrees with the in-situ aircraft classification, I defined a consistency ratio as the total number of pixels that meet the following conditions divided by the total number of the satellite pixels collocated with the aircraft: (1) the synergy classification matched with an aircraft phase within the satellite bin of 1.1km horizontal and 240m vertical (except for the mixed-phase type); (2) if the synergy classification is mixed-phase type, the aircraft observes either mixed-phase or the combination of water and ice clouds within the satellite bin. The analysis was restricted to data for which both the aircraft and satellite were able to conduct phase classification. In both cases of Fig. 4.6 the consistency ratio was 100%, meaning the perfect agreement between the satellite and aircraft type classifications.

Another validation was performed for the case observed in the Arctic on 7 April 2007. Figures 4.7a, 4.7b and 4.7d are similar to the figures in Cesana et al. [2016] (their Figs. 3a, 3c, 3i). At altitudes below 500 m, the CPR data is affected by the surface clutter and thus the CPR type (and also the synergy type) cannot be diagnosed. Above 500m, however, the cloud phase for low-level clouds can be compared and verified even when the lidar could not observe them, by using the synergy classification based on the CPR only classification. According to the aircraft data, the presence of liquid clouds is mainly found near cloud top and ice phase (with some water mixed in) in underneath layers. The synergy classification also indicates that ice phase dominates at altitudes below 1 km between 77.54°N–77.64°N latitude, overall consistent with aircraft observations. Even at 77.54°N latitude or less, the aircraft probe alternatively detects water and ice layers so do the synergy type observations (water and ice or mixed-phase type). The consistency ratio in this case is 73.0%. The inconsistency of about 27% comes from the misclassifications between 77.64°N–77.80°N latitude. Along the aircraft track, the synergy classification type changes at 77.7°N from 3D-ice to mixed-phase cloud, in response to the inclusion of the lidar observations. At latitudes less than 77.7°N, the aircraft observes consecutive water and ice cloud in the satellite pixels. However, the synergy classification determines 3D-ice based on high radar reflectivity (approximately –10 dBZ; c.f. Fig. 7c), which is too high to be produced by water clouds. At latitudes above 77.7°N where the synergy classification determines mixed-phase cloud (in pink), the aircraft observes consecutive water clouds, which resulted in inconsistency. The synergy mixed-phase cloud is determined by the lidar water cloud (Fig. 4.7d) and radar 3D-ice (Fig. 4.7e). Again, the radar-only scheme assigns 3D-ice due to its high radar reflectivity. There are two possible causes for the inconsistency between the aircraft and satellite observations: (1) there was a phase transition or advection of clouds with different phase during the time and space collocation windows (5 km and 5 minutes between the satellite and the aircraft); (2) the aircraft locally observes only a portion of the satellite scattering volume and the difference in the spatial representativeness of the satellite and aircraft caused the inconsistency. Although the misclassification by

the synergy type is concerned in the area (77.64°N–77.80°N latitude), the radar reflectivity factor is as large as –10 dBZ and that ice cloud was considered to actually did exist. In other words, water was dominated within in-situ measurements, whereas water and ice were dominated within CALIOP and CPR measurements, respectively, which resulted the “mixed-phase cloud” in the synergy type.

The satellite-aircraft comparison performed in this study demonstrates that the synergy type and aircraft in-situ measurements agree well for the case in mid-latitude high-level ice clouds and also gives consistent results for the case in the Arctic region where water and ice clouds coexist. A direct comparison of aircraft and satellite measurements, however, involves some issues. In particular, the collocation in time and space makes it difficult to observe the same spatial and temporal variabilities of clouds, giving differences in the representativeness of the observations, and the possibility of phase transition under the circumstances where water and ice coexist. In the future, it is required to extend the comparison into more various cases and to validate the satellite-based classification schemes with different types of hydrometeors, with attention paid to the validation conditions (including cloud spatiotemporal homogeneity and satellite-aircraft collocation).

4.5 Global Characteristics of Hydrometeor Particle Types

After validating the classification algorithm, the algorithm was applied to the global analysis of hydrometeor particle types to study their behaviors. The zonal and global mean frequency of occurrence were investigated for each hydrometeor type. For the zonal mean occurrence frequency, I first discuss the key features found in the lidar- and radar-only classification (Figs. 4.8 and 4.9) and then show how they are merged in the synergy classification (Fig. 4.10). The definitions used to derive these statistics are given in Appendix 4.1.

4.5.1 Zonal Mean Occurrence Frequency

Here, the consistency of hydrometeor classification obtained by the CPR-only scheme with the CALIOP-only scheme in Chapter 3 was investigated. Despite the CPR classification being built based on CALIOP information, this does not guarantee the agreement of their global distributions. Figures 4.8 and 4.9 investigate these points by showing the zonal mean cross section of the occurrence frequency of each particle type for CALIOP and CPR, respectively. The statistics were derived between September and November 2006. Latitude and altitude were sampled every 2° and 240m, respectively. Note that the water is the sum of warm water and supercooled water. The main findings derived from this analysis are as follows:

(a) The CPR types of water, 3D-ice and 2D-plate (Figs. 4.9-2 – 4.9-4) generally show distributions of occurrence similar to the corresponding CALIOP types (Figs. 4.8-2 – 4.8-4). This suggests that the occurrences of the CPR types, derived from combined radar reflectivity and temperature, were statistically consistent with those of the CALIOP types, derived from the independent observations of depolarization and lidar attenuation. Figure 4.8 and 4.9 confirm the consistency of the two schemes in terms of their existence region. However, the occurrence frequencies of the CPR types are overall higher than those of CALIOP because the CPR is capable of observing hydrometeors where the CALIOP signal is attenuated.

(b) The hydrometeor types detected by CPR alone, namely liquid drizzle, mixed-phase drizzle, rain and snow (Figs. 4.9-5 – 4.9-8), are those that were difficult to obtain from the lidar scheme in Chapter 3 due to its total attenuation by the water clouds or thick ice clouds above. The drizzle or precipitation types are assigned to the bin where the radar reflectivity is relatively high ($> -11.75 dBZ$) associated with large-sized particles. The rain type is found to occur frequently in the tropics (Fig. 4.9-7), centered at approximately 10° N, where deep convection is ubiquitous. The rain type occurrence is also found to be enhanced at mid-latitudes (30°–60°) in both hemispheres, which is associated with the storm tracks. It is also shown that some of CPR types (e.g., 2D-plate and mixed-phase drizzle) share the common arched-shape distributions primarily determined by latitudinal temperature variations. This emphasizes that the different types were identified according to different radar reflectivities even in isothermal conditions.

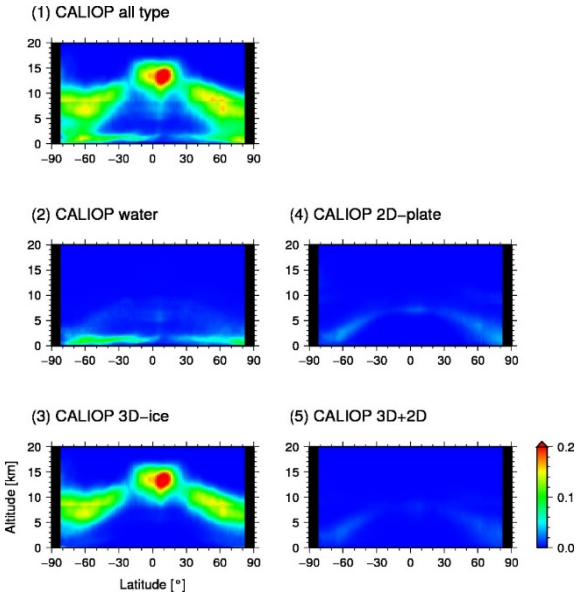

Figure 4.8 Latitude–altitude cross-section of hydrometeor particle type for CALIOP cloud type retrieved from the algorithm in Chapter 3: (1) all types, (2) water (warm water + supercooled water), (3) 3D-ice, (4) 2D-plate, and (5) 3D-ice + 2D-plate.

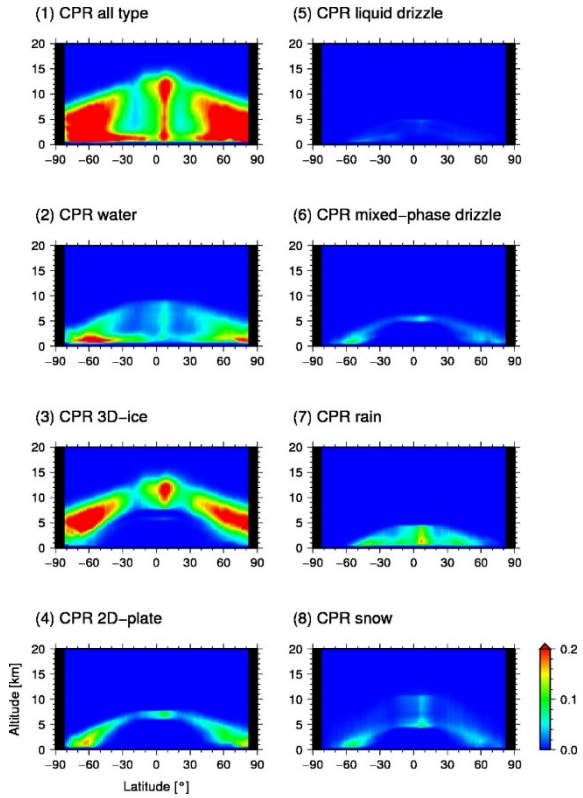

Figure 4.9 Latitude–altitude cross-section of hydrometeor particle type for CPR hydrometeor type retrieved from the algorithm developed in this chapter: (1) all types, (2) water (warm water + supercooled water), (3) 3D-ice, (4) 2D-plate, (5) liquid drizzle, (6) mixed-phase drizzle, (7) rain, and (8) snow.

Similarly, the occurrence frequencies of hydrometeor types obtained from the CPR–CALIOP synergy algorithm are shown in Fig. 4.10 in the form of the zonal mean cross section. The latitude and altitude samplings and the observation period analyzed are the same as those shown in Fig. 4.8. The main findings are summarized as follows;

(a) The synergy algorithm successfully identifies the hydrometeor types that are detected by the CPR- or CALIOP-only algorithms, namely water, 3D-ice, 2D-plate, 3D-ice+2D-plate, liquid drizzle, mixed-phase drizzle, rain, and snow (Figs. 4.10-2 – 4.10-9) with the capability of compensating for the weakness of each stand-alone algorithm. For example, the synergy algorithm identified drizzle and precipitation (Figs. 4.9-5 – 4.9-8) types that were detected by the CPR algorithm alone and was not retrieved in the CALIOP algorithm (Chapter 3). The frequent (>0.15) high cloud top over 15 km in the tropics that could only be detected by the CALIOP algorithm (Figs. 4.8-3) is also covered by the synergy algorithm (Figs. 4.10-3).

(b) The new hydrometeor type derived from the synergistic use of CPR and CALIOP (mixed-phase cloud, water+liquid drizzle, water+rain; Figs. 4.10-10 – 4.10-12) was enabled by complementary capability of CALIOP and CPR that are sensitive to small and large particles, respectively. Such different contributions from CALIOP and CPR reveals the mixed-phase clouds that are mainly composed of water+3D or water+2D. The differing sensitivities of CALIOP and CPR to particle size also suggest that the water+liquid drizzle and water+rain are in a bi-modal states, in which CALIOP is more sensitive to the cloud-sized particles and CPR is more sensitive to the precipitation-sized particles. It should be noted that the mixed-phase cloud and bi-modal types are identified only when CPR and CALIOP have overlapped detections. Therefore, the occurrence frequency indicated in Fig. 4.10 are lower than that in nature.

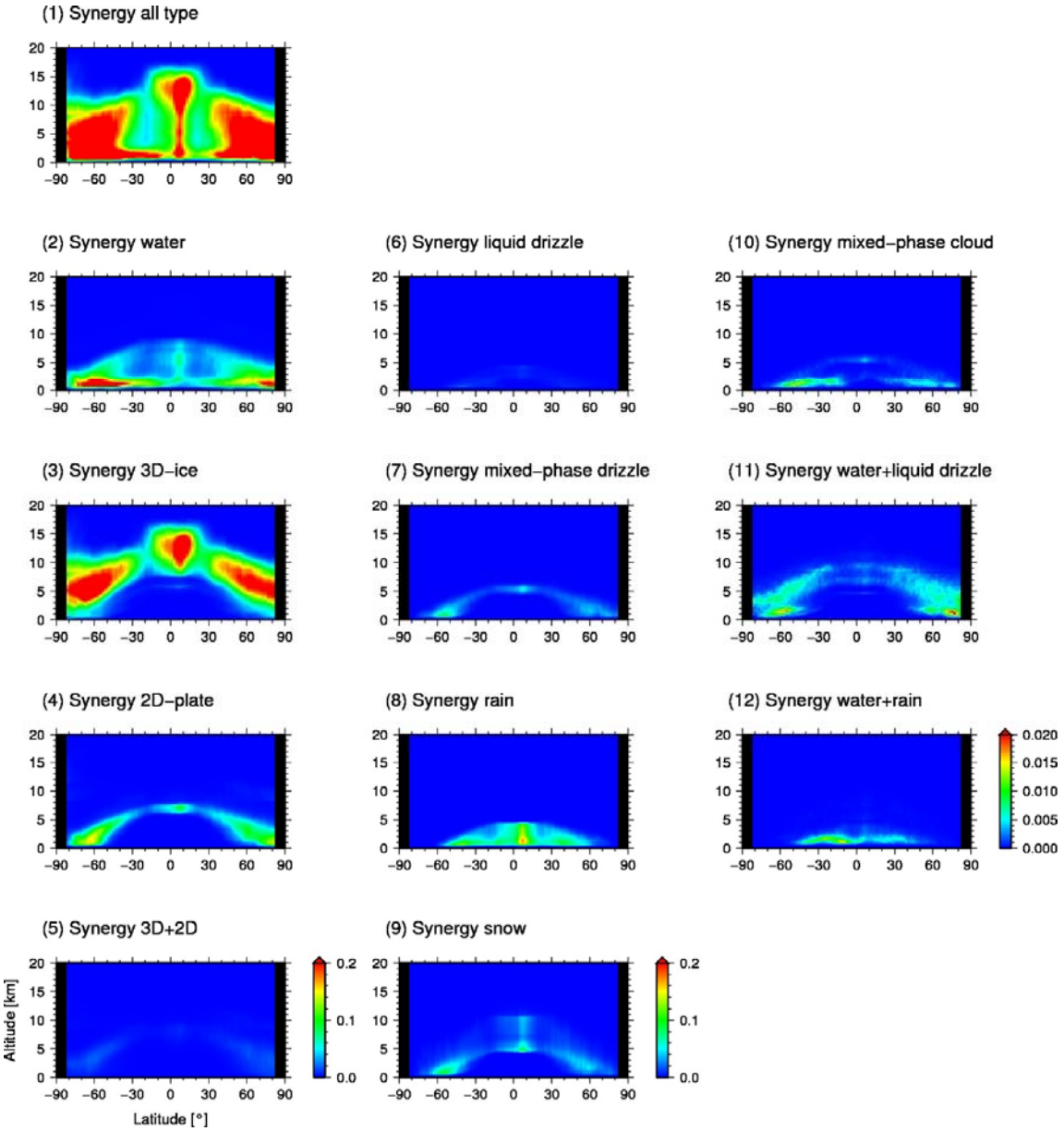

Figure 4.10 Latitude–altitude cross sections of hydrometeor particle types by the synergy algorithm developed in this chapter. The hydrometeor types are (1) all types, (2) water (warm water + supercooled water), (3) 3D-ice, (4) 2D-plate, (5) 3D-ice + 2D-plate, (6) liquid drizzle, (7) mixed-phase drizzle, (8) rain, (9) snow, (10) mixed-phase cloud, (11) water + liquid drizzle, and (12) water + rain. The calculation period and resolution were same as those in Fig. 4.8. The color scale of the three types on the right panel is different from that of left and middle panels because the three types are only derived when CPR and CALIOP observation overlapped, whereas the other types are derived even in the absence of either of the sensor.

It is worth mentioning that the change in the distribution of 2D-plate in the synergy algorithm was not as significant as in the lidar algorithm after the change in the CALIOP pointing direction from near-nadir (0.3°) to off-nadir (3.0°) on 28 November 2007. Studies such as Sassen and Zhu [2009] and Sassen et al. [2012] analyzed the depolarization ratio before and after the tilt, and found a significant increase in the depolarization. The increase in the depolarization would lead to the decrease in the detection of 2D-plate in the lidar algorithm. However, since the CPR algorithm (and therefore the synergy algorithm) was trained by the lidar dataset before the tilt (where the observation of 2D-plate was apparent), the detection of 2D-plate by the synergy algorithm was similar between before and after the change of the pointing direction (Fig. A4.1 in Appendix 4.3). This was because the radar reflectivity field had not changed after the tilt and number of cloud pixels detected by CPR was notably larger than that by CALIOP within the temperature range where 2D-plate dominates. Thus, the synergy algorithm is considered to be applicable to long-term analysis. It is however my future task to optimize the lidar algorithm to the periods after the tilt. The effect of CALIOP's tilting on 2D-plate is discussed in more detail in Appendix 4.3.

4.5.2 Global Mean Statistics of Hydrometeors Occurrence

The global analysis is further summarized here in the form of the global mean occurrence frequency of different hydrometeor types. The total three-dimensional occurrence frequency of all the hydrometeor types is estimated to be 0.104. The breakdown of this into different types shown in Fig. 4.11 illustrates that the 3D-ice type represents the largest contribution, with a mean occurrence frequency of 0.056, which amounts to 53.8% of the total frequency. This is followed by the supercooled water with occurrence frequency of 0.015 (which accounted for 14.3% of the total). The remaining contributions are (in the order of contribution to the total) from 2D-plate with 0.010 (9.2%), rain with 0.006 (5.9%), warm water with 0.006 (5.7%), snow with 0.005 (4.8%), mixed-phase drizzle with 0.002 (2.3%), 3D+2D with 0.002 (1.9%), mixed-phase cloud with 0.001 (1.1%), liquid drizzle with 0.0004 (0.4%), water+rain with 0.0003 (0.3%), water+liquid drizzle with 0.0003 (0.3%), and unknown with 0.00002 (0.02%). In terms of the phase composition, ice phase contributed more than 70% with contributions from water and mixed-phase over 25% and below 5%, respectively.

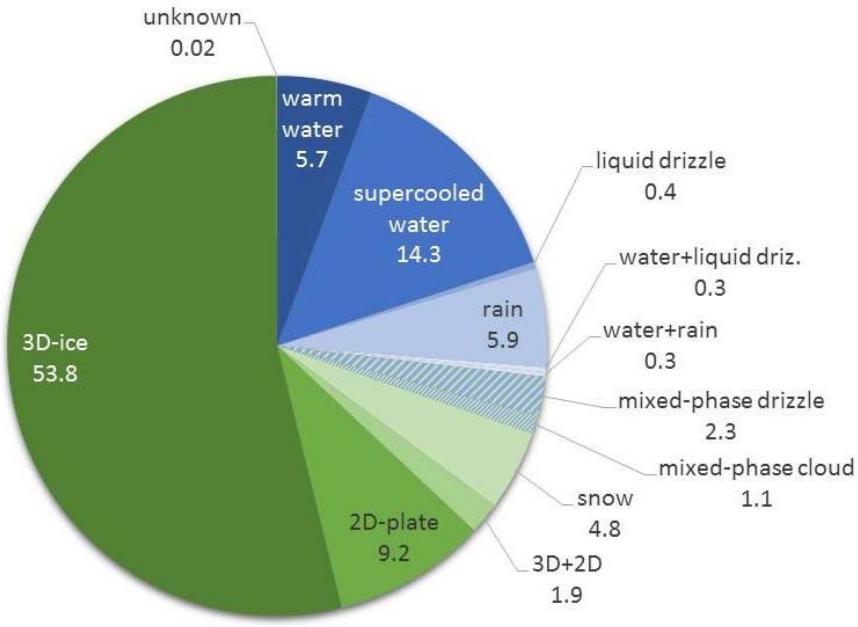

Figure 4.11 Particle type breakdown against global hydrometeor observed by CloudSat and CALIPSO. The blue, green and meshed colors indicate liquid-, ice- and mixed-phase, respectively. The numbers are in percentage.

4.6 Summary

For the propose of developing a satellite-based classification algorithm to discriminate cloud/precipitation phase and cloud crystal shape (hereafter, hydrometeor particle type), this study combined CloudSat/CPR and CALIPSO/CALIOP to relate the lidar-derived hydrometeor particle types to radar reflectivity and temperature. Given that the radar reflectivity can be regarded as a proxy for particle size, the global statistics revealed how the hydrometeor type tends to vary with particle size and temperature. The multi-variable dependency of the hydrometeor type on radar reflectivity and temperature was then interpreted in the context of the freezing process characteristics. In particular, ice phase occurrence is found to increase with decreasing temperature, and the critical temperature for keeping liquid state is dependent on particle size. Ice particle size was also found to vary not only with temperature but also with the particle habit. These observation-based findings are expected to be useful for climate model diagnostics in the representation of freezing processes, particularly in dependency of the cloud phase to temperature and particle size.

The findings were then employed to develop an algorithm that discriminates hydrometeor particle types with a synergistic use of multi-platform satellite measurements of CloudSat and CALIPSO. The

classification algorithm developed is distinctive from the past studies in that it contains statistical information of the hydrometeor types as a continuous function of the reflectivity and temperature identified above. This novel information was exploited to develop a new CPR-alone classification algorithm, which extends the capability of the previous studies that classified the phase per cloud layer [Wang et al. 2013] or within a cloud layer using threshold methods [Ceccaldi et al., 2013]. Another unique aspect of the algorithm is to provide vertically resolved profiles of hydrometeor types by combining the observation of CloudSat and CALIPSO satellites, offering a more complete picture of the hydrometeor occurrence from thin cirrus to precipitating clouds on the global scale. Hence the discrimination scheme conveys the capability of three-dimensional global characterization of hydrometeor types in the atmosphere (Fig. 4.10). For those types already retrieved by the CALIOP algorithm in Chapter 3 (i.e. water, 3D-ice and 2D-plate), the CPR classification developed in this chapter generally gave a consistent latitudinal distribution, with increase in the observation frequency due to capability of the CPR to capture the hydrometeors that had been attenuated in the CALIOP observation. Further, one of the types that are newly introduced is the precipitation type (e.g. rain, snow and drizzle), which are only measured by CPR since CALIOP is attenuated by cloud layers above. The other type is bimodal/mixed-phase type (e.g. water+rain, mixed-phase cloud) which employed the different sensitivities of CPR and CALIOP to particle size. These capabilities were employed to quantify contributions from different types of hydrometeors to the three-dimensional total occurrence of clouds (Fig. 4.11).

Appendix 4.1 Statistical Metrix

The following definitions were used for the statistical metrics in this study.

Radar reflectivity versus temperature dependence of occurrence frequency of CALIOP cloud type (Fig. 4.1a):

$$F_{CAL}\left(dbz\,,temp\,\right)=N_{CAL\,,cloud}\left(dbz\,,temp\,\right)/\sum_{dbz\,,temp}N_{CPR}\left(dbz\,,temp\,\right) \tag{A4.1}$$

where $F_{CAL}(dbz, temp)$ is the occurrence frequency of CALIOP cloud at a given radar reflectivity, dbz, and temperature, $temp$. $N_{CAL,cloud}(dbz, temp)$ is the total number of CALIOP cloud observations at a given dbz and $temp$. $N_{CPR}(dbz, temp)$ is the total number of CPR cloud observations at a given dbz and $temp$.

Radar reflectivity versus temperature dependence of occurrence frequency of CPR hydrometeor type (Fig. 4.1b):

$$F_{CPR}\left(dbz\,,temp\,\right)=N_{CPR\,,hyd}\left(dbz\,,temp\,\right)/\sum_{dbz\,,temp}N_{CPR}\left(dbz\,,temp\,\right) \tag{A4.2}$$

where $F_{CPR}(dbz, temp)$ is the occurrence frequency of CPR hydrometeor at a given dbz and $temp$. $N_{CPR,hyd}(dbz, temp)$ is the total number of CPR hydromete at a given dbz and $temp$.

Radar reflectivity versus temperature dependence of fractional occurrence of a CALIOP cloud type (Figs. 4.1c–4.1e):

$$\begin{aligned}&R\left(type\,,dbz\,,temp\,\right)\\&\quad=N_{CAL\,,cloud}\left(type\,,dbz\,,temp\,\right)/\sum_{type\,,dbz\,,temp}N_{CAL\,,cloud}\left(type\,,dbz\,,temp\,\right)\end{aligned} \tag{A4.3}$$

where $R(type, dbz, temp)$ is the occurrence frequency ratio for a type, $type$ (any one of water, 3D-ice and 2D-plate) at a given dbz and $temp$. $N_{CAL,cloud}(type, dbz, temp)$ is the total number of CALIOP observations for $type$ at a given dbz and $temp$.

Latitude and altitude cross-section of occurrence frequency of a hydrometeor particle type (Figs. 4.8 – 4.10):

$$F_{hyd}\left(type, lat, alt\right) = N_{cloud}\left(type, lat, alt\right) / \left\{\sum_{lat,alt}\left[N_{clear}\left(lat, alt\right) + \sum_{type} N_{cloud}\left(type, lat, alt\right)\right]\right\} \quad \text{(A4.4)}$$

where $F_{hyd}(type, lat, alt)$ is the occurrence frequency of a target type, $type$, at a given latitude, lat, and altitude, alt. $N_{cloud}(type, lat, alt)$ and $N_{clear}(lat, alt)$ are the total number of target $type$ and clear sky observations, respectively, at a given lat and alt.

Appendix 4.2 Correction for Cloud and Precipitation Partitioning

The attenuation corrected radar reflectivity factor at the near-surface (in dBZ) can be derived by adding its path-integrated attenuation (PIA) and water vapor attenuation to the observed radar reflectivity factor at the near-surface [Haynes et al., 2009]:

$$Z_{e,true}(h_{ns}) = Z_{e,att}(h_{ns}) + Z_G(h_{ns}) + PIA \times \frac{H - h_{ns}}{H} \qquad \text{(A4.5)}$$

where $Z_{e,true}(h_{ns})$ is the attenuation corrected radar reflectivity factor at the near-surface and $Z_{e,att}(h_{ns})$ is the attenuated radar reflectivity at altitude h_{ns}. I set h_{ns} to 840-m altitude instead of the lowest altitude to avoid surface clutter. $Z_G(h_{ns})$ is the column gaseous attenuation from the top of the atmosphere to h_{ns} and H is the hydrometeor top height. The PIA can be derived from the difference between the observed surface radar reflectivity (with attenuation by hydrometeors) and the surface radar reflectivity that would have been observed in the absence of the hydrometeor. This clear-sky surface radar reflectivity (or similarly, normalized radar cross section σ^0_{clr} has been estimated in a number of previous studies (Meneghini et al. [2000] and Meneghini et al. [2004] for the PR; Haynes et al. [2009] for the CPR). In this study, the surface radar reflectivity was selected from the closest cloud-free profiles within 10 consecutive pixels in the along-track forward and backward directions [Meneghini et al., 2004]. Where there were no cloud profiles within the 10 pixels, the mean clear-sky surface radar reflectivity was selected from the September to November 2006 period mapped onto every 2° latitude–longitude grids.

From $Z_{e,true}$ in Eq. (A4.5), a precipitation classification was conducted for each profile, according to the threshold defined in Haynes et al. [2009]. Here, Haynes et al. [2009] identified "snow definite," "rain definite," and "no precipitation" profiles where $Z_{e,true}(h_{ns}) > -5dB$, $Z_{e,true}(h_{ns}) > 0dB$, and $Z_{e,true}(h_{ns}) < -15dB$, respectively. In the present study, I checked the consistency of this classification with the initial estimation, and for inconsistent profiles, the initial hydrometeor type at the lowest layer was corrected. Here, I defined the lowest layer as one or several continuous bins containing hydrometeors that appeared for the first time from the surface. Hence, for "rain definite" or "snow definite" profiles, the initially estimated cloud pixels at the lowest layer was corrected to precipitation. If the precipitation layer did not cross the freezing level, the rain-snow separation was kept to 0°C as in the diagram (Fig. 4.2). However, if the precipitation layer crossed the freezing level, this 0°C threshold was modified to 2 °C [Liu, 2008]. Similarly, where there were no precipitation profiles, I corrected the initial precipitation pixels to

the cloud particle type that gave the closest combination of radar reflectivity and temperature in the Fig. 4.1 diagram.

In this correction, the PIA was used to check the attenuation by cloud and precipitation and corrected any profile that was inconsistent with the initially estimated type. Hence, I corrected misclassifications of water cloud to rain that had been difficult to determine whether the low reflectivity (at high temperature over 20°C) was due to scattering by cloud particles or by attenuated precipitating particles.

Appendix 4.3 Effect of CALIOP Tilting to 2D-plate

On 28 November 2007, CALIOP changed its pointing direction from near nadir (0.3°) to off-nadir (3.0°). After the tilt, the depolarization ratio of those classified as 2-D plate would have increased, which would lead some of the 2-D plate to be classified as 3-D ice. The same error analysis described in Section 4.3.2.2 was conducted for two days on 13 September 2007 (before the tilt) and 13 September 2008 (after the tilt). The total error of CloudSat/CALIPSO synergy classification was 6.0% for 2007 and 5.5% for 2008. Further, despite the fact that the change in the pointing direction would be most sensitive to 2D-plate, the contribution of the 2D-plate to the total error was 20.0% for 2007 and 18.9% for 2008, which showed that the error of 2D-plate does not significantly affect the synergy type due to the change of tilting angle.

To investigate the geographical effect of 2D-plate tilting, shown in Fig. A4.1 is the zonal-mean distributions of occurrence of 2D-plate for September-November in 2006 and 2007 (before the change in CALIOP pointing) and in 2008 and 2009 (after the change in the CALIOP pointing). The differences of 2006, 2008, 2009 with respect to 2007 are also shown. As expected, there was a clear change in the detection of 2D-plate in the lidar algorithm between before and after the tilt of the pointing direction. The maximum frequency was approximately 0.036 in 2006 (which was also similar in 2007). The maximum difference between 2006 and 2007 was approximately 0.010 which corresponded to less than 28% of the maximum frequency in 2006 and this was considered to be the maximum variability of the 2D-plate in nature. In contrast, the maximum difference between 2008 and 2007 was approximately 0.032 and this large difference also remained in 2009. This was much larger than the maximum 2D-plate variability in nature and was induced by the tilting.

However, the difference of the 2D-plate detection in the synergy algorithm was not as significant as in the lidar algorithm. The maximum frequency in 2006 was approximately 0.156. The maximum difference between 2006 and 2007 was approximately 0.031 which corresponded to less than 20% of the maximum frequency in 2006. The maximum difference between 2007 and 2008 was approximately 0.034. This corresponded to 22% of the maximum frequency in 2007, which was comparable to the natural variability of 20%. (Note that the maximum difference between 2009 and 2007 was also similar.) This was due to the following three effects: (1) the CPR algorithm (and therefore the synergy algorithm) was trained by the lidar dataset before the tilt (where the observation of 2D-plate was apparent), (2) radar reflectivity field was similar in regardless of the tilt and (3) the number of cloudy pixels detected by CPR was notably larger than that by CALIOP within the temperature range where 2D-plate dominates. In this context, the synergy algorithm was considered to be more reliable than the lidar algorithm.

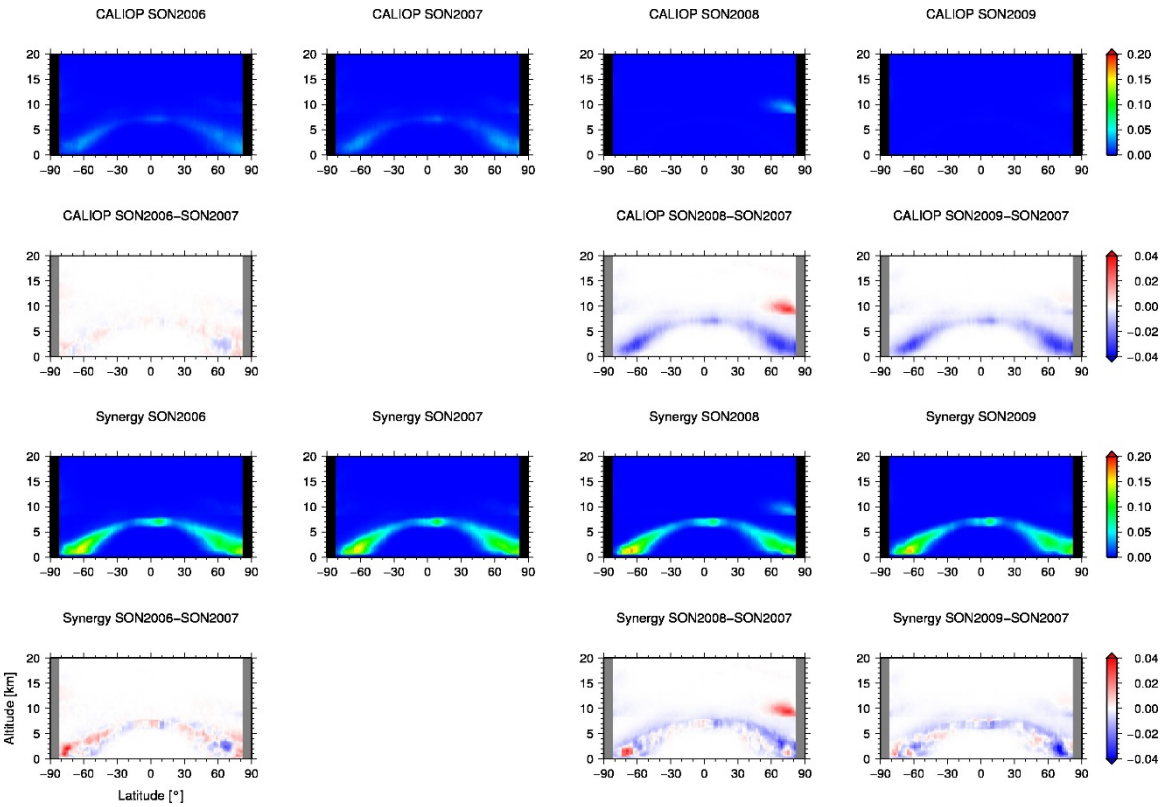

Figure A4.1 Latitude–altitude cross-section of fractional occurrence of 2D-plate obtained from (topmost row) CALIOP algorithm, (second row) their difference relative to SON2007, (third row) from the CPR-CALIOP synergy algorithm, (lowest row) their difference relative to SON2007. (Left) SON 2006, (middle) SON 2007 and (right) SON 2008.

In order to adapt the lidar algorithm to the period after the tilting, the thresholds in the algorithm should be optimized, which is left as my future task. The first parameter "*x*" in the lidar algorithm, which is the proxy of the extinction coefficient, should not have changed as much as the change in the depolarization ratio after tilting. Therefore, only the threshold of second parameter, depolarization ratio, between 2-D plate and 3-D ice would need to be reconsidered when applying the algorithm to data after CALIOP's tilt angle to 3.0°.

Appendix 4.4 Case Study of Type Classification in Arctic

Figure A4.2 shows an example case of hydrometeor particle type classification in the Arctic. Clouds with supercooled particles at the top with solid precipitation underneath are identified between 67° and 70° latitudes.

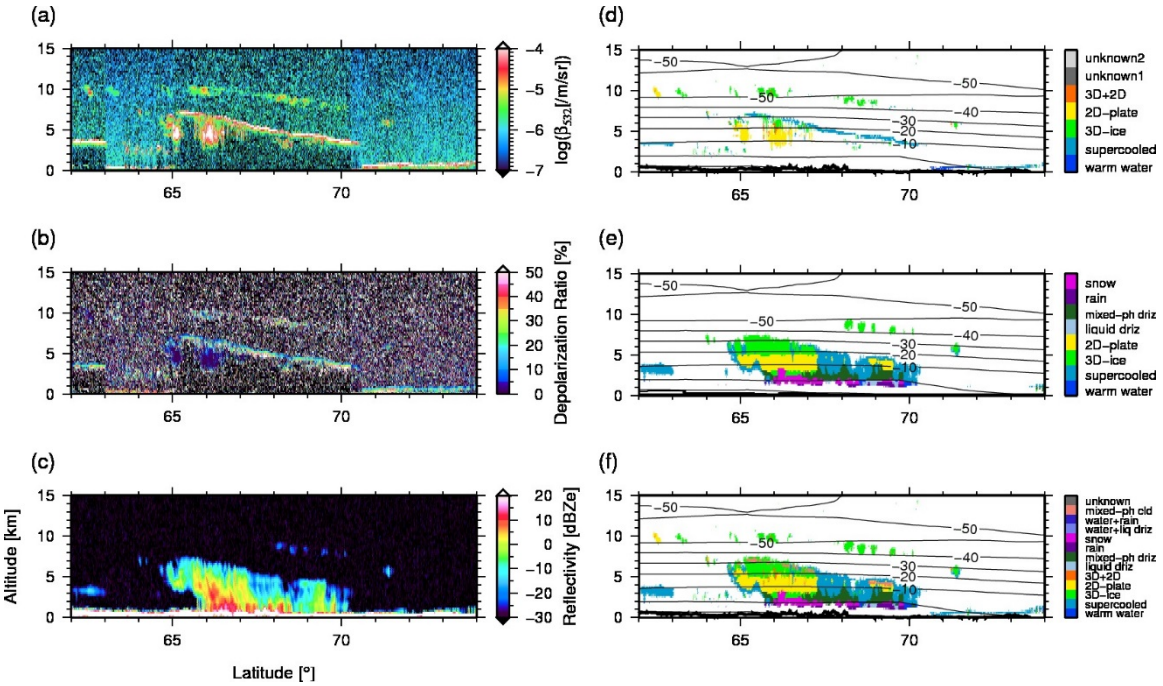

Figure A4.2 Example case of hydrometeor particle type classification: (a) CALIOP backscattering coefficient, (b) CALIOP depolarization ratio, (c) CPR attenuated radar reflectivity, (d) CALIOP hydrometeor particle type, (e) CPR hydrometeor particle type, and (f) CALIOP–CPR synergy hydrometeor particle type. The observation was conducted over Arctic at 0511 UTC on 1 September 2006.

Chapter 5 Improved Hourly Estimates of Aerosol Optical Thickness Using Spatiotemporal Variability Derived from Himawari-8 Geostationary Satellite

5.1 Motivation

The previous chapters projected CloudSat radar and CALIPSO lidar to add a vertical dimension to the horizontal cloud observation provided by past passive measurements. Chapter 4 further showed the nature of the sensor having its own sensitivity and attenuation characteristics and the limitation of single instrument analysis to capture 4-dimensional behavior of hydrometeor. This calls a focus for synergistic measurement and analysis by multiple sensors to complement those drawbacks in each sensor, as highlighted in the previous chapter exploiting CloudSat and CALIPSO to illustrate a more comprehensive measurement from thin cirrus to thick cloud and light precipitation. Hence an algorithm to discriminate different hydrometeors was developed by using the complemental characteristics of the two instruments. The remaining dimension in the atmospheric particle observation is thus the temporal dimension. In principle, the discrimination of different atmospheric particles is also possible by using difference in spatiotemporal variability characteristics among the particles. However, another long-standing issue in remote sensing of an atmospheric particle is the contamination of signals from different particles. Figure 5.1 is an example showing an aerosol optical thickness (AOT) retrieval using the algorithm explained in Section 2.4 and Appendix 2.2, together with the RGB composite image. When only minimum quality control was conducted (i.e. excluding cloud neighboring pixels and solar zenith angle over 70° to avoid low accuracy retrievals), aerosol estimations are strongly affected by the cloud signals, showing ubiquitously distributed high AOTs, which are unrealistic as illustrated in the open ocean. The separation of the signals from two particles, such as clouds and aerosols, are essential in the remote sensing, not only for understanding their microphysical properties, but also for understanding aerosol-cloud interactions and data assimilation. Zhang and Reid [2006] is a study that attempted to carefully extract aerosol retrievals from cloud in their aerosol data assimilation. Their quality assurance procedure removed 70% of the significant outliers, at the expense of 40% of the data that was eliminated. They stated that a strict quality assurance procedure was necessary to remove the outliers that would adversely affect the model performance and propagate errors through the atmospheric field.

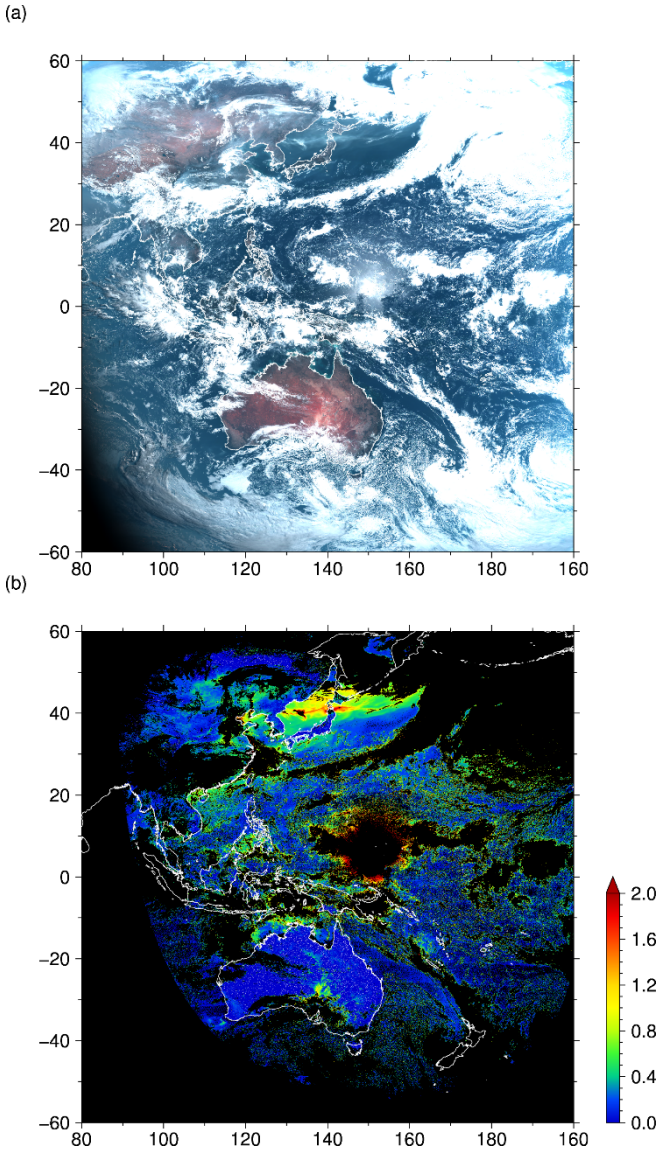

Figure 5.1 AHI image at 1:00UTC on 27 April 2015 from AHI: (a) RGB composite image (red=band3, green=band2, blue=band1) and (b) the retrieved aerosol optical thickness.

As a promising tool to overcome these issues, the Japanese geostationary satellite, Himawari-8, was launched on 7 October 2014, taking a lead in the series of the so-called new generation geostationary satellites [Bessho, 2016]. These satellites have the characteristics to observe at higher frequency, higher spatial resolution and with more channels than the conventional geostationary satellites. An schematic illustration in Fig. 5.2 depicts the advantage of geostationary satellites to observe particles at a high frequency compared to polar-orbiting satellites and how this capability would improve in microphysical property estimates. In aerosol remote sensing, for example, it is difficult to retrieve aerosol properties at a

present time if it laid under a cloud layer. Even if the cloud was not present at the target point a few tens of minutes ago, aerosol estimates would not be available by polar-orbiting satellites either since the satellite would have moved from the target. However, in the case of geostationary satellites, aerosol properties would be retrieved since it continuously monitors the target point; consequently, the retrievals are expected to compensate the missing retrieval at the present time. Hence this study makes the maximum use of this AHI's novel capability in an attempt to address the issues mentioned above. To this end, objectives of this study are twofold: (1) to quantify spatiotemporal variability of aerosol on a 10-minute and a sub-kilometer scale and (2) to develop an hourly algorithm for discriminating cloud from aerosols and minimize missing data over cloudy conditions based on the spatiotemporal variability information obtained in (1). A sophisticated cloud-screening quality control is applied to AOT at every 10 minutes (hereafter $AOT_{original}$, retrieved by the method in Section 2.4) to estimate AOTs with improved accuracy in treating cloud contamination, which are referred to as AOT_{pure}. Hence AOT_{pure} is a subset of $AOT_{original}$ that experienced the strict cloud screening. The AOT_{pure} is further accumulated over the surrounding area and for the past 1 hour to characterize the spatiotemporal variability of AOTs. The variability information is then employed to "interpolate" the missing pixels induced by the cloud and sensor noise. This offers AOT fields with less missing data (referred to as AOT_{merged}) that can be used to better monitor aerosol distributions. Note that the context of this chapter is published in Kikuchi et al. [2018].

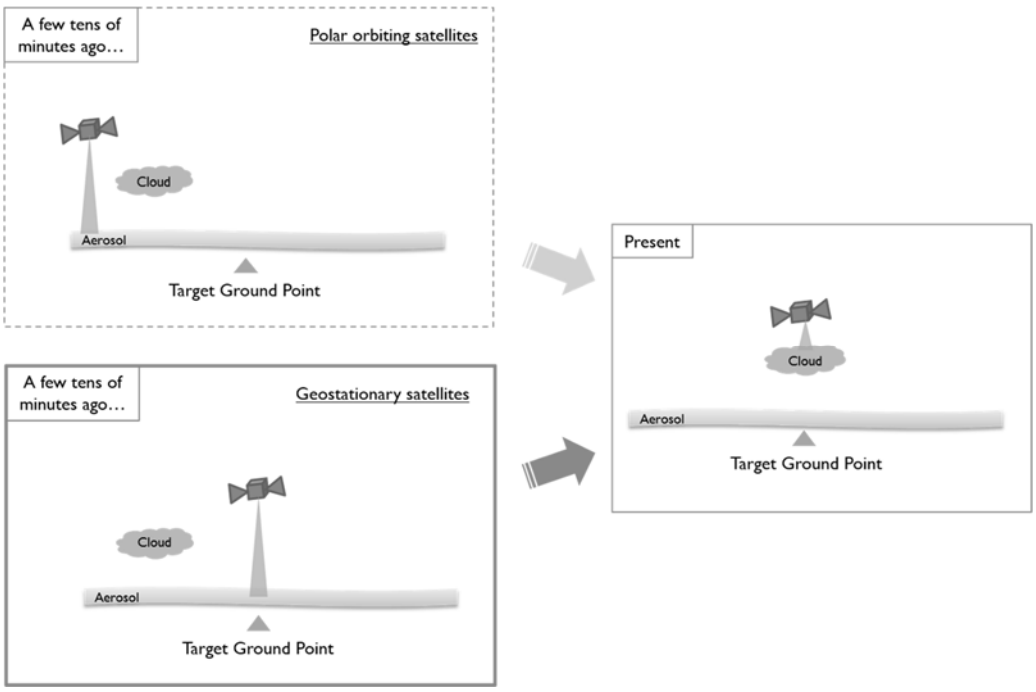

Figure 5.2 Schematic illustration of the difference in aerosol observation between polar orbiting and geostationary satellites.

5.2 Aerosol Spatiotemporal Variability

The $AOT_{original}$, derived by the method in Section 2.4, was first analyzed to investigate the spatiotemporal variability of aerosol at 10-minute and sub-km scale for use in the subsequent hourly combined algorithm described in the following section. To recall, the $AOT_{original}$ was derived based on the look-up-table method by Higurashi et al. [1998] and Fukuda et al. [2013] and the aerosol pixels were selected beforehand by the cloud detection algorithm, CLAUDIA, by Ishida and Nakajima [2009] and Ishida et al. [2011] (Section 2.4 and Appendix 2.2). In this study, the aerosol spatiotemporal variability was quantified in the form of a simple root mean square difference (RMSD) of AOT, which is given as

$$\sigma(\Delta L, \Delta t) = \sqrt{\frac{1}{N}\sum_{\Delta l \in \Delta L, \Delta \tau \in \Delta t}\{\Delta AOT(\Delta L, \Delta t)\}^2} \qquad (4.1)$$

where $\Delta AOT(\Delta L, \Delta t)$ is the difference in AOT between the two locations that satisfy the condition $\Delta l \in \Delta L, \Delta t \in \Delta t$. Here, Δl and $\Delta \tau$ is the distance and time difference between the two locations, respectively. N is the total number of pixels that satisfy the condition $\Delta l \in \Delta L, \Delta t \in \Delta t$.The time difference Δt was set as 6 slots of 0, 10, 20, 30, 40, 50 minutes' past. The distance ΔL was set as 6 slots of every 2.5 km up to 12.5 km. The ΔL threshold of 12.5 km was selected because this was the longest distance where the correlation coefficient with the center AOT (ΔL = 0.0 km) was above 0.65 (from the statistic at 01:00 UTC on 12th July 2015). The distance ΔL of 12.5 km within the total time slot of 1 hour corresponds to the moving speed of approximately 3.5 m/s. This means that the choice of the domain size of 12.5km and the time period of 1 hour takes into account those aerosols that are advected as slowly as 3.5m/s. In deriving $\sigma(\Delta L, \Delta t)$, the combination of the two locations was considered for all the pixels over the full disk images every 00 UTC minutes on 1, 2, 4, 5 UTC for arbitrary 5 days of data after official operation of AHI (12, 20, 28, and 30 July, and 5 August 2015), accounting for more than 32.2 million target aerosol pixels. Data on 03:00 UTC was not used because no observation data at 02:40 UTC is available because of housekeeping of the Himawari-8. Since the magnitude of $\sigma(\Delta L, \Delta t)$ is found to strongly vary with the AOT values at the center, $\sigma(\Delta L, \Delta t)$ was calculated separately for different discrete ranges of the target AOT (hereafter referred to as the AOT category) of 0.1, 0.25, 0.4, 0.5, 0.55, 0.6, 0.65, 0.7, 0.75, 0.8, 0.85, 0.9, and 1.0. AOT over 1.0 was included in the same category as 1.0 because $\sigma(\Delta L, \Delta t)$ cannot be calculated due to a lack of observation that satisfy the given condition (i.e. either one of the combination of 6 distance slots and 6 time-difference slots). An AOT category was defined to include AOTs that fall between the current and the previous thresholds (e.g., $0.4 < \text{AOT} \leq 0.5$ was registered to AOT category of 0.5). $\sigma(\Delta L, \Delta t)$ was derived with a particular care not to include cloudy pixels. After removing the cloudy pixels determined by the CLAUDIA algorithm, pixels were further tested on a "near-cloud quality control", where the combination of the two locations were excluded from the analysis if either of the pixel was within 12.5 km of a cloudy pixel, in order to eliminate cloud-contaminated aerosol pixels from the calculation.

Figure 5.3 shows the spatiotemporal variability of AOT derived from the algorithm in the form of RMSD as a function of both spatial distances and time differences from the center pixels for different AOT magnitudes at the center pixels (i.e. AOT categories). $\sigma(\Delta L = 0, \Delta t = 0)$ was 0 in all AOT categories because it corresponds to the center pixel at the same observation time. In general, the $\sigma(\Delta L, \Delta t)$ tends to monotonically increase as the spatial distance ΔL and time difference Δt increases. As the magnitude of the AOT at the center (i.e., AOT category) increases, $\sigma(\Delta L, \Delta t)$ is also found to increase. In a given AOT category, $\sigma(\Delta L, \Delta t)$ for land was generally larger than that for ocean although the land-ocean difference in the temporal variability at the center [i.e. $\sigma(\Delta L = 0, \Delta t)$] was not so significant (as also indicated in Fig. 5.4a) compared to other $\sigma(\Delta L \neq 0, \Delta t)$. Figure 5.3 illustrates how the RMSD systematically varies both in space and time, suggesting that the spatial and temporal variabilities are related to each other. This means that the spatial scale of a given variance can be "translated" into an equivalent temporal scale leading to the variance. For example, the temporal variance within 10 minutes at the center pixel $\sigma(\Delta L = 0, \Delta t = 10min)$ for the AOT category of 0.5 ($0.4 < \text{AOT} \leq 0.5$) was 0.12 over ocean and 0.14 over land (Fig. 5.4a). According to the fitting curve of RMSD as a function of spatial distance, as shown in Fig. 5.4b, these variances were equivalent to the distance of approximately 8.0 km for ocean and 2.9 km for land. In other words, the temporal variance within 10 minutes can be interpreted to be equivalent with the spatial variance within 8.0 km for ocean and 2.9 km for land. In summary, the AOT varied by 22.0% to 31.8% in time within 10 minutes, and by 15.2% to 31.3% in space within 2.5 km. The AOT variability within 10 minutes or 2.5 km, when normalized by AOT itself, is also found to be larger in high AOT categories than in low AOT categories, suggesting the necessity to quantify $\sigma(\Delta L, \Delta t)$ for different AOT categories.

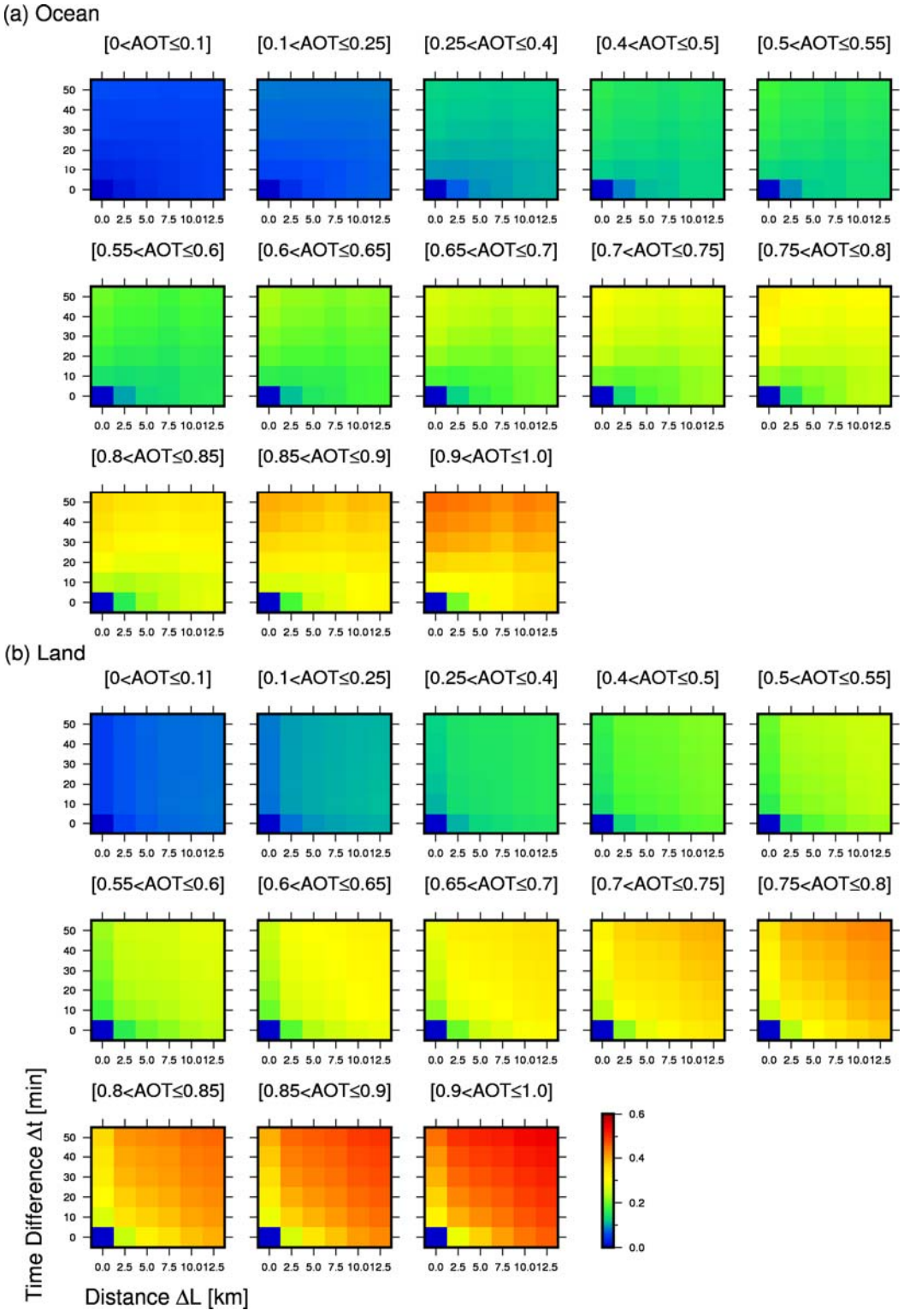

Figure 5.3 RMSD of AOT $\sigma_{\Delta L,\Delta t}$ over (a) ocean and (b) land. The "distance" axis indicates the distance from the center pixel in kilometers. The "time difference" axis indicates the difference in time from the center pixel in minutes.

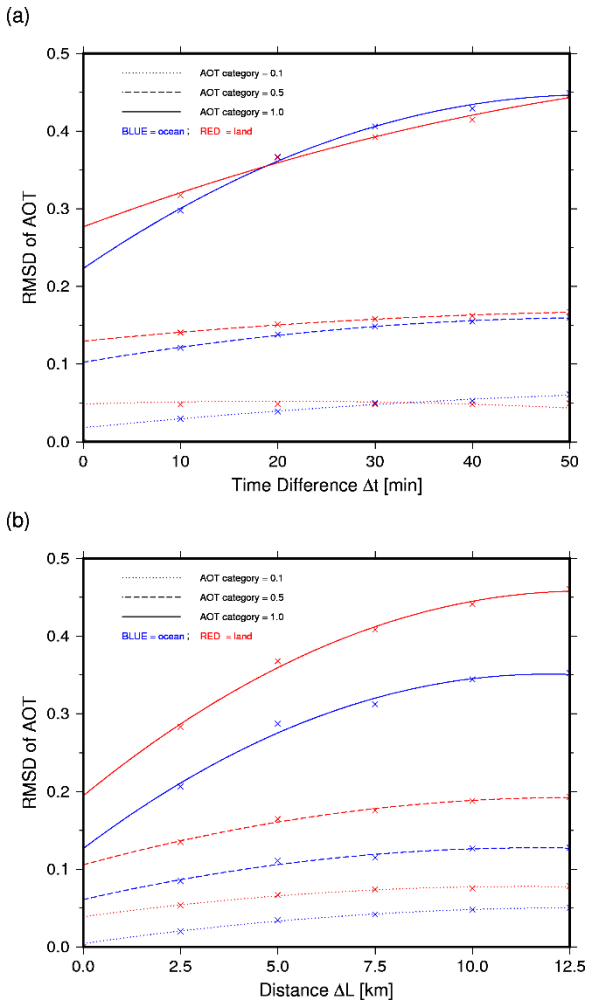

Figure 5.4 Root mean square difference in AOT from center pixel (a) observed at the same place as the center and (b) observed at the same time as the center pixel. AOT(x_0, y_0) categories of 0.1,0.5 and 1 are indicated in dotted, dashed and solid lines, respectively. Blue is for over ocean and red is for over land. The "distance" axis indicates the distance from the center pixel. The "time difference" axis indicates difference in time from the center pixel. Quadratic curve fitting are also shown to each of the plot.

Next, the differences in spatiotemporal variability characteristics between aerosol and cloud-contaminated aerosol were demonstrated in Figs. 5.5 and 5.6. In Fig. 5.5, the $\sigma(\Delta L, \Delta t)$ was populated for all the AOT categories over both land and ocean, and compares the aerosol fields with and without the near-cloud quality control. Hence Fig. 5.5a corresponds to the mean field of all the $\sigma(\Delta L, \Delta t)$ panels in Fig. 5.4 and Fig. 5.5b was derived even if the pixels was within 12.5 km of a cloud pixel.

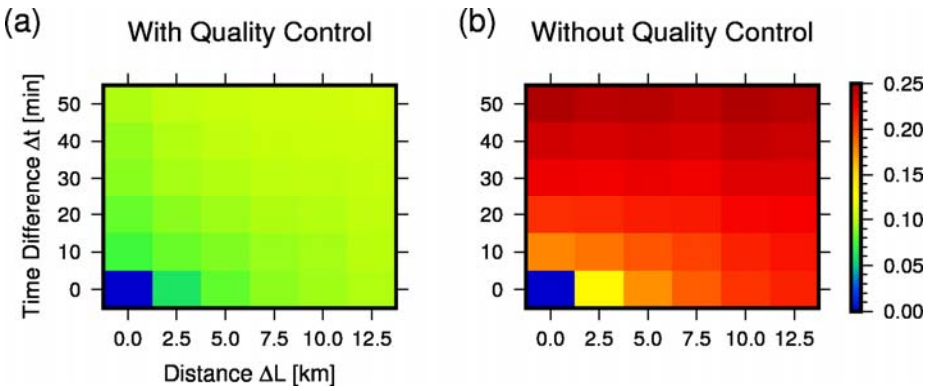

Figure 5.5 RMSD of AOT $\sigma_{\Delta L,\Delta t}$ (a) with and (b) without near-cloud quality control. The statistic was taken for all AOT categories and includes both land and ocean. The definition of the axes is same as that in Fig. 5.3.

As expected, the RMSD field without the quality control was higher than that with the quality control due to the presence of cloud-contaminated pixels. The mean RMSD field with the quality control varied 0.06–0.11 within 12.5 km and 1 hour. The mean RMSD field without the quality control, in contrast, varied 0.13–0.25 within 12.5 km and 1 hour. The variability without quality control was substantially larger than that with quality control in all 10 minutes/2.5 km steps; their difference was between 0.07–0.15.

Significant influences of cloud fields on aerosol variability are also highlighted in Fig. 5.6, which shows a case that captured the aerosol transport in 10 minutes from the continent crossing toward northern Japan on 27 April 2015 at 00:50UTC (Fig. 5.6a) and 01:00UTC (Fig. 5.6b). Note that only the minimum quality control was conducted in $AOT_{original}$ and therefore the analysis included cloud-contaminated pixels. As illustrated in Fig. 5.6c showing the difference in AOT between the two times, aerosol fields over northern Japan was fairly homogeneous during the 10 minutes, giving low AOT differences. Over southern Japan, by contrast, the movement of broken clouds (20°–30°N and 165°–180°E) and the cloud edges related to the front (20°–40°N and 130°–160°E) was larger, giving high AOT differences.

Both the analysis in Fig. 5.5 and 5.6 showed the clear differences in the spatiotemporal variability of aerosol fields that are unaffected by clouds from those that are cloud-contaminated. This motivated us to take into account the difference in the variabilities between aerosol and cloud to eliminate cloud-contaminated AOT retrievals using the AHI's 10-minute observation over an hour.

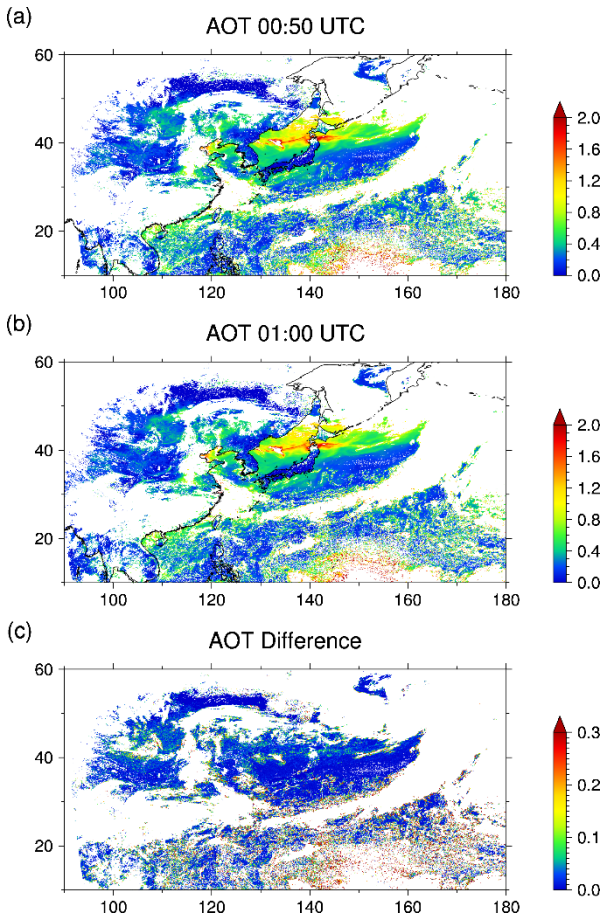

Figure 5.6 $AOT_{original}$ from the AHI's 10-minute observation over East Asia on 27 April 2015 at (a) 00:50 UTC; (b) 01:00 UTC and (c) their absolute difference.

5.3 Hourly Combined AOT Algorithm

Based on the spatiotemporal AOT variability obtained from the analysis described in the previous section, an hourly combined algorithm was introduced which derives two types of AOTs: AOT_{pure} and AOT_{merged}. AOT_{pure} is an extracted set of the $\mathrm{AOT}_{\mathrm{original}}$ with strict cloud screenings (which is the reason why it is named as the "pure" AOT). AOT_{merged} is a dataset derived from AOT_{pure} through the optimum interpolation based on the variability information into the point of interest (in space and time) even when the $\mathrm{AOT}_{\mathrm{original}}$ at the location and time was missing. This provides aerosol fields that contain as much AOT retrievals as possible with cloud contamination minimized based on the differences in spatiotemporal variability characteristic between aerosol and cloud. Detailed procedures for obtaining AOT_{pure} and AOT_{merged} are described below.

5.3.1 AOT_{pure}

In deriving AOT_{pure}, the AOT at a point of interest, $AOT_{est}(x_o, y_0, t_0)$, was first estimated by interpolating $AOT_{original}$ included in the radius of 12.5 km and past 1 hour (excluding the center pixel) with weights defined according to the RMSD computed above. The AOT_{est} is thus obtained as

$$AOT_{est}(x_o, y_0, t_0) = \sum_{i=1}^{n} w_i \, AOT_{original}(x_i, y_i, t_i) \tag{4.2}$$

$$w_i = \frac{\frac{1}{\sigma_{original}(x_i, y_i, t_i)^2}}{\frac{1}{\sigma_{est}(x_o, y_0, t_0)^2}} \tag{4.3}$$

$$\frac{1}{\sigma_{est}(x_o, y_0, t_0)^2} = \sum_{i=1}^{n} \frac{1}{\sigma_{original}(x_i, y_i, t_i)^2} \tag{4.4}$$

where $AOT_{original}(x_i, y_i, t_i)$ and $\sigma_{original}(x_i, y_i, t_i)^2$ are the $AOT_{original}$ and the error variance at a pixel (x_i, y_i, t_i), respectively. In this analysis, all the effective pixels that gave $AOT_{original} \geq 0$, that were cloud-free within 12.5 km from the pixel (x_i, y_i, t_i) and that were within 12.5 km and past 50 minutes from the center (x_o, y_0, t_0) were considered as (x_i, y_i, t_i). Sunglint regions where the cone angle of solar-to-surface and surface-to-sensor direction was below 30.0° over ocean were excluded. *n* was the total number of the effective pixels within the analysis domain of 12.5 km radius and past 1 hour from (x_o, y_0, t_0). $\sigma_{original}(x_i, y_i, t_i)^2$ was the error variance to estimate $AOT_{est}(x_o, y_0, t_0)$ (at the center) from $AOT_{original}(x_i, y_i, t_i)$ (at the surrounding and past), and therefore, it can be described by the RMSD of AOTs that were (x_o, y_0, t_0) and (x_i, y_i, t_i) apart [Awaji et al., 2009]. Consequently, $\sigma_{original}(x_i, y_i, t_i)$ was taken from the LUT of $\sigma(\Delta L, \Delta t)$ that was already calculated in Section 5.2. Equation (4.2) illustrates that the estimated AOT, AOT_{est}, is derived as the mean of surrounding and past $AOT_{original}$ weighted according to the inverse of their error variances. Assuming that the inverse of the error variance quantifies the accuracy of the AOT at each pixel, Eq. (4.4) implies that the estimated accuracy at the center pixel, $\frac{1}{\sigma_{est}(x_o, y_0, t_0)^2}$, is given by the sum of the accuracies of the $AOT_{original}$, $\frac{1}{\sigma_{original}(x_i, y_i, t_i)^2}$, over surrounding locations and past times.

Based on the AOT_{est} derived above, the AOT_{pure} was estimated as

$$AOT_{pure}(x_o, y_0, t_0) =$$

$$\begin{Bmatrix} AOT_{original}(x_o, y_0, t_0) & if\ AOT_{original}(x_o, y_0, t_0) \le AOT_{est}(x_o, y_0, t_0) + 2.58\sigma_{pure}(x_o, y_0, t_0) \\ missing\ value & else \end{Bmatrix} \quad (4.5)$$

$$\sigma_{pure}(x_o, y_0, t_0) = \begin{Bmatrix} \sqrt{\sigma(x_o, y_0, t_0)^2 + \sigma_{est}(x_o, y_0, t_0)^2} & if\ \ AOT_{pure}(x_o, y_0, t_0) \neq missing\ value \\ missing\ value & else \end{Bmatrix} \quad (4.6)$$

where $\sigma(x_o, y_0, t_0)^2$ was the error variance at the center pixel and $\sigma_{pure}(x_o, y_0, t_0)$ was the estimated error of AOT_{pure}. Equation (4.5) means that if the observed AOT, $AOT_{original}(x_o, y_0, t_0)$, was above the upper threshold at the 99% confidence interval, then the center pixel was considered to be contaminated by cloud and was therefore excluded from the AOT_{pure}. The error variance at the center pixel $\sigma(x_o, y_0, t_0)^2$ could not be derived from $\sigma(\Delta L, \Delta t)$ LUT because $\sigma(\Delta L = 0, \Delta t = 0)$ was zero (i.e., no difference in AOT at the center pixel at the same observation time). Therefore, $\sigma(x_o, y_0, t_0)$ was estimated by applying quadratic fitting to $\sigma(\Delta L, \Delta t)$ to every AOT category (an example shown in Fig. 5.4). Two values of $\sigma(x_o, y_0, t_0)$ can be derived since the value could be estimated from both distance and time direction and therefore the final $\sigma(x_o, y_0, t_0)$ was derived by taking the root mean square of the two values. $\sigma(x_o, y_0, t_0)$ contains errors arising from the sensor noise and the surface reflectance estimates that vary in time and space. Note that $\sigma(x_o, y_0, t_0)$ does not incorporate the errors induced by the algorithm assumptions nor the systematic bias in the surface reflectance estimates (i.e. without spatiotemporal variability). Therefore, the error of AOT_{pure} at the center [$\sigma_{pure}(x_o, y_0, t_0)$ in Eq. (4.6)] was defined as the square root addition of $\sigma(x_o, y_0, t_0)^2$ and the estimated error variance induced by the estimation from surrounding and the past pixels ($\sigma_{est}(x_o, y_0, t_0)^2$) [Awaji et al., 2009]. Assuming that the error variance follows the normal distribution, the true AOT was expected to be below $2.58\ \sigma_{pure}(x_o, y_0, t_0)$ (i.e., the upper limit of the 99% confidence interval) from $AOT_{est}(x_o, y_0, t_0)$. Therefore, if the $\mathrm{AOT_{original}}$ was below this threshold, $\mathrm{AOT_{original}}$ was registered as $AOT_{pure}(x_o, y_0, t_0)$, otherwise it was assigned to be a missing value assuming such a value largely deviated from $AOT_{est}(x_o, y_0, t_0)$ is likely to suffer from cloud contamination. Note that $AOT_{pure}(x_o, y_0, t_0)$ was also assigned to be a missing value if a cloudy pixel existed within 12.5 km of (x_o, y_0, t_0) or if the number of effective pixels to derive $AOT_{est}(x_o, y_0, t_0)$ was below 20% of the total possible number of observations within a distance of 12.5 km and 1 hour. $\sigma_{pure}(x_o, y_0, t_0)$ was not calculated if $AOT_{pure}(x_o, y_0, t_0)$ was a missing value.

5.3.2 AOT_{merged}

Next, AOT_{merged} was derived by substituting a set of AOT_{pure} within the radius of 12.5 km and past 1 hour as a new $AOT_{original}$ in Eq. (4.2)-(4.4) and defined the newly calculated AOT_{est} to be the AOT_{merged}. Note that $AOT_{merged}(x_o, y_0, t_0)$ was different from $AOT_{est}(x_o, y_0, t_0)$ in that the calculation of $AOT_{merged}(x_o, y_0, t_0)$ included the center pixel (x_o, y_0, t_0), whereas $AOT_{est}(x_o, y_0, t_0)$ did not. Accordingly, the equations defining AOT_{merged} are given as follows:

$$AOT_{merged}(x_o, y_0, t_0) = \sum_{i=0}^{N} W_i \, AOT_{pure}(x_i, y_i, t_i) \tag{4.7}$$

$$W_i = \frac{\frac{1}{\sigma_{pure}(x_i, y_i, t_i)^2}}{\frac{1}{\sigma_{merged}(x_o, y_0, t_0)^2}} \tag{4.8}$$

$$\frac{1}{\sigma_{merged}(x_o, y_0, t_0)^2} = \sum_{i=0}^{N} \frac{1}{\sigma_{pure}(x_i, y_i, t_i)^2} \tag{4.9}$$

where $\sigma_{merged}(x_o, y_0, t_0)$ was the estimation error of AOT_{merged}. N is the total number of pixels within the calculation domain of 12.5 km radius and past 1 hour from (x_o, y_0, t_0).

The overall flow of the hourly combined algorithm is shown in Fig. 5.7. In summary, the algorithm (1) estimates the variability of AOT in the spatiotemporal window of an hour and 12.5km prior, and (2) derives the hourly combined AOTs using the variability information taking into account the time difference and distance of the past and surrounding pixels from the point of interest. Note that the hourly combined retrievals derived in this study (AOT_{pure} and AOT_{merged}) means an optimal estimation of AOT at a certain time, rather than an estimate of the average state over an hour.

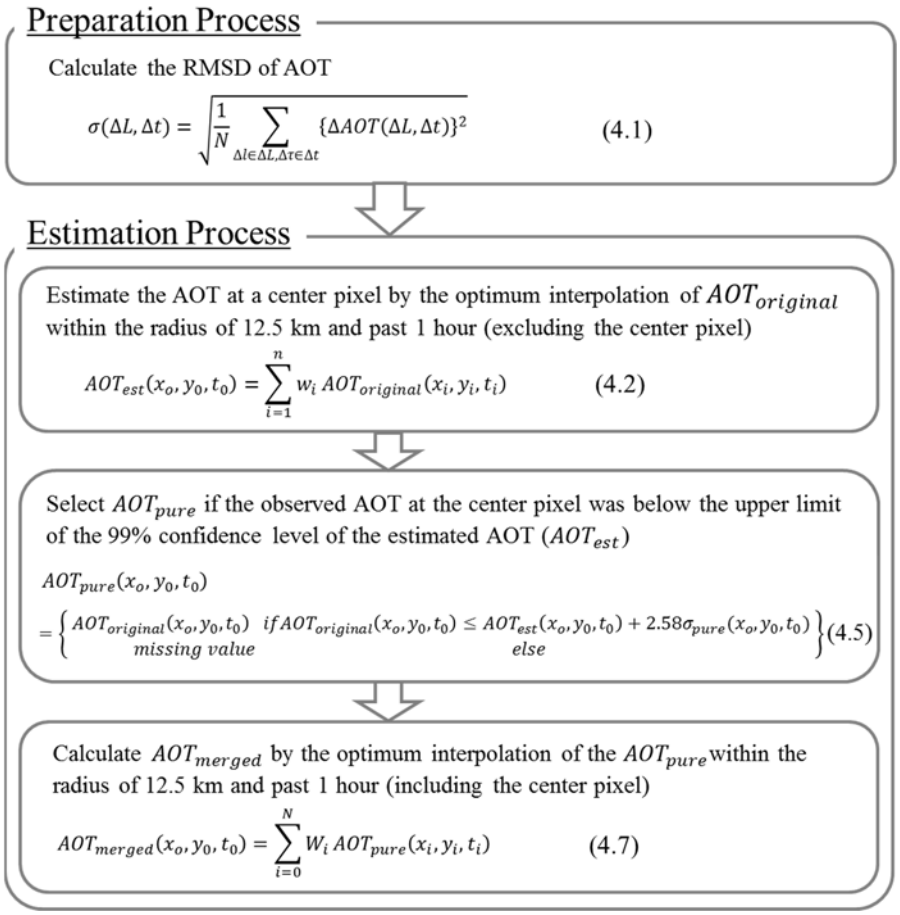

Figure 5.7 Flow of the hourly combined algorithm. The equation numbers correspond to that in the text.

5.3.3 Algorithm Uncertainty

The uncertainty in the hourly combined algorithm is primarily attributed to the representativeness of the aerosol spatiotemporal variability in Fig. 5.3, which is derived statistically from the full disk observation of Himawari-8, giving the mean state of the variability. Since AOT_{pure} is obtained through the cloud-screening procedure using the 99% confidence level threshold calculated from the RMSD field, there are cases when the screening threshold become too strict. One such example is when applying the algorithm to regions close to an aerosol source where aerosol variability from its emission is larger and is beyond the mean field of the variability. Although the spatiotemporal variability is derived per AOT category to minimize this effect, the future work will involve improving the RMSD field by taking the statistics for each month and regionally, which is expected to reflect differences in aerosol types and its variability among the seasons and geographical conditions.

5.4 Case Study

As an example of the hourly combined estimates described in Section 5.3, shown in Fig. 5.8 is the $AOT_{original}$, AOT_{pure}, and AOT_{merged} retrieved at 01:00 UTC on 5 August 2015 around northern Japan. The hourly combined AOTs were derived using AHI data from 00:10 UTC and 01:00 UTC. Cloudy and missing pixels are indicated in gray and black, respectively. Although the $AOT_{original}$ was successfully retrieved in general, it sometimes gave a high value (close to 1.0) around the cloud edge because of misclassification of cloudy versus clear pixels. Some missing $AOT_{original}$ pixels were also present because the parameters derived were outside the LUT.

Using one hour dataset, AOT_{pure} successfully excluded pixels with AOTs that are exceptionally higher than those estimated from the surrounding and past pixels, and therefore minimized contaminations of cloudy pixels. As a result of this quality control, the numbers of effective AOT_{pure} and AOT_{merged} pixels became less than that of the $AOT_{original}$ in the upper left corner of Fig. 5.8 (44°–45° latitude and 135°–136° longitude). The AOT_{pure} is found to become missing particularly nearby blocky clouds that were produced intermittently over land and moving in the southeast direction as a whole. The number of effective AOT_{pure} within 12.5 km and past 1 hour was below the threshold of 20% of the total possible number within the domain, which resulted the AOT_{merged}, derived from the optimal interpolation of the AOT_{pure}, to be missing values. In the southern region of Fig. 5.8 (40°–41° latitude and 136°–140° longitude), the AOT_{merged} gave a seamless distribution of AOT even when the $AOT_{original}$ and AOT_{pure} were missing due to sensor noise, because the AOT_{merged} can be derived if there are sufficient number of observations in the past and/or surrounding.

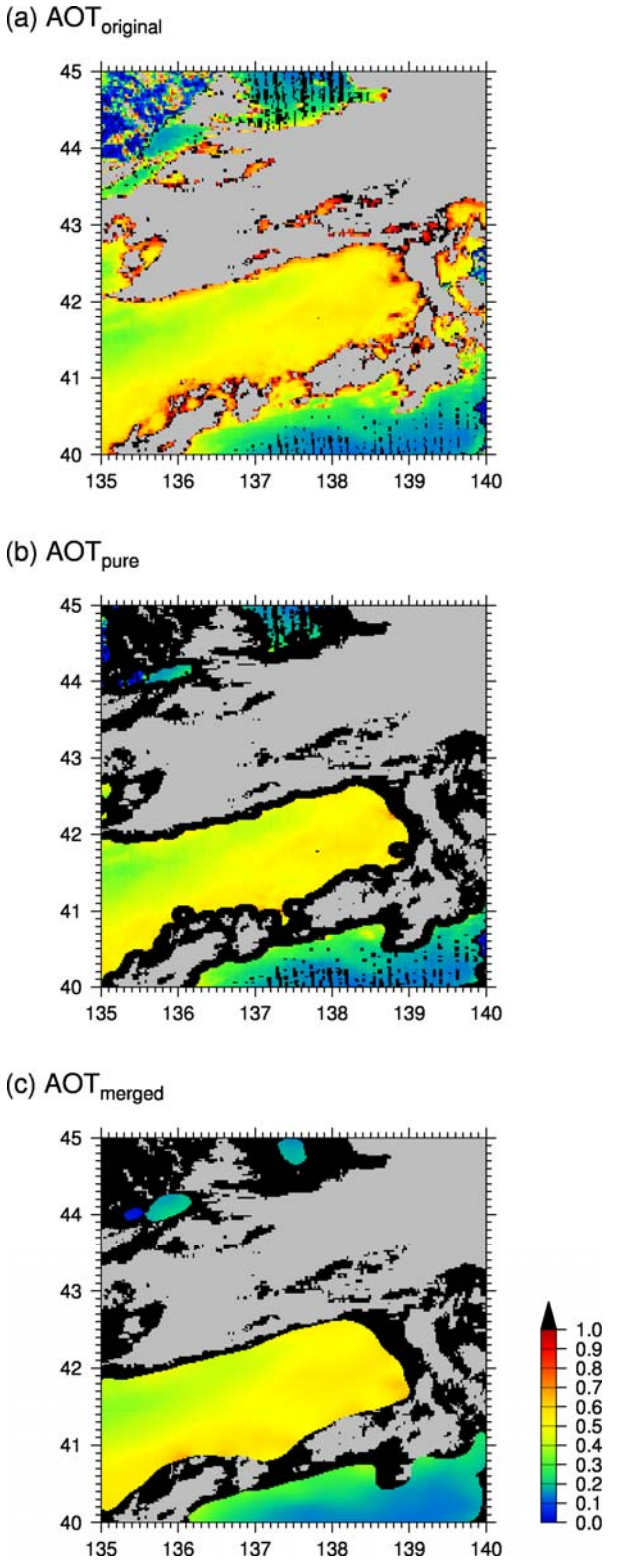

Figure 5.8 AHI image on 5 August 2015 around northern Japan: (a) $AOT_{original}$ at 01:00 UTC, (b) hourly combined AOT_{pure} from 00:10 to 01:00 UTC, (c) hourly combined AOT_{merged} from 00:10 to 01:00 UTC. Cloudy and missing pixels are indicated in gray and black, respectively.

5.5 Validation

The hourly combined AOTs were validated against an independent observation of AERONET in Fig. 5.9, which also shows $AOT_{original}$ for comparison. AERONET is a network of sun and sky scanning radiometers that are used to observe aerosol properties established by the NASA [Holben et al., 1998] and AOT at 500 nm were used from Level 2.0 product [Smirnov et al., 2000]. AERONET ground-based sites were selected where Level 2.0 was available with more than 10 data samples for each of the three AOTs ($AOT_{original}$, AOT_{pure}, and AOT_{merged}) after 7 July when the official operation of Himawari-8 started. Four sites satisfying these criteria are available over the Asian-Oceanian region: Dalanzadgad in Mongolia, Kuching in Malaysia, Toyama in Japan, and Ussuriysk in Russia. The geolocation, observation period, and the number of observations for each site are listed in Table 5.1. For each AERONET site, an AHI pixel was extracted that was observed over the site. One-to-one comparisons were conducted when AERONET data were available during 10 minutes of AHI observation. If more than one AERONET observation was available during AHI's 10-minute observation, then AERONET AOTs were averaged. Since AOT_{pure} is a subset of $AOT_{original}$, the relationship between the blue and gray plots in Fig. 5.9 is as follows: blue points (=AOT_{pure}) + gray points (= cloud-contaminated $AOT_{original}$) = total $AOT_{original}$. The definitions of the statistical metrics used in the figures are described in Appendix 5.1.

Table 5.1. Information on AERONET sites and cruise used in this study.

Observation Site	Latitude [degrees]	Longitude [degrees]	Observation Period[*1]	Number of Observations		
				$AOT_{original}$	AOT_{pure}	AOT_{merged}
Dalanzadgad, Mongolia	43.577	104.419	2015/7/7–2015/7/26	128	43	60
Kuching, Malaysia	1.491	110.349	2015/7/7–2015/10/26	258	32	37
Toyama, Japan	36.699	137.187	2015/7/7–2015/7/29	240	73	68
Ussuriysk, Russia	43.700	132.164	2015/7/7–2015/7/29	163	50	55
Total	-	-	-	789	198	220

Cruise	Latitude [degrees] Start / End	Longitude [degrees] Start / End	Observation Period	Number of Observations		
				$AOT_{original}$	AOT_{pure}	AOT_{merged}
Okeanos Explorer 4	20.829 / 20.666	-160.826 / -161.139	2015/7/11–2015/7/23	30	1	5
Okeanos Explorer 7	20.378 / 17.608	-163.045 / -169.627	2015/9/14–2015/9/26	16	4	1
Total	-	-	-	46	5	6

[*1] The operation of AHI started on 7 July 2015. The observation end date was the date when the latest Level 2.0 AERONET data were available at the time of writing.

Overall, the AOT_{pure} and AOT_{merged} showed successful elimination of cloud contamination with high values found in the $AOT_{original}$. In all sites, the AOT_{pure} and AOT_{merged} agreed better with the AERONET AOT than the $AOT_{original}$ did, giving a lower root mean square error (RMSE). The correlation of the AOT_{pure} and AOT_{merged} with respect to the AERONET was also better at most of the sites (except for the AOT_{pure} at Toyama). The systematic overestimation and underestimation, or bias, in the hourly combined products was due to the errors in the $AOT_{original}$, which was discussed in [Fukuda et al., 2013], in which the largest influence on the $AOT_{original}$ retrieval was considered to be due to errors in surface reflectance and aerosol model setting including single scattering albedo. The errors in surface reflectance were considered to be caused by the difference in the NDVI-surface reflectance relationship between Australia and the AERONET sites. Although assessment of the algorithm retrieving the $AOT_{original}$ was beyond the scope of this study, the future improvement of the $AOT_{original}$ will also improve the bias in AOT_{pure} and therefore in AOT_{merged}. In addition, the accumulation of AHI observation over a few years will improve the surface reflectance estimation by the accumulation of aerosol-free second minimum reflectances. Despite the Toyama site being within 7 km from the nearest coast, I did not recognize significant underestimation nor overestimation induced by difference in the aerosol model between land and ocean. In Kuching, some AOT_{merged} were missing even when the AOT_{pure} was retrieved [i.e., $(\text{AERONET}, AOT_{pure}) = (0.87, 0.68)$] because the number of effective AOT_{pure} around the AOT_{merged} pixel was less than 20% of the possible number of observations in the calculation domain. By contrast, the AOT_{merged} was retrieved even when the AOT_{pure} was missing [i.e., $(\text{AERONET}, AOT_{merge}) = (0.45, 0.33)$] in some cases because the AOT_{merged} can be retrieved when the number of the AOT_{pure} in the calculation domain was more than 20%. Some underestimations in the AOT_{pure} were improved in the AOT_{merge} at Ussuriysk because the AOT_{merged} was derived by using more accurate cloud-screened dataset of the AOT_{pure} than in the case of AOT_{pure}, which was derived from the $AOT_{original}$.

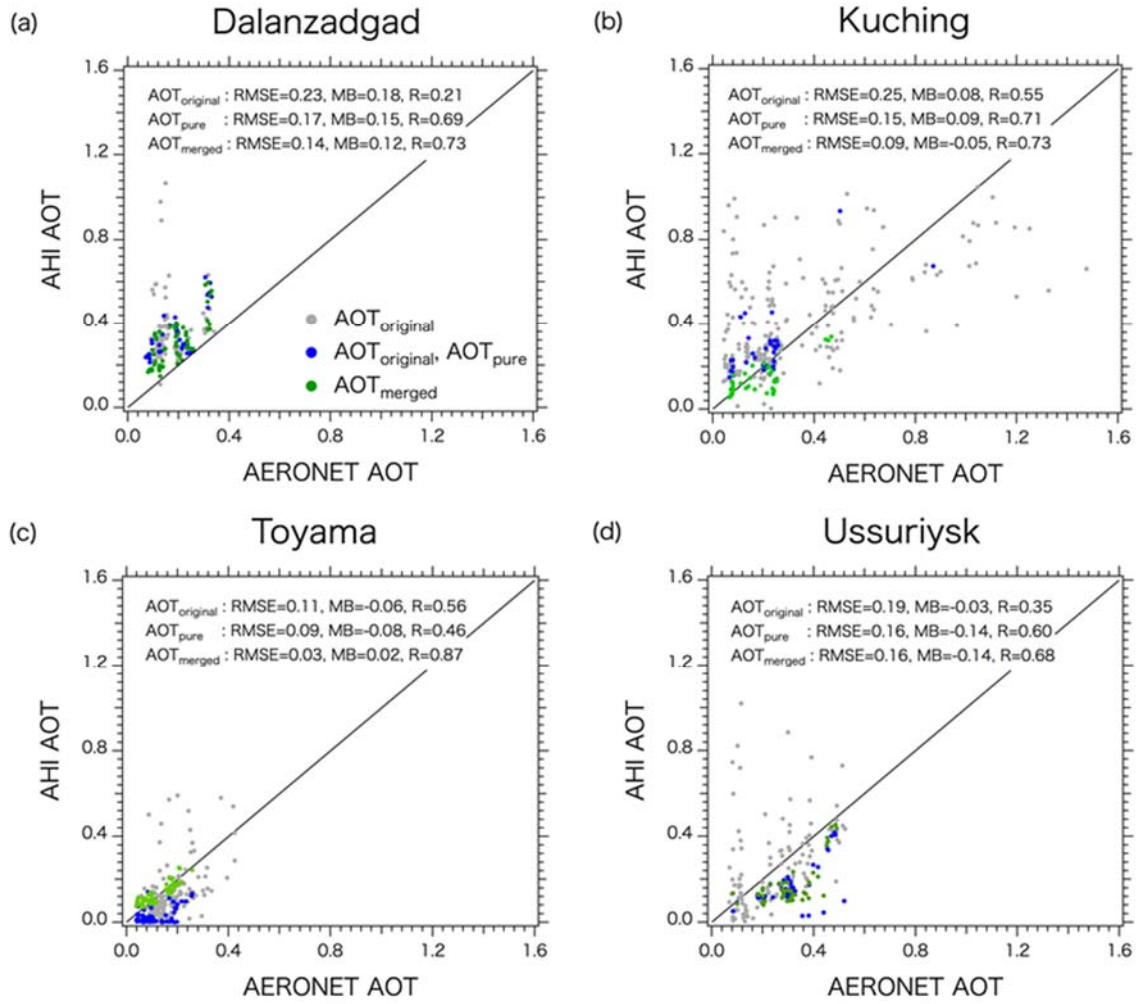

Figure 5.9. Comparison of AHI AOT to AERONET: (gray+blue) $AOT_{original}$, (blue) hourly combined AOT_{pure}, and (green) hourly combined AOT_{merged} at (a) Dalanzadgad, Mongolia, (b) Kuching, Malaysia, (c) Toyama, Japan, and (d) Ussuriysk, Russia.

The RMSE, mean bias (MB), mean normalized error (MNE), mean normalized bias (MNB), and correlation coefficients of all four sites are summarized in Table 5.2. The definitions of the statistic metrics are given in Appendix 5.1. Note that R_{All_data} is the simple correlation coefficient of all data with respect to the AERONET, and $R_{Average\_sites}$ is the average of the correlation coefficient at each site. $R_{Average\_sites}$ was derived to avoid taking the covariance between the sites because the source of the error differed according to the sites. Except for R_{All_data}, the AOT_{pure} and AOT_{merged} gave better statistical values than the $AOT_{original}$, showing better agreement with the AERONET and the improvement of the AOT estimation by the hourly combined algorithm. The RMSE of the $AOT_{original}$, AOT_{pure} and AOT_{merged} were 0.20,

0.14, and 0.11, respectively. The MNE also showed this tendency with 94% for the $AOT_{original}$, 73% for the AOT_{pure}, and 50% for the AOT_{merged}. The $AOT_{original}$ gave a positive bias of 0.032, and the main source of the error was considered to be cloud contamination. By contrast, AOT_{pure} and AOT_{merged} was negatively biased with -0.016 and -0.006, respectively, due to the successful elimination of cloud contamination and leaving the overestimation of surface reflectance and errors in the aerosol model setting. MNB was positive for AOT_{merged}, showing the influence of low AOT observation.

Table 5.2 RMSE, MB, MNE, MNB, and correlation coefficients (R_{All_sites} and $R_{Average\_sites}$) of $AOT_{original}$, AOT_{pure}, and AOT_{merged} with respect to AERONET.

	RMSE	MB	MNE [%]	MNB [%]	Correlation Coefficient	
					$R_{All\ data}$	$R_{Average\ sites}$
$AOT_{original}$	0.20	0.032	94.3	43.7	0.52	0.41
AOT_{pure}	0.14	-0.016	73.9	-3.6	0.52	0.62
AOT_{merged}	0.11	-0.006	50.0	16.5	0.44	0.76

R_{All_sites} is the simple correlation coefficient of all data. $R_{Average\_sites}$ is the mean of the correlation coefficient at each site. The definitions of the metrics are given in Appendix 5.1.

Figure 5.10 shows the scatter plot of derived AOTs with AERONET Maritime Aerosol Network. Maritime Aerosol Network is a component of the AERONET, which provides the AOT dataset from shipborne sun photometer measurements [Smirnov et al., 2003]. Cruises was selected that had more than one observation for each of the three AOTs ($AOT_{original}$, AOT_{pure}, and AOT_{merged}) during the operation period of Himawari-8. Two cruises satisfied these criteria: Okeanos Explorer Cruise 4 and 7. The number of the AOT_{pure} and AOT_{merged} was not high compared with that of $AOT_{original}$ because the ship track was over sunglint area (especially in Cruise 4) and the regions were covered by broken clouds at the time of observation, which was eliminated in the hourly combining procedure. Therefore, Fig. 5.10 should be regarded as a preliminary validation result with shipborne observations. Overall, the underestimation of $AOT_{original}$ seen in the ground-based sites was not recognized in Fig. 5.10, thereby showing the adequacy of the ocean algorithm. This result also confirmed that one of the major causes of underestimation in Fig. 5.9 was due to the overestimation of surface reflectance estimation and aerosol setting. The overestimation of $AOT_{original}$ could be related to not only cloud contamination but also white foams at high wind conditions, which was effectively eliminated in the AOT_{pure}, and therefore in the AOT_{merged}. The RMSE was 0.12 for $AOT_{original}$ and 0.06 for AOT_{pure} and AOT_{merged}, showing the improvement in the hourly combined algorithm.

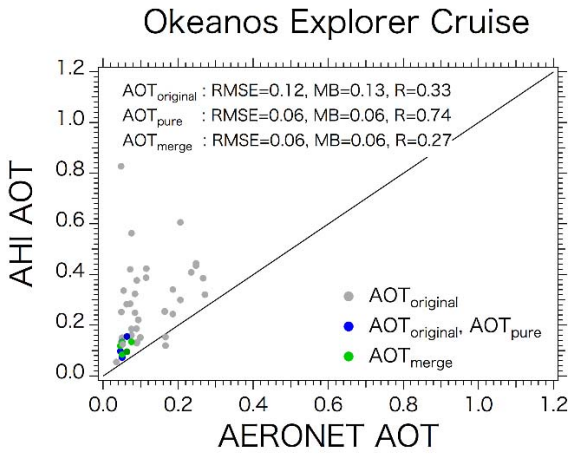

Figure 5.10. Comparison of AHI AOT with AERONET Maritime Aerosol Network: (gray + blue) $AOT_{original}$, (blue) hourly combined AOT_{pure}, and (green) hourly combined AOT_{merged} in Okeanos Explorer Cruise4 and Cruise7.

Lastly, shown in Fig. 5.11 is the full-disk image of the mean $AOT_{original}$, AOT_{pure} and AOT_{merged} on 27 April 2015 from 00:00 to 05:00 UTC. The aerosol transport from the continent over northern Japan seen in Fig. 5.1 is clearly shown in all AOTs ($AOT_{original}$, AOT_{pure}, and AOT_{merged}).The relatively high value (~1.0) of the $AOT_{original}$ can be recognized even over open ocean, indicating the presence of cloud contaminations. The AOT_{pure} and AOT_{merged} successfully eliminated these pixels and extracted uncontaminated aerosol pixels which reveals the distribution of aerosols more clearly. AHI's high frequent observation enabled the AOT_{merged} to reduce the missing AOT retrievals due to clouds and maximize the observation of aerosol during the day. Although the AOT_{pure} and AOT_{merge} seem similar in Fig. 5.11, the AOT_{merged} is actually smoother than the AOT_{pure} when analyzed in more detail (c.f. Fig. 5.8) and the number of the AOT_{merged} retrieval is larger than that of AOT_{pure}. Overall, the detailed AOT retrievals were successfully obtained that cover more than thousands of square kilometers from only 5 hours of observations, which were not achieved by the conventional geostationary nor polar-orbiting satellites.

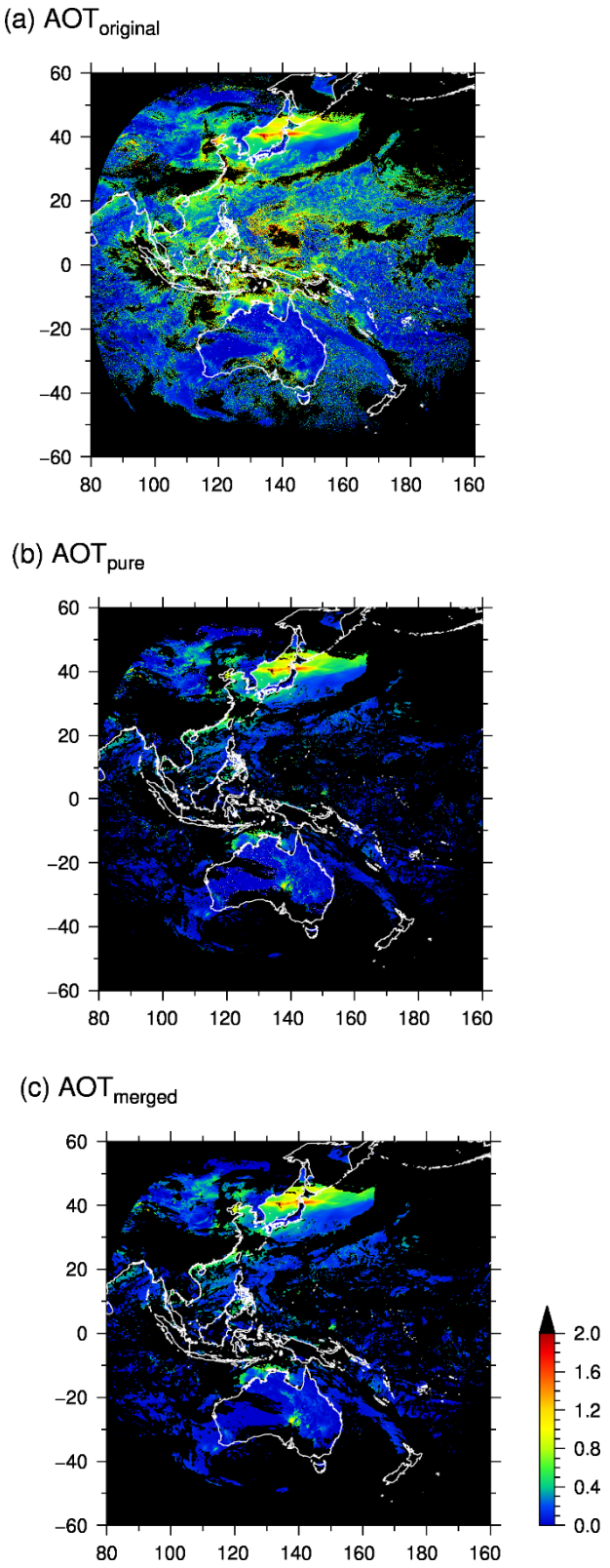

Figure 5.11. Full-disk image of mean (a) $AOT_{original}$, (b) AOT_{pure}, and (c) AOT_{merged} during 00:00 and 05:00 UTC on 27 April 2015.

5.6 Summary

In order to demonstrate a remote sensing scheme for distinguishing cloud and aerosol, the spatiotemporal variability of aerosol on a 10-minute and sub-kilometer scale was derived from observation for the first time by using AHI's ability to perform full-disk observation at every 10-minutes. As expected, the AOT variability was larger over land than over ocean: for example, the RMSD of AOT (between 0.4–0.5) within 10 minutes was 0.12 over ocean and 0.14 over land, which was equivalent to the spatial variability of approximately 8.0 km for ocean and 2.9 km for land (c.f. Section 5.2), indicating the spatial scale of aerosol variability over land being smaller than that over ocean. This appears to be a reasonable result given that more aerosol point sources are present over land than ocean and that sea salts from sea spray evaporation, a major oceanic aerosol type, spread widely and homogeneously over ocean.

The spatiotemporal variability of quality-controlled aerosols was found to be smaller than that of cloud-contaminated aerosols as demonstrated in Figs. 5.5 and 5.6. These results clearly indicated aerosol and cloud persisting different spatiotemporal variability characteristics, and that it would be effective to use these differences in discriminating them. These spatiotemporal variability characteristics were thus utilized to develop two types of AOTs from the snapshot estimates ($AOT_{original}$): AOT_{pure} and AOT_{merged}. AOT_{pure} is the subset of $AOT_{original}$ with strict cloud screening applied, excluded cloud-contaminated pixels that gave an exceptionally high AOTs compared to the surrounding and past aerosol fields. AOT_{merged} was derived by the spatial and temporal interpolation of AOT_{pure} and retrieved even at the missing pixels, giving maximum number of aerosol retrievals that can help better monitor aerosol distribution. Validated against AERONET ground-based observation, the RMSEs of the AOT_{pure} and AOT_{merged} improved to 0.14 and 0.11, respectively, compared with that of the $AOT_{original}$, which was 0.20.

The essence of the hourly combined algorithm is that it is a method to distinguish the substance of interest (in this case, aerosol) from another (in this case, cloud) using the spatiotemporal continuity of the variability characteristic of the substance of interest. The proposed method can also be applied to exclude contamination of unwanted entities from retrievals of other geophysical parameters, such as exclusion of aerosol contamination from cloud retrieval.

Appendix 5.1 Statistical Metrix

The followings are the definitions of the statistical metrics used in this study:

$$\text{Root Mean Square Error (RMSE)} = \sqrt{\frac{1}{N}\sum_{i=1}^{N}(AHI_i - ANET_i)^2}$$

$$\text{Mean Normalized Error (MNE)} = \frac{1}{N}\sum_{i=1}^{N}\left(\frac{|AHI_i - ANET_i|}{ANET_i}\right) \times 100\ [\%]$$

$$\text{Mean Normalized Bias (MNB)} = \frac{1}{N}\sum_{i=1}^{N}\left(\frac{AHI_i - ANET_i}{ANET_i}\right) \times 100\ [\%]$$

$$\text{Mean Bias (MB)} = \frac{1}{N}\sum_{i=1}^{N}(AHI_i - ANET_i)$$

$$\text{Correlation Coefficient } R_{All\_data}(\text{n} = \text{N}) = \frac{\sum_{i=1}^{n=N}(AHI_i - \overline{AHI})(ANET_i - \overline{ANET})}{\sqrt{\{\sum_{i=1}^{n=N}(AHI_i - \overline{AHI})^2\}\{\sum_{i=1}^{n=N}(ANET_i - \overline{ANET})^2\}}}$$

$$Correlation\ Coefficient\ R_{Average\_sites} = \frac{1}{4}\sum_{j=1}^{4} R_{All\_data}(n = M_j)$$

N is the total number of data for all sites, M_j is the total number of data at observation site j (j = 1: Dalanzadgad, 2: Kuching, 3: Toyama, 4: Ussuriysk). AHI_i and $ANET_i$ are the AHI and AERONET observation data, respectively. Variables with overbar are the mean of the data. R_{All_data} is a simple correlation coefficient of all data. $R_{Average\_sites}$ is the average of the correlation coefficient at each site. $R_{Average\_sites}$ was derived to avoid taking the covariance over different sites.

Chapter 6 General Conclusion

Cloud, precipitation and aerosols are the three principal particles in the atmosphere, playing as the key determinants of the radiation and water cycle on the Earth. Clouds are formed by the condensation of water vapor on to aerosols, growing through processes such as collision and coalescence of water droplets and aggregation of ice crystals, and dissipated by precipitation or evaporation. They often experience thermodynamic phase changes through melting and freezing processes, incorporating absorption or release of latent heat, affecting the degree of acceleration in its cloud development. These processes are complex and associated with non-linear interactions and feedbacks between the particles and ambient atmosphere, many of which are not yet well understood and hence are insufficiently represented in most of the climate models, leaving a potential source of uncertainties in the present and future climate projections. This calls for the need in observing four-dimensional distributions of atmospheric particles on a global scale, which is an ideal concept for monitoring their state and behavior in nature and untangle spatial- and temporal-dependent sophisticated interactions and feedbacks to improve our understanding in their physical processes governed. Toward this ultimate goal, employed in this dissertation study are the state-of-the-art satellite observations of hydrometeor and aerosol microphysical properties offered by the active and new generation geostationary satellites, which add the vertical and temporal dimensions in the atmospheric measurement, respectively. Special focus was brought to observationally analyze the spatial and temporal variabilities of the atmospheric particles in various scales - from a few minute and tens of kilometers to seasonal and global scales - using multiple satellite measurements, and develop the algorithms to discriminate different particles from the observational findings obtained. This study was comprised of three major parts: (1) the global and seasonal characteristic analysis of cloud phase and ice crystal types, namely cloud/hydrometeor particle type, by a Mie-scattering lidar (CALIOP) onboard CALIPSO satellite, (2) the algorithm development of particle type discrimination by combining a cloud profiling radar (CPR) onboard CloudSat satellite and the CALIOP classification, and (3) the algorithm development of aerosol-cloud discrimination using the difference in the spatiotemporal variability between cloud and aerosol fields by employing Himawari-8 multispectral imager.

6.1 Main Findings

The global and seasonal variability of cloud particle type was exploited using the new vertical dimension offered by the CALIPSO satellite (Chapter 3). The classification algorithm of cloud particle type by Yoshida et al. [2010] was revised to assign the original unknown type to appropriate ice crystal types and the analysis period was extended from three months to one entire year. The classified retrievals were compared with a different lidar algorithm (NASA VFM product), a different instrument (Aqua/MODIS) and environmental

conditions offered by a numerical model (ECMWF), to investigate the robustness and weakness of the algorithm, as well as to reveal the geographical and seasonal characteristics in relations to environmental conditions such as temperature and humidity that vary in the vertical direction. The strong temperature dependence of 2D-plate existence concentrating around -15 °C was found throughout the year, which infer the climatological nature of 2D-plate. Given that ice supersaturation is an important factor in cloud nucleation, the three-dimensional occurrence frequencies of ice clouds were compared with that of ice supersaturation derived from ECMWF. The results were in general agreement especially at temperatures below -20 °C with a strong correlation seen in their seasonal variations of their occurrence and cloud top temperature. A future work would include the evaluation of the ECMWF supersaturation using the CALIPSO particle type dataset and a possible employment of relative humidity to understand atmospheric condition in large-scale particle type formation. The cloud particle phase classification from this study was also in good correlation with NASA VFM and MODIS products, although uncertainties in the different algorithms (attributed to averaging of backscattering signals) and sensors (due to sensitivity and horizontal resolution/representativeness) was identified and evaluated quantitatively. Despite of satellite data often considered as a “truth” in model validations [e.g. Probst et al. 2012], the results shown here underscore the uncertainties within both the satellite algorithms and sensor sensitivities and that these uncertainties are actually larger in ice clouds than in water clouds, giving implication to the necessity of appropriate treatments of satellite retrieval uncertainties in future model evaluation studies.

Building upon the CALIPSO lidar classification above, the hydrometeor particle discrimination was further extended in the vertical direction by introducing CloudSat radar classification and combined the CALIPSO and CloudSat algorithms to complement each other to cover wider spectrum of hydrometeors (Chapter 4). To this end, the collocated measurement capability of the two sensors was exploited to relate the lidar-derived hydrometeor particle type to radar reflectivity and temperature. Given the significant sensitivity of radar reflectivity to particle size, the systematic multiple-dependence of particle size and temperature to particle type was revealed for the first time on the global scale, showing consistent characteristics indicated in the laboratory experiment from the global observation. To the basic principle of water droplets freezing to ice in temperature decrease, the results inferred the critical size for keeping its liquid state is dependent on temperature where at lower temperatures (e.g. ~-35°C), small particles are capable in freezing to ice, in contrast to the higher temperatures (e.g. ~-20°C) requiring the particles to grow larger before they start freezing. The findings from this analysis are then employed to propose CPR stand-alone and CPR-CALIOP synergy hydrometeor particle type discrimination. The algorithm presented here provides vertically resolved hydrometeor type profiles, employing the particle size - temperature dependency in the freezing process obtained above, which extends the capability of previous hydrometeor particle type algorithms that classified a phase per cloud layer [Wang et al., 2013] or within a cloud layer that uses solid thresholds of radar reflectivity and temperature [Ceccaldi et al., 2013]. The algorithm was then validated against the

independent observations of aircraft campaigns and discussed on the issues regarding the difference in the spatiotemporal representativeness of the space- and air-borne observations. Analyzing the hydrometeor classification before and after tilting CALIOP's viewing angle from 0.3° to 3.0° surprisingly showed a significant decrease in 2D-plate detection after the tilting. Inferred from this is the existence of 2D-plate in a significantly stable manner (i.e. its tumbling angle being within 3.0°) in the atmosphere. The missing 2D-plate in the lidar algorithm was complemented by the radar scheme introduced as the radar reflectivity field was not affected by the lidar tilting and the radar algorithm was trained by the lidar measurements before the tilting. Overall, the complementary nature of satellite measurements covers a wider spectrum in hydrometeor type classification, such as from relatively thick convection core and large anvil incorporated to the surrounding thin cirrus. To the total hydrometeor occurrence often derived in previous studies, the breakdown of each particle type was illustrated, offering a microphysical-based insight to the general idea of cloud occurrence. In contrast to the lidar algorithm used in Chapter 3, the synergy discrimination in Chapter 4 highlighted (1) the increase in the identification of the particle types that had already been classified (i.e., water, 3D-ice and 2D-plate) and (2) the identification of precipitations (including drizzle, rain and snow) introduced in the radar scheme, both of which was offered by the hydrometeor detection of the CPR in the regions where lidar was attenuated, and (3) the identification of mixed-phase and bi-modal types (such as the combination of liquid cloud and precipitation), which are also the new types revealed by employing the different sensitivity characteristics between the lidar and radar.

In principle, the discrimination of different atmospheric particles is also possible by using their different behaviors in time and space. Particularly, the discrimination of aerosol and cloud, which is essential in understanding their interactions but has been a common issue in aerosol estimation from conventional passive instrument, is expected to be improved using the significant difference in their spatiotemporal variabilities. For this purpose, the high-frequency measurement capability of Himawari-8 was employed to develop an algorithm to discriminate aerosols from clouds by quantifying their spatiotemporal variability characteristics (Chapter 5). Here, the spatiotemporal variability of aerosol was first derived in 10-minute and a few kilometers scale by the frequent observation offered from Himawari-8 satellite. These variabilities were quantitively represented in aerosol optical thickness and evidently indicated the spatial scale of aerosol over land being smaller than that over ocean, which was reasonable considering that more ubiquitous aerosol point source over land and sea salts from sea spray evaporation distributes homogeneously over open ocean. These characteristics were then utilized to develop an hourly algorithm that produces two sets of AOTs: AOT_{pure}, derived by the application of strict cloud screening to the original retrieval ($AOT_{original}$), and AOT_{merged}, derived from spatial and temporal interpolations of AOT_{pure}. The AOTs thus obtained from the hourly algorithm were validated against measurements from the aerosol robotic network (AERONET). The root-mean square errors (RMSEs) of the AOT_{pure} and AOT_{merged} products were 0.14 and 0.11, respectively, providing improvement over an RMSE of 0.20 for $AOT_{original}$

and indicating successful elimination of cloud-contaminated retrievals. A particular example on 27 April 2015 was shown where the detailed aerosol transport from the continent stretching over northern Japan was demonstrated only from 5-hours of observation data, covering almost all regions over Asia and Oceania. The present scheme is distinctive from the past in that it incorporates the 10-minute temporal observation information within the algorithm to evaluate the aerosol spatiotemporal variability to effectively improve the aerosol property estimates. The essence of the hourly combined algorithm developed here is that it is a scheme to discriminate the substance of interest (in this case, aerosol) from another (in this case, cloud) by considering the spatiotemporal continuity of the substance of interest. Hence the proposed method can be applied to exclude aerosol contamination from cloud retrievals or other combination of geophysical parameters.

6.2 Implications to Climate Modelling

The accumulated measurements of CloudSat and CALIPSO over a decade have been used to evaluate model performance and attempted to constrain model assumptions [e.g. Cesana and Chepfer, 2013; Kay et al., 2018]. The unrealistic representations of cloud-phase, in particular, have been pointed out as a common remaining uncertainty in climate models that influence cloud feedbacks simulated in climate models [Storelvmo et al., 2015; Tan et al., 2016], which is considered to partly attribute to the long-standing surface shortwave radiation bias over the Southern Ocean [Trenberth and Fasullo et al., 2009; Kay et al., 2016b]. The work by McCoy et al. [2015] is known for the comprehensive study that evaluated the cloud phase dependence on temperature in 19 Coupled Model Intercomparison Project Phase 5 (CFMIP5) climate models against the CALIOP phase measurement obtained from the NASA VFM product. Shown in Fig. 6.1a is a figure extracted from McCoy et al. [2015], indicating the liquid condensate fraction as a function of temperature, with the observation uncertainty in blue area suggested from this study as explained below. They found a substantial diversity in the liquid condensate fraction among the models and the freezing temperature (at which liquid and ice are equally mixed) ranged as much as 40 K, generally underestimating liquid clouds and producing ice clouds instead. While McCoy et al. [2015] demonstrated a cloud phase diagnosis for climate models, the following two issues are yet to be addressed in their model-satellite comparison:

- employment of a satellite simulator to the models for a more direct comparison with the satellite measurements
- consideration of the uncertainties in the satellite retrievals

Regarding the first point, the model evaluation in McCoy et al. [2015] using the CALIOP measurement was still an apples-to-oranges comparison where the liquid condensation fractions of the models were derived on mass-basis (i.e. liquid mass versus ice mass) whereas that of the measurement was derived on

frequency-basis (i.e. liquid frequency versus ice frequency). Further, the model results were based on all clouds in all pressure level and limited to 30-80°S during 1850-1900 historical runs [McCoy et al., 2015] whereas CALIPSO measurements were limited to cloud-tops from the global observation for one year of 2008 [Hu et al., 2010]. For a more apples-to-apples comparison, incorporated in recent model evaluation studies are the satellite simulators, which simulate what a satellite would have measured if it flew over a modelled atmosphere [Matricardi et al. 2004; Bauer et al., 2006; Voors et al., 2007; Masunaga et al., 2010; Bodas-Salcedo and Webb, 2011; Hashino et al. 2013; Matsui et al. 2014]. Using such dedicated tools would derive the liquid/ice occurrence frequency from climate models and thus can be compared to CALIOP in a "scare-aware and definition-aware evaluation" [Kay et al., 2018] where the spatiotemporal scale and definition of the microphysical properties of the measurements and models are equivalent. The works by Cesana and Chepfer [2013] and Cesana et al. [2015] showed that the liquid condensate fraction was found to generally increase when the satellite simulators were applied to two climate models of Institut Pierre-Simon Laplace (IPSL) and Centre National de Recherches Météorologiques (CNRM). Cesana et al. [2015] concluded that approximately -6 to -10 K transition of the freezing temperature were identified when the simulator was applied, implicating that the freezing temperature is sensitive to the observation sampling of the instruments and utilizing satellite simulators would be necessary for an accurate evaluation of the phase partitioning in models.

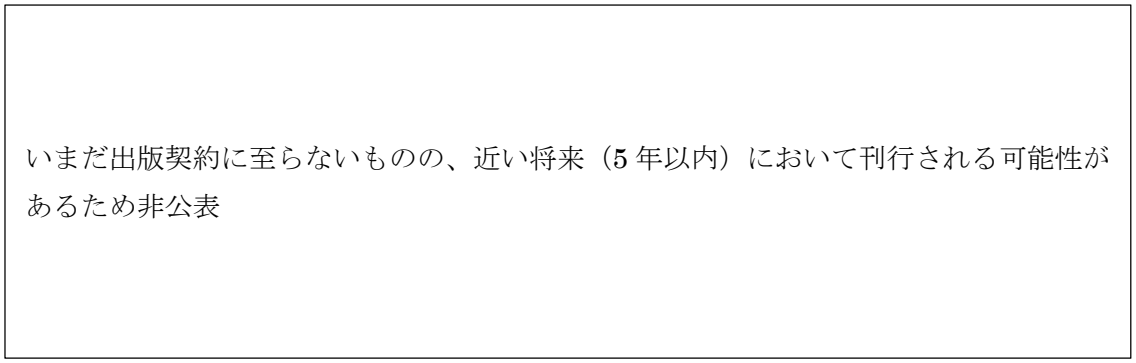

Figure 6.1 Temperature dependence of cloud phase, shown in the liquid condensate fraction as a function of temperature. (a) Climate model simulations from 19 CFMIP5 models, and (b) CALIOP and CloudSat/CALIPSO synergy observations obtained in this study. CALIOP observations from Hu et al. [2010] are shown in the red dashed line in both figures. Fig. 6.1a is extracted from McCoy et al. [2015] with the blue area overlaid, schematically illustrating observation uncertainty represented from Fig. 6.1b. Gray dashed vertical lines indicate the 0°C and -40°C temperatures.

To address the second point, a preliminary result on the temperature dependence of cloud phase obtained from the dataset developed in this study is shown in Fig. 6.1b. The liquid condensate fractions were derived

from the CALIPSO algorithm (in Chapter 3) and CloudSat/CALIPSO synergy algorithm (in Chapter 4) using three years of data in 2007-2009. The gray dashed vertical lines indicate 0°C and -40°C as a guide to freezing/melting and homogeneous/heterogeneous freezing transition temperatures, respectively. In the figure, the observation uncertainty is schematically illustrated in the blue area, taking into account the difference between the CALIPSO and synergy estimations. It is noteworthy to mention that the observation uncertainty attributed to the differences in the CALIPSO algorithms (i.e. Hu et al. [2009], Yoshida et al. [2010] and Cesana and Chepfer [2013]) shown in Fig. 6 of Cesana et al. [2016] is appeared to fall within the observational uncertainty range in Fig. 6.1b. Overall, the liquid fraction obtained from this study was lower than that served in Hu et al. [2010] (Fig. 6.1b). The reason for this is that the liquid fraction in Hu et al. [2010] was derived from topmost cloud pixels whereas this study was derived from the pixels throughout the cloud layers, taking into account the ice layer especially under the liquid-topped clouds, leading to lower the liquid fraction.

In Fig. 6.1a, the observational uncertainty range obtained in Fig. 6.1b was overlaid to the model simulations, clearly showing the narrower range of the uncertainty in the observations than that among the models. Surprisingly, the liquid fraction of the multimodel mean, shown in the gray dashed line, was generally larger than that of the observation in this study. From the discussion on the first point, the liquid fraction detected to be water increases when the satellite simulators were applied to the models [Cesana and Chepfer, 2013; Cesana et al. 2015]. Therefore, the multimodel mean is expected to become even larger when satellite simulators were applied, implying a possible overestimation of liquid phase in the models, rather than the underestimation that has been understood before. One further implication here is that if the model phase representation was tuned in a manner to decrease the liquid fraction, the melting process from ice to liquid is expected to accelerate in a warmed climate simulation, inducing stronger negative phase feedback and leading to decrease the climate sensitivity [Storelvmo et al. 2015]. Another implication is that if the liquid fraction in the model was optimized to decrease, the excessive absorption of the shortwave radiation over the Southern Ocean commonly found in climate models would be increased even more. Hence this may suggest that the bias was resulted from the unrealistic representation in the cloud nucleation (i.e. cloud frequency) or the cloud microphysical properties (such as mass concentration and size distribution) rather than the phase representation in the models.

The hydrometeor particle type classification in this study is thus expected to offer an observational constraint for the models based on a more comprehensive measurement of clouds, serving as an observational source to revisit the implication of the cloud phase feedback and climate sensitivity investigated in the previous studies [Cheng et al., 2012; Cesana et al., 2012, 2015; Cesana and Chepfer, 2013; Komurcu et al., 2014; Kay et al., 2016a; McCoy et al., 2015; Tan et al., 2016]. Although the recent studies on cloud phase representativeness are focused on the temperature-based analysis as shown in the

discussion above, the findings in Chapter 4 also inferred the multivariable dependence of cloud phase not only on the temperature, but also on particle size in the freezing process. Therefore, extending the particle size and temperature discussion to the climate model simulation similar to that demonstrated in Chapter 4 is expected to give a more microphysical-based evaluation of the freezing process in the models.

6.3 Future Studies

Building upon the atmospheric particle algorithms, the future work will include (1) further validation of the retrieval algorithms, (2) application of the algorithms to the future satellites, and (3) process-oriented analysis by the synergetic analysis of the geostationary and polar-orbiting satellites. The estimated microphysical properties will be carefully validated against various independent measurements of in-situ aircraft observations and remote sensing ground-based networks and satellite observations. In-situ measurements by optical particle counters and cloud/precipitation probes, for example, would be the most direct method to validate the aerosol and hydrometeor estimations. The precipitation radars onboard the TRMM and GPM Core Observatory are the two satellite missions that provide the measurements especially for the evaluation of rain and snow retrievals introduced in this study. Ground-based sun photometer sites of SKYNET would be another observation network for aerosol validation in addition to the AERONET network used in Chapter 3. Given that terminal velocity differs according to hydrometeor particle types [Locatelli and Hobbs, 1974; Mitchell, 1995], ground-based Doppler radars would be a powerful measurement to not only validate the current algorithms but also to employ Doppler velocity for an more advanced algorithm, which can be applied as an algorithm basis for the future mission of Earth Clouds, Aerosols and Radiation Explorer (EarthCARE), which loads a Doppler cloud profiling radar and an atmospheric lidar as a “successor” of CloudSat and CALIPSO. The combination of CloudSat/CALIPSO and EarthCARE observation is expected to offer the three-dimensional long-term dataset towards climatological analysis on hydrometeor particle types. The application of the Himawari-8 hourly-combined aerosol algorithm to the next-generation geostationary satellites developed in the international meteorological agencies (e.g. GOES-R, MTG) would extend the analysis region from Asia-Oceana to the globe. This global geostationary satellite observations would offer continuous matchup measurement with polar-orbiting satellites. In particular, the highly accurate global aerosol dataset retrieved using the temporal information is expected to improve the aerosol contamination issue in CALIOP cloud detection discussed in Chapter 3. Furthermore, the uniqueness of the proposed aerosol estimates is in the capability to derive aerosol optical properties (i.e. particularly demonstrated as AOT_{merge} in this study) even when a pixel of interest was covered over cloud. The synergy analysis of the geostationary satellites giving horizontal aerosol property estimates and Cloudsat/CALIPSO giving vertical particle type profiles is expected to further dig into the processes governing aerosol, cloud and precipitation. For example, a study by Luo et al. [2008] served a cloud-top buoyancy estimation using the temperature difference between the ambient and

cloud-top observed by the MODIS imager. This buoyancy estimation can be applied to the Himawari-8 imager and, owing to its high-frequency observations, to track a cloud motion and pin down on which stage of its life cycle the cloud is experiencing. Combining with the CloudSat and CALIPSO, this can be linked to the vertical particle type transitions over their life time and how they are affected by aerosol perturbation for better estimates of their impacts on radiation field. The further multi-platform satellite analysis of the atmospheric particles using the temporal and vertical information explored in this study is expected to contribute to deepen our understanding in aerosol-cloud-precipitation interactions and processes that govern the microphysical structures of atmospheric particles that vary in time and space.

References

Albrecht, B. A., 1989: Aerosols, cloud microphysics, and fractional cloudiness, *Science*, 245, 1227–1230, https://doi.org/10.1126/science.245.4923.1227

Ackerman, A. S., M. P. Kirkpatrck, D. E. Stevens, and O. B. Toon, 2004: The impact of humidity above stratiform clouds on indirect aerosol climate forcing, *Nature*, 432, 1014–1017, https://doi.org/10.1038/nature03174

Awaji, T., M. Kamaji, M. Ikeda, and Y. Ishida, 2009: Data Assimilation—Innovation to Combine Observation and Experiment With Model, Kyoto, Japan: Kyoto Univ. Press. (in Japanese)

Bauer, P., E. Moreau, F. Chevallier, and U. O'Keefe, 2006: Multiple-scattering microwave radiative transfer for data assimilation applications, *Quart. J. Roy. Meteor. Soc*., 132, 1259–1281, https://doi.org/10.1256/qj.05.153

Baum, B. A., D. P. Kratz, P. Yang, S. C. Ou, Y. Hu, P. F. Soulen, and S. C. Tsay, 2000: Remote sensing of cloud properties using MODIS airborne simulator imagery during SUCCESS: 1. Data and models, *J. Geophys. Res.*, 105, 11,767–11,780. https://doi.org/10.1029/1999JD901089

Beneditte, A. 2003: CloudSat AN–ECMWF Ancillary Data Interface Control Document.

Bergeron, T., 1935: On the physics of cloud and precipitation, *Proc. of the 5th General Assembly of the UGGI*, 2, 156–175, UGGI, Lisbon.

Bessho, K., K. Date, M. Hayashi, A. Ikeda, T. Imai, H. Inoue, Y. Kumagai, T. Miyakawa, H. Murata, T. Ohno, A. Okuyama, R. Oyama, Y. Sasaki, Y. Shimazu, K. Shimoji, Y. Sumida, M. Suzuki, H. Taniguchi, H. Tsuchiyama, D. Uesawa, H. Yokota, and R. Yoshida, 2016: An introduction to Himawari-8/9—Japan's new-generation geostationary meteorological satellites, *J. Meteorol. Soc. Jpn*., 94(2), https://doi.org/10.2151/jmsj.2016-009

Bigg, E. K. 1953: The formation of atmospheric ice crystals by the freezing of droplets, *Quart. J. Roy. Meteor. Soc*., 79, 510-519, https://doi.org/10.1002/qj.49707934207

Bodas-Salcedo, A., M. J. Webb, S. Bony, H. Chepfer, J. Dufresne, S. A. Klein, Y. Zhang, R. Marchand, J. M. Haynes, R. Pincus, and V. O. John, 2011: COSP: Satellite simulation software for model assessment, *Bull. Amer. Meteor. Soc*., 92, 1023–1043, https://doi.org/10.1175/2011BAMS2856.1

Bréon, F., and B. Dubrulle, 2004: Horizontally Oriented Plates in Clouds, *J. Atmos. Sci.*, 61, 2888–2898, https://doi.org/10.1175/JAS-3309.1.

Ceccaldi, M., J. Delanoë, R. J. Hogan, N. L. Pounder, A. Protat, and J. Pelon, 2013: From CloudSat-CALIPSO to EarthCare: Evolution of the DARDAR cloud classification and its comparison to airborne radar-lidar observations., *J. Geophys. Res.*, 118, 7962–7981, https://doi.org/10.1002/jgrd.50579

Cesana, G., and H. Chepfer, 2013: Evaluation of the cloud thermodynamic phase in a climate model using CALIPSO‐GOCCP, *J. Geophys. Res.*, 118, 7922–7937, https;//doi.org/10.1002/jgrd.50376

Cesana, G., J. E. Kay, H. Chepfer, J. M. English, and G. DeBoer, 2012: Ubiquitous low-level liquid-containing Arctic clouds: New observations and climate model constraints from CALIPSO-GOCCP, *Geophys. Res. Lett.*, 39, L20804, https://doi.org/10.1029/2012GL053385

Cesana, G., D. E. Waliser, X. Jiang, and J. L. F. Li, 2015: Multimodel evaluation of cloud phase transition using satellite and reanalysis data, *J. Geophys. Res.*, 120, 7871–7892, https://doi.org/10.1002/2014JD022932

Cesana, G., H. Chepfer, D. Winker, B. Getzewich, X. Cai, O. Jourdan, G. Mioche, H. Okamoto, Y. Hagihara, V. Noel, and M. Reverdy, 2016: Using in situ airborne measurements to evaluate three cloud phase products derived from CALIPSO, *J. Geophys. Res.*, 121, 5788–5808, https://doi.org/10.1002/2015JD024334

Cheng, A., K.-M. Xu, Y. Hu, and S. Kato, 2012: Impact of a cloud thermodynamic phase parameterization based on CALIPSO observations on climate simulation, *J. Geophys. Res.*, 117, D09103, https://doi.org/10.1029/2011JD017263

Chepfer, H., P. Goloub, J. Riedi, J. F. De Haan, J. W. Hovenier, and P. H. Flamant, 2001: Ice crystal shapes in cirrus clouds derived from POLDER/ADEOS-1, *J. Geophys. Res.*, 106(D8), 7955–7966, https://doi.org/10.1029/2000JD900285

Christensen, M. W., K. Suzuki, B. Zambri, and G. L. Stephens, 2014: Ship track observations of a reduced shortwave aerosol indirect effect in mixed‐phase clouds, *Geophys. Res. Lett.*, 41, 6970–6977, https://doi.org/10.1002/2014GL061320

CloudSat Project, 2008: CloudSat Standard Data Products Handbook, Colorado State University.

Dubovik, O., B. Holben, T. F. Eck, A. Smirnov, Y. J. Kaufman, M. D. King, D. Tanré, and I. Slutsker, 2002: Variability of Absorption and Optical Properties of Key Aerosol Types Observed in Worldwide Locations, *J. Atmos. Sci.*, 59, 590–608, https://doi.org/10.1175/1520-0469(2002)059<0590:VOAAOP>2.0.CO;2

Dubovik, O., Herman, M., Holdak, A., Lapyonok, T., Tanré, D., Deuzé, J. L., Ducos, F., Sinyuk, A., and Lopatin, A., 2011: Statistically optimized inversion algorithm for enhanced retrieval of aerosol properties from spectral multi-angle polarimetric satellite observations, *Atmos. Meas. Tech.*, 4, 975-1018, https://doi.org/10.5194/amt-4-975-2011

Eichler, H., A. Ehrlich, M. Wendisch, G. Mioche, J.-F. Gayet, M. Wirth, C. Emde, and A. Minikin, 2009: Influence of ice crystal shape on retrieval of cirrus optical thickness and effective radius: A case study, *J. Geophys. Res.*, 114, D19203, https://doi.org/10.1029/2009JD012215

Engvall, A.-C., R. Krejci, J. Ström, R. Treffeisen, R. Scheele, O. Hermansen, and J. Paatero, 2008: Changes in aerosol properties during spring-summer period in the Arctic tropospheric aerosol during late spring and summer, *Tellus*, 60B, 392–404, https://doi.org/10.1111/j.1600-0889.2008.00348.x

Eyre, J. R., Kelly, G. A., McNally, A. P., Andersson, E., and Persson, A., 1993: Assimilation of TOVS radiance information through one-dimensional variational analysis, *Quart. J. Roy. Meteor. Soc.*, 119(514), 1427–1463, https://doi.org/10.1002/qj.49711951411

Findeisen, W., 1938: Die Kolloidmeteorologischen Vorgange bei der Niederschlasbildung (Collodial meteorological processes in the formation of precipitation), *Meteorol. Z.*, 55, 121–133.

Fukuda, S., T. Nakajima, H. Takenaka, A. Higurashi, N. Kikuchi, T. Y. Nakajima, and H. Ishida, 2013: New approaches to removing cloud shadows and evaluating the 380 nm surface reflectance for improved aerosol optical thickness retrievals from the GOSAT/TANSO‐Cloud and Aerosol Imager, *J. Geophys. Res.*, 118, 13,520–13,531, https://doi.org/10.1002/2013JD020090

Goloub, P., M. Herman, H. Chepfer, J. Riedi, G. Brogniez, P. Couvert, and G. Se'ze, 2000: Cloud thermodynamical phase classification from the POLDER spaceborne instrument, *J. Geophys. Res.*, 105(D11), 14,747–14,759, https://doi.org/10.1029/1999JD901183

Gordon, H. R., and M. H. Wang, 1994: Retrieval of water-leaving radiance and aerosol optical thickness over the oceans with SeaWiFS: a preliminary algorithm, *Appl. Optics*, 33-3, 443-452, https://doi.org/10.1364/AO.33.000443

Hagihara, Y., H. Okamoto, and R. Yoshida, 2010: Development of a combined CloudSat-CALIPSO cloud mask to show global cloud distribution, *J. Geophys. Res.*, 115, D00h33, https://doi.org/10.1029/2009JD012344

Hashino, T., M. Satoh, Y. Hagihara, T. Kubota, T. Matsui, T. Nasuno, and H. Okamoto, 2013: Evaluating cloud microphysics from NICAM against CloudSat and CALIPSO, *J. Geophys. Res.*, 118, 1–20, https://doi.org/10.1002/jgrd.50564

Haynes, J. M., T. S. L'Ecuyer, G. L. Stephens, S. D. Miller, C. Mitrescu, M. B. Wood, and S. Tanelli, 2009: Rainfall retrieval over the ocean with spaceborne W-band radar, *J. Geophys. Res.*, 114, D00A22, https://doi.org/10.1029/2008JD009973

Higurashi, A., and T. Nakajima, 1998: Development of a two-channel aerosol retrieval algorithm on a global scale using NOAA AVHRR, *J. Atmos. Sci.*, 56, 7, 924–941, https://doi.org/10.1175/1520-0469(1999)056<0924:DOATCA>2.0.CO;2

Hirakata, M., H. Okamoto, Y. Hagihara, T. Hayasaka, and R. Oki, 2014: Comparison of Global and Seasonal Characteristics of Cloud Phase and Horizontal Ice Plates Derived from CALIPSO with MODIS and ECMWF, *J. Atmos. Oceanic Technol.*, 31, 2114–2130, https://doi.org/10.1175/JTECH-D-13-00245.1

Holben B.N., T.F.Eck, I.Slutsker, D.Tanre, J.P.Buis, A.Setzer, E.Vermote, J.A.Reagan, Y.Kaufman, T.Nakajima, F.Lavenu, I.Jankowiak, and A.Smirnov, 1998: AERONET - A federated instrument network and data archive for aerosol characterization, *Remote Sens. Environ.*, 66, 1-16, https://doi.org/10.1016/S0034-4257(98)00031-5

Holz, R. E., S. A. Ackerman, F. W. Nagle, R. Frey, S. Dutcher, R. E. Kuehn, M. A. Vaughan, and B. Baum, 2008: Global Moderate Resolution Imaging Spectroradiometer (MODIS) cloud detection and height evaluation using CALIOP, *J. Geophys. Res.*, 113, D00A19, https://doi.org/10.1029/2008JD009837

Hunt, W. H., D. M. Winker, M. A. Vaughan, K. A. Powell, P. L. Lucker, and C. Weimer, 2009: CALIPSO Lidar Description and Performance Assessment, *J. Atmos. Oceanic Technol.*, 26, 1214–1228, https://dx.doi.org/10.1175/2009JTECHA1223.1

Hsu, N. C., S. C. Tsay, M. D. King, and J. R. Herman, 2004: Aerosol properties over bright-reflecting source regions, *IEEE Trans. Geosci. Remote Sens.*, 42(3), 557–569, https://doi.org/10.1109/TGRS.2004.824067

Hsu, N. C., S. C. Tsay, M. D. King, and J. R. Herman, 2006: Deep Blue retrievals of Asian aerosol properties during ACE-Asia, *IEEE Trans. Geosci. Remote Sens.*, 44(11), 3180–3195, https://doi.org/10.1109/TGRS.2006.879540

Hu, Y., D. Winker, M. Vaughan, B. Lin, A. Omar, C. Trepte, D. Flittner, P. Yang, S.L. Nasiri, B. Baum, R. Holz, W. Sun, Z. Liu, Z. Wang, S. Young, K. Stamnes, J. Huang, and R. Kuehn, 2009: CALIPSO/CALIOP Cloud Phase Discrimination Algorithm, *J. Atmos. Oceanic Technol.*, 26, 2293–2309, https://doi.org/10.1175/2009JTECHA1280.1

Hu, Y., S. Rodier, K. Xu, W. Sun, J. Huang, B. Lin, P. Zhai, and D. Josset, 2010: Occurrence, liquid water content, and fraction of supercooled water clouds from combined CALIOP/IIR/MODIS measurements, *J. Geophys. Res.*, 115, D00H34, https://doi.org/10.1029/2009JD012384

Hunt, W. H., D. M. Winker, M. A. Vaughan, K. A. Powell, P. L. Lucker, and C. Weimer, 2009: CALIPSO Lidar Description and Performance Assessment, *J. Atmos. Oceanic Technol.*, 26, 1214-1228, https://doi.org/10.1175/2009JTECHA1223.1

Ishida, H., and T. Y. Nakajima, 2009: Development of an unbiased cloud detection algorithm for a spaceborne multispectral imager, *J. Geophys. Res.*, 114, D07206, https://doi.org/10.1029/2008JD010710

Ishida, H., T. Y. Nakajima, T. Yokota, N. Kikuchi, and H. Watanabe, 2011: Investigation of GOSAT TANSO-CAI cloud screening ability through an inter-satellite comparison, *J. Appl. Meteor. Climatol.*, 50, 1571-1586, https://doi.org/10.1175/2011JAMC2672.1

Kaufman, Y. J., D. Tanré, L. A. Remer, E. F. Vermote, A. Chu, and B. N. Holben, 1997: Operational remote sensing of tropospheric aerosol over land from EOS moderate resolution imaging spectroradiometer, *J. Geophys. Res.*, 102(D14), 17051–17067, https://doi.org/10.1029/96JD03988

Kay, J. E., L. Bourdages, N. B. Miller, A. Morrison, V. Yettella, H. Chepfer, and B. Eaton, 2016a: Evaluating and improving cloud phase in the Community Atmosphere Model version 5 using spaceborne lidar observations, *J. Geophys. Res.*, 121, 4162–4176, https://doi.org/10.1002/2015JD024699

Kay, J.E., C. Wall, V. Yettella, B. Medeiros, C. Hannay, P. Caldwell, and C. Bitz, 2016b: Global Climate Impacts of Fixing the Southern Ocean Shortwave Radiation Bias in the Community Earth System Model (CESM), *J. Climate*, 29, 4617–4636, https://doi.org/10.1175/JCLI-D-15-0358.1

Kay, J. E., T. L'Ecuyer, A. Pendergrass, H. Chepfer, R. Guzman, and V. Yettella, 2018: Scale‐aware and definition‐aware evaluation of modeled near‐surface precipitation frequency using CloudSat observations, *J. Geophys. Res.*, 123, 4294–4309, https://doi.org/10.1002/2017JD028213

Kikuchi, M., H. Okamoto, K. Sato, K. Suzuki, G. Cesana, Y. Hagihara, N. Takahashi, T. Hayasaka, and R. Oki, 2017: Development of algorithm for discriminating hydrometeor particle types with a synergistic Use of CloudSat and CALIPSO, *J. Geophys. Res.*, 122, 11,022–11,044. https://doi.org/10.1002/2017JD027113

Kikuchi, M., H. Murakami, K. Suzuki, T. M. Nagao, and A. Higurashi, 2018: Improved Hourly Estimates of Aerosol Optical Thickness Using Spatiotemporal Variability Derived From Himawari-8 Geostationary Satellite, *IEEE Trans. Geosci. Remote Sens.*, 56 (6), 3442-3455, https://doi.org/10.1109/TGRS.2018.2800060

King, M. D., S. Platnick, P. Yang, G. T. Arnold, M. A. Gray, J. C. Riedi, S. A. Ackerman, and K. N. Liou, 2004: Remote sensing of liquid water and ice cloud optical thickness and effective radius in the Arctic: Application of airborne multispectral MAS data, *J. Atmos. Oceanic Technol.*, 21, 857–875, https://doi.org/10.1175/1520-0426(2004)021<0857:RSOLWA>2.0.CO;2

Komurcu, M., T. Storelvmo, I. Tan, U. Lohmann, Y. Yun, J. E. Penner, Y. Wang, X. Liu, and T. Takemura, 2014: Intercomparison of the cloud water phase among global climate models, *J. Geophys. Res.*, 119, 3372–3400, https://doi.org/10.1002/2013JD021119

Kummerow, C., W. S. Olson, and L. Giglio, 1996: A Simplified Scheme for Obtaining Precipitation and Vertical Hydrometeor Profiles from passive Microwave Sensors, *IEEE Trans. Geosci. Remote Sens.,* 34, 1213-32, https://doi.org/10.1109/36.536538

Kummerow, C., Y. Hongb, W. S. Olsonc, S. Yangc, R. F. Adlerd, J. McCollume, R. Ferraroe, G. Pettyf, D. B. Shina, and T. T. Wilheitg, 2001: The evolution of the Goddard Profiling Algorithm (GPROF) for rainfall estimation from passive microwave sensors, *J. Appl. Meteor.*, 40, 1801-1820,https://doi.org/10.1175/1520-0450(2001)040<1801:TEOTGP>2.0.CO;2

Lawson, P. R., S. Woods, and H. Morrison, 2015: The microphysics of ice and precipitation development in tropical cumulus clouds, *J. Atmos. Sci.*, 72, 2429-2445, https://doi.org/10.1175/JAS-D-14-0274.1

Leon, D. C., Z. Wang, and D. Liu, 2008: Climatology of drizzle in marine boundary layer clouds based on 1 year of data from CloudSat and CALIPSO, *J. Geophys. Res.*, 113, D00A14, https://doi.org/10.1029/2008JD009835

Levy, R. C., L. A. Remer, D. Tanré, Y. J. Kaufman, C. Ichoku, B. N. Holben, J. M. Livingston, P. B. Russell, and H. Maring, 2003: Evaluation of the Moderate-Resolution Imaging Spectroradiometer (MODIS) retrievals of dust aerosol over the ocean during PRIDE, *J. Geophys. Res.*, 108, D19, 8594, https://doi.org/10.1029/2002JD002460

Libbrecht, K. L., 2005: The physics of snow crystals, Reports on Progress in Physics, 68, 855-895, *Institute of Physics Publishing*, https://doi.org/10.1088/0034-4885/68/4/R03

Liu, G., 2008: Deriving snow cloud characteristics from CloudSat observations, *J. Geophys. Res.*, 113, D00A09, https://doi.org/10.1029/2007JD009766

Liu, G., and J. A. Curry, 1992: Retrieval of precipitation from satellite microwave measurements using both emission and scattering, *J. Geophys. Res.*, 97, 9959–9974, https://doi.org/10.1029/92JD00289

Liu, G., and J. A. Curry, 1996: Large-scale cloud features during January 1993 in the North Atlantic Ocean as determined from SSM/I and SSM/T2 observations, *J. Geophys. Res.*, 101, D3, 7019–7032, https://doi.org/10.1029/95JD03859

Locatelli, J. D., and P. V. Hobbs, 1974: Fall speeds and masses of solid precipitation particles, *J. Geophys. Res.*, 79(15), 2185–2197, https://doi.org/10.1029/JC079i015p02185

Luo, Z., G. Y. Liu, and G. L. Stephens, 2008: CloudSat adding new insight into tropical penetrating convection, *Geophys. Res. Lett.*, 35, L19819, https://doi.org/10.1029/2008GL035330

Mace, G., 2007: Level 2 GEOPROF product process description and interface control document algorithm version 5.3, *Colorado State University*, 44 pp.

Marchand, R., G. G. Mace, T. Ackerman, and G. Stephens, 2008: Hydrometeor detection using Cloudsat—An Earth‐orbiting 94‐GHz cloud radar, *J. Atmos. Oceanic Technol.*, 25, 519–533, https://doi.org/10.1175/2007JTECHA1006.1

Marti, J., and K. Mauersberger, 1993: A survey and new measurements of ice vapor pressure at temperatures between 170 and 250K, *Geophys. Res. Lett.*, 20(5), 363–366, https://doi.org/10.1029/93GL00105

Masunaga, H., T. Matsui, W. Tao, A.Y. Hou, C.D. Kummerow, T. Nakajima, P. Bauer, W.S. Olson, M. Sekiguchi, and T.Y. Nakajima, 2010: Satellite Data Simulator Unit, *Bull. Amer. Meteor. Soc*., 91, 1625–1632, https://doi.org/10.1175/2010BAMS2809.1

Matricardi, M., F. Chevallier, G. Kelly, and J. N. Thépaut, 2004: An improved general fast radiative transfer model for the assimilation of radiance observations, *Quart. J. Roy. Meteor. Soc*., 130, 153–173, https://doi.org/10.1256/qj.02.181

Matrosov, S. Y., T. Uttal, and D. A. Hazen, 2004: Evaluation of radar reflectivity based estimates of water content in stratiform marine clouds, *J. Appl. Meteorol.*, 43, 405–419, https://doi.org/10.1175/1520-0450(2004)043<0405:EORREO>2.0.CO;2

Matsui, T., J. Santanello, J. J. Shi, W. K. Tao, D. Wu, C. Peters-Lidard, E. Kemp, M. Chin, D. Starr, M. Sekiguchi, and F. Aires, 2014: Introducing multisensor satellite radiance‐based evaluation for regional Earth System modeling, *J. Geophys. Res.*, 119, 8450–8475, https://doi.org/10.1002/2013JD021424

McCoy, D. T., D. L. Hartmann, M. D. Zelinka, P. Ceppi, and D. P. Grosvenor, 2015: Mixed‐phase cloud physics and Southern Ocean cloud feedback in climate models, *J. Geophys. Res.*, 120, 9539–9554, https://doi.org/10.1002/2015JD023603

McGill, M. J., M. A. Vaughan, C. R. Trepte, W. D. Hart, D. L. Hlavka, D. M. Winker, and R. Kuehn, 2007: Airborne validation of spatial properties measured by the CALIPSO lidar, *J. Geophys. Res.*, 112, D20201, https://doi.org/10.1029/2007JD008768

Meneghini, R., T. Iguchi, T. Kozu, L. Liao, K. Okamoto, J. A. Jones, and J. Kwiatkowski, 2000: Use of the Surface Reference Technique for Path Attenuation Estimates from the TRMM Precipitation Radar, *J. Appl. Meteor.*, 39, 2053–2070, https://doi.org/10.1175/1520-0450(2001)040<2053:UOTSRT>2.0.CO;2

Meneghini, R., J. A. Jones, T. Iguchi, K. Okamoto, and J. Kwiatkowski, 2004: A Hybrid Surface Reference Technique and Its Application to the TRMM Precipitation Radar, *J. Atmos. Oceanic Technol.*, 21, 1645–1658, https://doi.org/10.1175/JTECH1664.1

Miller, S. D., and G. L. Stephens, 2001: CloudSat instrument requirements as determined from ECMWF forecasts of global cloudiness, *J. Geophys. Res.*, 106, 17,713-17,733, https://doi.org/10.1029/2000JD900645

Mitchell, D.L., 1996: Use of Mass- and Area-Dimensional Power Laws for Determining Precipitation Particle Terminal Velocities, *J. Atmos. Sci.*, 53, 1710–1723, https://doi.org/10.1175/1520-0469(1996)053<1710:UOMAAD>2.0.CO;2

Morrison, H., G. de Boer, G. Feingold, J. Harrington, M. D. Shupe, and K. Sulia, 2012: Resilience of persistent Arctic mixed-phase clouds, *Nature Geoscience*, v.5, p. 11, https://doi.org/10.1038/ngeo1332

Nakajima, T., and M. Tanaka, 1986: Matrix formulation for the transfer of solar radiation in a plane-parallel scattering atmosphere, *J. Quant. Spectrosc. Radiat. Transfer*, 35, 13-21, https://doi.org/10.1016/0022-4073(86)90088-9

Okamoto, H., T. Nishizawa, T. Takemura, H. Kumagai, H. Kuroiwa, N. Sugimoto, I. Matsui, A. Shimizu, S. Emori, A. Kamei, and T. Nakajima, 2007: Vertical cloud structure observed from shipborne radar and lidar: Midlatitude case study during the MR01/K02 cruise of the research vessel Mirai, *J. Geophys. Res.*, 112, D08216, https://doi.org/10.1029/2006JD007628

Okamoto, H., T. Nishizawa, T. Takemura, K. Sato, H. Kumagai, Y. Ohno, N. Sugimoto, A. Shimizu, I. Matsui, and T. Nakajima, 2008: Vertical cloud properties in the tropical western Pacific Ocean: Validation of the CCSR/NIES/FRCGC GCM by shipborne radar and lidar, *J. Geophys. Res.*, 113, D24213, https://doi.org/10.1029/2008JD009812

Okamoto, H., K. Sato, and Y. Hagihara, 2010: Global analysis of ice microphysics from CloudSat and CALIPSO: Incorporation of specular reflection in lidar signals, *J. Geophys. Res.*, 115, D22209, https://doi.org/10.1029/2009JD013383

Ota, Y., A. Higurashi, T. Nakajima, and T. Yokota, 2009: Matrix formulations of radiative transfer including the polarization effect in a coupled atmosphere-ocean system, *J. Quant. Spectrosc. Radiat. Transfer*, 111, 878-894, https://doi.org/10.1016/j.jqsrt.2009.11.021

Ovarlez, J., P. van Velthoven, G. Sachse, S. Vay, H. Schlager, and H. Ovarlez, 2000: Comparison of water vapor measurements from POLINAT 2 with ECMWF analyses in high-humidity conditions, *J. Geophys. Res.*, 105(D3), 3737–3744, https://doi.org/10.1029/1999JD900954

Platnick, S., M. D. King, S. A. Ackerman, W. P. Menzel, B. A. Baum, J. C. Riedi, and R. A. Frey, 2003: The MODIS cloud products: Algorithms and examples from Terra, *IEEE Trans. Geosci. Remote Sens.*, 41(2), 459–473, https://doi.org/10.1109/TGRS.2002.808301

Probst, P., R. Rizzi, E. Tosi, V. Lucarini, and T. Maestri, 2012: Total cloud cover from satellite observations and climate models, *Atmospheric Research*, 107, 161-170, https://doi.org/10.1016/j.atmosres.2012.01.005

Protat, A., D. Bouniol, E. J. O'Connor, H. K. Baltink, J. Verlinde, and K. Widener, 2011: CloudSat as a Global Radar Calibrator, *J. Atmos. Oceanic Technol.*, 28, 445–452, https://doi.org/10.1175/2010JTECHA1443.1

Pruppacher, H. R., and J. D. Klett, 1997: Microphysics of Clouds and Precipitation, *Oxford Univ. Press*, 914 pp.

Rädel, G., and K. P. Shine, 2010: Validating ECMWF forecasts for the occurrence of ice supersaturation using visual observations of persistent contrails and radiosonde measurements over England, *Quart. J. Roy. Meteor. Soc.*, 136, 1723-1732, https://doi.org/10.1002/qj.670

Rauber, R. M., and A. Tokay, 1991: An Explanation for the Existence of Supercooled Water at the Top of Cold Clouds, *J. Atmos. Sci.*, 48, 1005-1023, https://doi.org/10.1175/1520-0469(1991)048<1005:AEFTEO>2.0.CO;2

Riedi, J., B. Marchant, S. Platnick, B. A. Baum, F. Thieuleux, C. Oudard, F. Parol, J. M. Nicolas, and P. Dubuisson, 2010: Cloud thermodynamic phase inferred from merged POLDER and MODIS data, *Atmospheric Chemistry and Physics*, 10, 11,851–11,865. https://doi.org/10.5194/acp-10-11851-2010

Rodgers, C. D., 2000: Inverse methods for atmospheric sounding: theory and practice, vol. 2 of Atmospheric, Oceanic and Planetary Physics World Scientific, Singapore.

Rogers, R. R., and M. K. Yau, 1989: A Short Course in Cloud Physics, 3rd ed., 290 pp., *Elsevier*, New York.

Rossow, W. B., and Y. Zhang, 2010: Evaluation of a Statistical Model of Cloud Vertical Structure Using Combined CloudSat and CALIPSO Cloud Layer Profiles, *J. Climate*, 23, 6641–6653, https://doi.org/10.1175/2010JCLI3734.1

Sassen, K., and J. Zhu, 2009: A global survey of CALIPSO linear depolarization ratios in ice clouds: Initial findings, *J. Geophys. Res.*, 114, D00H07, https://doi.org/10.1029/2009JD012279

Sassen, K., V. K. Kayetha, and J. Zhu, 2012: Ice cloud depolarization for nadir and off-nadir CALIPSO measurements, *Geophys. Res. Lett.*, 39, L20805, https://doi.org/10.1029/2012GL053116

Shupe, M. D., S. Y. Matrosov, and T. Uttal, 2006: Arctic mixed-phase cloud properties derived from surface-based sensors at SHEBA, *J. Atmos. Sci.*, 63, 697-711, https://doi.org/10.1175/JAS3659.1

Shupe, M. D., 2007: A ground-based multisensor cloud phase classifier, *Geophys. Res. Lett.*, 34, L22809, doi:10.1029/2007GL031008, https://doi.org/10.1029/2007GL031008

Smirnov, A., B. N. Holben, T. F. Eck, O. Dubovik, and I. Slutsker, 2000: Cloud-screening and quality control algorithms for the AERONET database, *Remote Sens. Environ.*, 73(3), 337–349, https://doi.org/10.1016/S0034-4257(00)00109-7

Smirnov, A., B. N. Holben, O. Dubovik, R. Frouin, T. F. Eck, and I. Slutsker, 2003: Maritime component in aerosol optical model derived from Aerosol Robotic Network data, *J. Geophys. Res.*, 108(D1, 4033), https://doi.org/10.1029/2002JD002701

Stephens, G. L., and J. M. Haynes, 2007: Near global observations of the warm rain coalescence process, *Geophys. Res. Lett.*, 34, L20805, https://doi.org/10.1029/2007GL030259

Stephens, G. L., D. G. Vane, R. J. Boain, G. G. Mace, K. Sassen, Z. Wang, A. J. Illingworth, E. J. O'connor, W. B. Rossow, S. L. Durden, S. D. Miller, R. T. Austin, A. Benedetti, C. Mitrescu, and The CloudSat Science Team, 2002: THE CLOUDSAT MISSION AND THE A-TRAIN A New Dimension of Space-Based Observations of Clouds and Precipitation, *Bull. Amer. Meteor. Soc.*, 83, 1771-1790, https://doi.org/10.1175/BAMS-83-12-1771

Stephens, G. L., D. G. Vane, S. Tanelli, E. Im, S. Durden, M. Rokey, D. Reinke, P. Partain, G. G. Mace, R. Austin, T. L'Ecuyer, J. Haynes, M. Lebsock, K. Suzuki, D. Waliser, D. Wu, J. Kay, A. Gettelman, Z. Wang, and R. Marchand, 2008: CloudSat mission: Performance and early science after the first year of operation, *J. Geophys. Res.*., 113, D00A18, https://doi.org/10.1029/2008JD009982

Storelvmo, T., I. Tan, and A. V. Korolev, 2015: Cloud Phase Changes Induced by CO2 Warming—a Powerful yet Poorly Constrained Cloud-Climate Feedback, *Curr. Clim. Change Rep.*, 1:288–296, https://doi.org/10.1007/s40641-015-0026-2

Sun, W., N. G. Loeb, and P. Yang, 2006: On the retrieval of ice cloud particle shapes from POLDER measurements, *Quart. J. Roy. Meteor. Soc.*, 101, 435–447.

Tan, I., T. Storelvmo, M. D. Zelinka, 2016: Observational constraints on mixed-phase clouds imply higher climate sensitivity, *Science*, 352, 6282, 224-227, https://doi.org/10.1126/science.aad5300

Tanré, D., Y. J. Kaufman, M. Herman, and S. Mattoo, 1997: Remote sensing of aerosol properties over oceans using the MODIS/EOS spectral radiances, *J. Geophys. Res.*, 102, D14, 16971–16988, https://doi.org/10.1029/96JD03437

Tompkins, A. M., K. Gierens, and G. Radel, 2007: Ice supersaturation in the ECMWF integrated forecast system, *Quart. J. Roy. Meteor. Soc.*, 133, 53-63, https://doi.org/10.1002/qj.14

Trenberth, K.E., and J.T. Fasullo, 2010: Simulation of Present-Day and Twenty-First-Century Energy Budgets of the Southern Oceans, *J. Climate*, 23, 440–454, https://doi.org/10.1175/2009JCLI3152.1

Twomey, S., 1974: Pollution and the planetary albedo, *Atmos. Environ.*, 8, 1251–1256, https://doi.org/10.1016/0004-6981(74)90004-3

Wang, Z., D. Vane, G. Stephens, and D. Reinke, 2013: Level 2 combined radar and lidar cloud scenario classification product process description and interface control document, version 1.0, 22 pp.

Wang, X., W. Li, Y. Zhu, and B. Zhao, 2013: Improved cloud mask algorithm for FY-3A/VIRR data over the northwest region of China, *Atmos. Meas. Tech.*, 6, 549-563, https://doi.org/10.5194/amt-6-549-2013

WCP-55, 1983: Report of the experts meeting on aerosols and their climate effects, 107 pp., *World Meteorological Organization*.

Vaughan, M. A., D. M. Winker, and K. A. Powell, 2005: CALIOP algorithm theoretical basis document, part 2, feature detection and layer properties algorithms, PC‐SCI‐202.02, *NASA Langley Res. Cent.*, Hampton, Va.

Voors, R., D. Donovan, J. Acarreta, M. Eisinger, R. Franco, D. Lajas, R. Moyano, F. Pirondini, J. Ramos, and T. Wehr, 2007: ECSIM: the simulator framework for EarthCARE, *Proc. SPIE*, 6744, 67441Y, https://doi.org/10.1117/12.737738

Yang, J., Wang, Z., Heymsfield, A. J., and Luo, T. 2016: Liquid/Ice Mass Partition in Tropical Maritime Convective Clouds, *J. Atmos. Sci.*, https://doi.org/10.1175/JAS-D-15-0145.1

Yoshida, Y., H. Okamoto, and Y. Hagihara, 2010: Global analysis of cloud phase and ice crystal orientation from Cloud‐Aerosol Lidar and Infrared Pathfinder Satellite Observation (CALIPSO) data using attenuated backscattering and depolarization, *J. Geophys. Res.*, 115, D00h32, https://doi.org/10.1029/2009JD012334

Zhang, J., and J. S. Reid, 2006: MODIS aerosol product analysis for data assimilation: Assessment of over-ocean level 2 aerosol optical thickness retrievals, *J. Geophys. Res.*, 111, D22207, https://doi.org/10.1029/2005JD006898

Zhou, C., P. Yang, A. E. Dessler, Y. Hu, and B. A. Baum, 2012: Study of Horizontally Oriented Ice Crystals with CALIPSO Observations and Comparison with Monte Carlo Radiative Transfer Simulations, *J. Appl. Meteor. Clim.*, 51, 1426-1439, https://doi.org/10.1175/JAMC-D-11-0265.1

Zhou, C., P. Yang, A. E. Dessler, and F. Liang, 2013: Statistical Properties of Horizontally Oriented Plates in Optically Thick Clouds From Satellite Observations, *IEEE Trans. Geosci. Remote Sens. Lett.*,10, https://doi.org/10.1109/LGRS.2012.2227451